Title

Method Development for Polymer Thin Film Characterization with Applications in Perfluorinated Sulfonic Acid Polymers

Permalink

https://escholarship.org/uc/item/1xm2w470

Author

Dudenas, Peter J

Publication Date

2020

Peer reviewed|Thesis/dissertation

Method Development for Polymer Thin Film Characterization
with Applications in Perfluorinated Sulfonic Acid Polymers

By

Peter J. Dudenas

A dissertation submitted in partial satisfaction of the

requirements for the degree of

Doctor of Philosophy

in

Chemical Engineering

in the

Graduate Division

of the

University of California, Berkeley

Committee in charge:

Dr. Adam Z. Weber, Co-Chair
Professor Bryan D. McCloskey, Co-Chair
Professor Nitash P. Balsara
Professor Andrew Minor

Spring 2020

Method Development for Polymer Thin Film Characterization
with Applications in Perfluorinated Sulfonic Acid Polymers
© Copyright 2020
Peter J. Dudenas

Abstract

Method Development for Polymer Thin Film Characterization
with Applications in Perfluorinated Sulfonic Acid Polymers

by

Peter J. Dudenas

Doctor of Philosophy in Chemical Engineering

University of California, Berkeley

Dr. Adam Z. Weber, Co-Chair
Professor Bryan D. McCloskey, Co-Chair

Electrochemical energy-conversion devices represent a potentially significant contribution to the renewable-energy paradigm. A subclass of these devices (fuel cells, electrolyzers, flow batteries, CO_2 reduction devices, *etc.*) rely on ion-conducting polymers (ionomers) as a critical component to transport reactants and products between and within the device's electrodes. A major impediment towards widespread implementation of these devices is high transport resistance within the electrode. Previous research has correlated the resistance to the ionomer that exists as thin films in the electrodes, but the origin of the resistance remains unknown. To enable next-generation electrochemical energy-conversion devices, it is crucial to understand better the structure-property relationships of these ionomer thin films.

Perfluorosulfonic acid (PFSA) ionomers are heavily utilized for these technologies due to their excellent mechanical and electrochemical stability and superior ion transport. They are random copolymers with a hydrophobic PTFE backbone and pendant side-chains that are terminated with a sulfonic-acid group. Upon hydration, the acid-group proton dissociates and enables high ionic conductivity. While this class of materials has been heavily studied in bulk membrane form, the behavior of PFSAs as thin films in catalyst layers is poorly understood. Part of the reason for this are the difficulties in ionomer thin-film characterization.

Because of these challenges, the first half of this dissertation focuses on method development for thin-film characterization. The first and foremost characterization method covered is grazing-incidence x-ray scattering (GIXS). A general introduction is given and the differences between transmission and GIXS are highlighted. These concepts are built upon to construct a new method of data collection and analysis, termed electric field intensity (EFI)-modulated scattering. This technique allows high-resolution depth-profiling of thin film samples, which is not achievable with standard GIXS experiments.

A cantilever bending method for the mechanical characterization of thin films is described within polymer network theory and solid mechanics analysis, and validated with a model hydrogel system. It is shown that the osmotic pressure and equilibrium shear modulus can be measured in non-glassy materials. Characterizing PFSA thin-film

mechanical properties is discussed in the context of these results, and the chapter concludes with a discussion on extending the technique to study thin films under different thermal conditions.

As PFSAs exist in catalyst layers, there is a need to study and understand their behavior under working conditions such as applied potentials. The fabrication of heterogeneous, planar electrode devices for *operando* characterization is discussed, and two different ionomer chemistries are used as case studies for the device. In the first case study, Nafion thin films show a change in through-plane density with applied potential. The second case study uses a perfluorinated anion exchange membrane, which shows a change in morphology from lamellae to a bicontinuous structure as the anionic form is reacted from carbonated species to hydroxide. Based on these findings, we discuss improvements to the cell design, as well as fabrication of interdigitated electrodes for detailed impedance measurements.

The second half of the dissertation focuses on studying the structure and physical properties of PFSA thin films. This starts with a study on the morphological evolution of PFSA thin-film formation. An *in-situ* slot die coater is used to cast ionomer dispersions and GIXS is used to investigate the dynamic behavior of ionomer morphology as it dries into thin films. Aggregate interactions in dispersion directly impact the hydrophilic-domain network of the cast film and the onset of crystallization occurs simultaneously with the solution-to-film transition but each length scale evolves on different time scales. In addition, confinement is shown to induce anisotropic morphology at multiple length scales. These results demonstrate promising avenues for tuning ionomer morphology during film formation and end-film functionality.

The inverse relationship between mechanical properties and water uptake is well established in PFSA membranes, but less so in thin films. This relationship is investigated in PFSA thin films and connected to the nanostructural morphology using GIXS and the cantilever bending method. GIXS was used to determine the relative degree of crystallinity for Nafion thin films at three different annealing temperatures and across a range of thicknesses. From these measurements, transitional points in confinement effects are identified and reveal a counterintuitive decrease in crystallinity with increasing annealing temperature. Films prepared under the same conditions were measured with the cantilever bending method. The same universal inverse relationship between mechanical properties and water uptake is observed in thin films prepared under these conditions. The connection between the crystallinity and macroscopic mechanical properties is less strong, which highlights network effects and the complex structure of PFSAs.

The final study looks at the structure and swelling behavior of Nafion and 3M PFSA ionomer thin films. Each of these chemistries were annealed across a range of temperatures and their structure was characterized using GISAXS and correlated to water uptake measurements. Domain correlations are oriented through-plane in films annealed below their thermal transition. Above this transition, the domain orientation becomes isotropic and there is a corresponding decrease in water uptake, which demonstrates the connection between the nanostructural morphology and resulting physical properties. This chapter ends with a discussion on investigating domain connectivity and tortuosity using the interdigitated electrodes developed in Chapter 4.

Table of Contents

List of Figures

List of Tables

Acknowledgments

I have been incredibly fortunate to be surrounded by a wonderful family. Without the support and encouragement from my family: Mum, Dad, and Nick, I most likely would not have come to grad school. Thank you for always being there for me. Once I did make that decision to move across the country, my cousins, the Cesniks, immediately made the Bay Area feel like home. Thank you for giving me a home away from home.

To my advisors, Adam, Bryan, and Ahmet, thank you for providing me every opportunity to learn and develop into the researcher I am today. Notable examples include teaching me electrochemistry, correcting my liberal use of split infinitives, and showing me what a publication-quality figure should look like. I also appreciate the freedom to explore topics that at first glance seem unrelated to fuel-cell research.

Getting started on PFSA research was much easier with Meron's help. Thank you for being a mentor in the lab and teaching me to always be skeptical of Nafion. Andrew was also an integral part of my research experience. You are an academic in every sense of the word and our conversations over the past five and a half years have been invaluable.

I also have many friends to thank outside of the lab for making Berkeley a great place to spend my Ph.D.: my roommates of the Alligator house, my classmates and the greater CBE department, and my teammates on the East Bay Athletic Club. Similarly, thanks to my high school friends who succeed in making me laugh harder than anyone else.

Last, but not least, thank you Sarah. Your persistent reminders to help me finish this dissertation on time is but one small of example of how you make me better in every way.

1   Introduction

1.1   Background

Solid-state energy technologies including polymer-electrolyte fuel cells (PEFCs), electrolyzers, and vapor-fed solar-fuel generators have garnered significant attention in recent years driven by the need for clean and sustainable energy solutions. These electrochemical energy devices involve multiple functional layers with active interfaces and combinations of materials with varying physical processes and chemical reactions. Figure 1.1 shows a schematic of a PEFC.
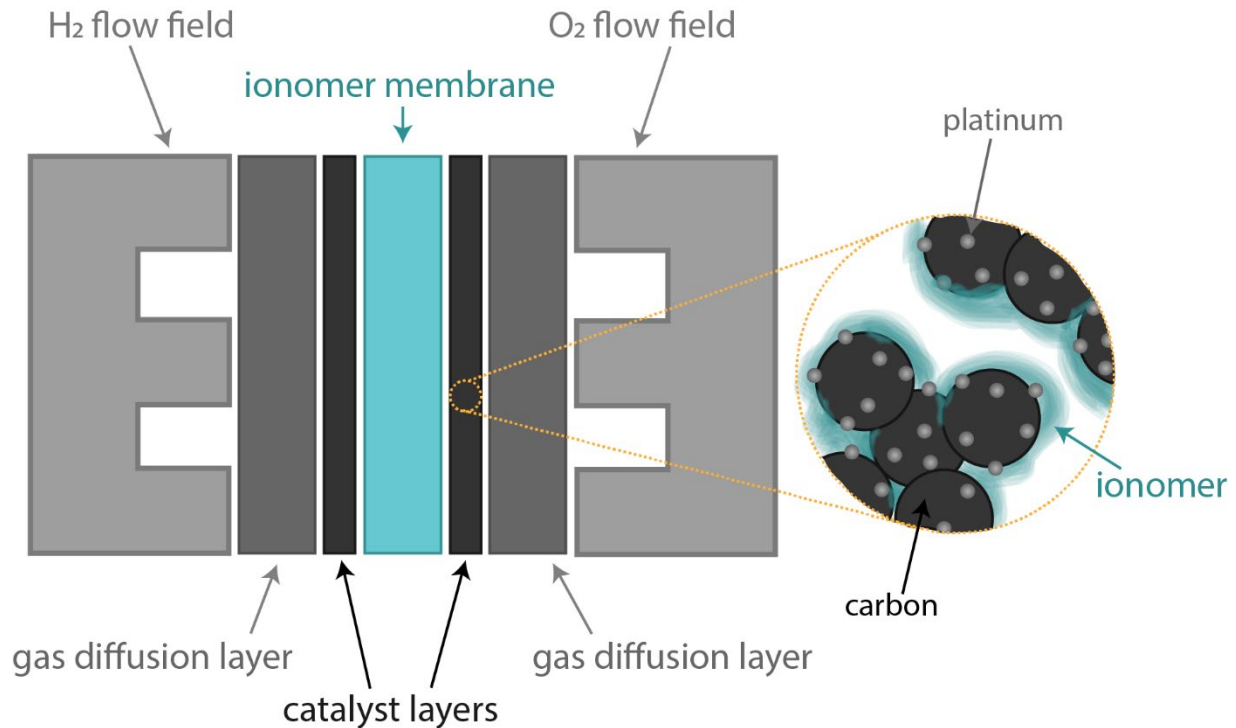
Figure 1.1. PEFC schematic showing individual components. Close up of catalyst layer depicts the heterogeneous environment the perfluorinated sulfonic acid ionomer thin films exist in. Figure credited to Sarah Berlinger.

Chief among the physical processes is the transport of charged intermediates (e.g, protons, redox cations) through solid-state ion-conducting polymer (ionomer) pathways.[1] This ionomer exists both as a membrane (micrometers thick), and in the catalyst layers as thin films (nanometers thick). The catalyst layer is a porous electrode composed of pores, ionomer, and platinum supported on carbon nanoparticles; it is formed by spraying or casting inks of the constituent species. Ionomer present as thin films in catalyst layers helps bind the catalyst particles while facilitating ionic-species conduction for electrochemical redox reactions; but the general understanding of how the ionomer behaves in the catalyst layer is not well known.[2-3] While this class of materials has been extensively characterized in bulk form, their properties (mechanical, structural, electrochemical, *etc*.) when confined to smaller length scales are not well understood. Some work in the literature shows the properties are very different,[4-6] but the origin for this difference has not been rationalized. As a result of this confinement, high transport resistances for

gaseous reactants through ionomer thin films have been observed,[7] but the origin of this resistance remains unknown. Multiple open hypotheses have been put for including sulfonic-acid-group-platinum poisoning (from interactions with the ionomer side chains, discussed below), and high interfacial and internal resistances, but no conclusive mechanisms have been elucidated. To summarize, the interaction of the ionomer thin film with these catalyst particles, and how that interaction affects structural and relevant properties is not well understood. A fundamental understanding of their structure and physical properties as thin films in catalyst layers must be established to optimize electrochemical technologies in the desired new clean-energy paradigm.

Nafion, a perfluorinated sulfonic-acid (PFSA) ionomer, is the most heavily studied and utilized ionomer since it was first synthesized by Walther Grot at DuPont in the late 1960's.[8] All PFSAs are comprised of a polytetrafluoroethylene backbone that imparts excellent mechanical stability, and pendant side chains terminated with sulfonic-acid groups enabling high proton conductivity, although the exact side-chain chemistry may vary.[2] The hydrophobic backbone and hydrophilic functional group weakly phase separate during hydration, leading to a poorly ordered bi-continuous matrix.[9] Upon hydration, the hydrophilic regions swell with water, and create ion-conduction pathways through the ionomer. Even after extensive research into alternative chemistries, Nafion and other PFSAs remain the preferred material for these devices. Figure 1.2 shows the chemistries for some commonly used PFSAs.
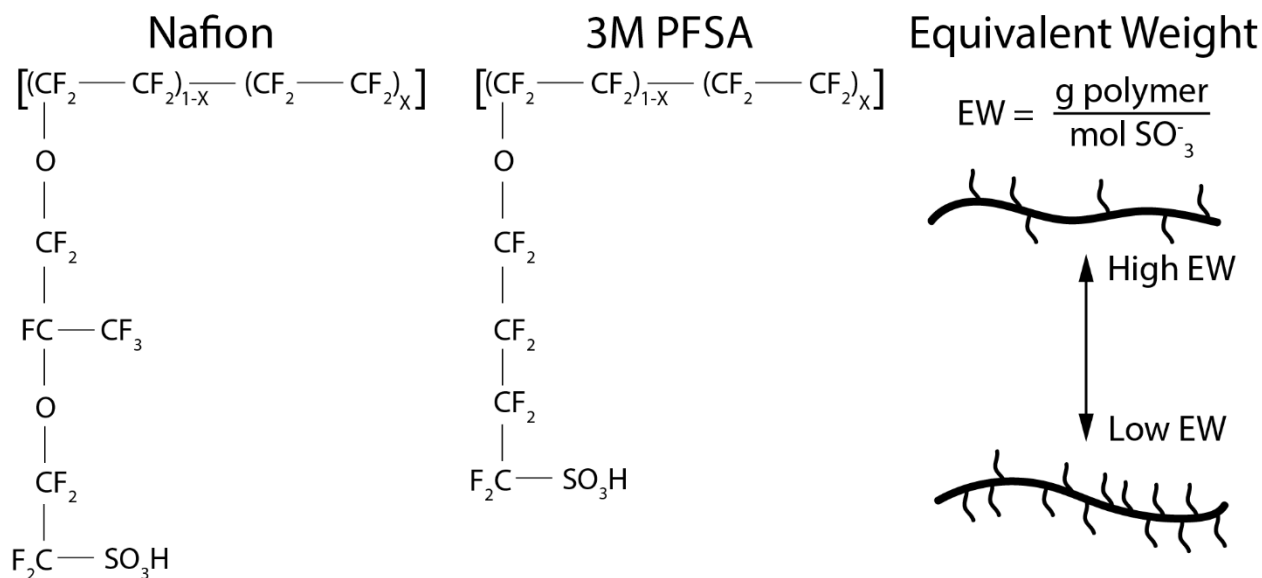
Figure 1.2. Chemical structure of Nafion and 3M PFSA and a diagram illustrating equivalent weight. The fraction X will change depending on equivalent weight.

In addition to Nafion, now manufactured by Chemours, the 3M Company synthesizes several PFSAs for academic and commercial use. The 3M PFSA sidechain is slightly shorter than that of Nafion. All of the 3M PFSAs have this same shorter side-chain chemistry, but the density of side-chains on the backbone may vary. Within the PFSA ionomer community, this differing side-chain density (and therefore ionic-group density) is referred to as the equivalent weight (EW), which is defined as the grams of polymer per sulfonic-acid group. Higher EWs indicate relatively fewer ionic groups per PTFE backbone units, while lower EWs have relatively greater sidechain density (Figure 1.2). Crystallinity is a function of EW; a higher density of side chains interrupts

chain packing and prevents crystallization of the backbone. Additionally, the EW dictates the driving force for water sorption into these materials. More sulfonic-acid groups lead to higher water contents and higher conductivity, at the cost of lower mechanical stability due to lower crystallinity. Together, Nafion and the library of 3M PFSAs are the materials of study within this dissertation and have helped elucidate the effect of EW on morphology and physical properties in PFSA thin films.
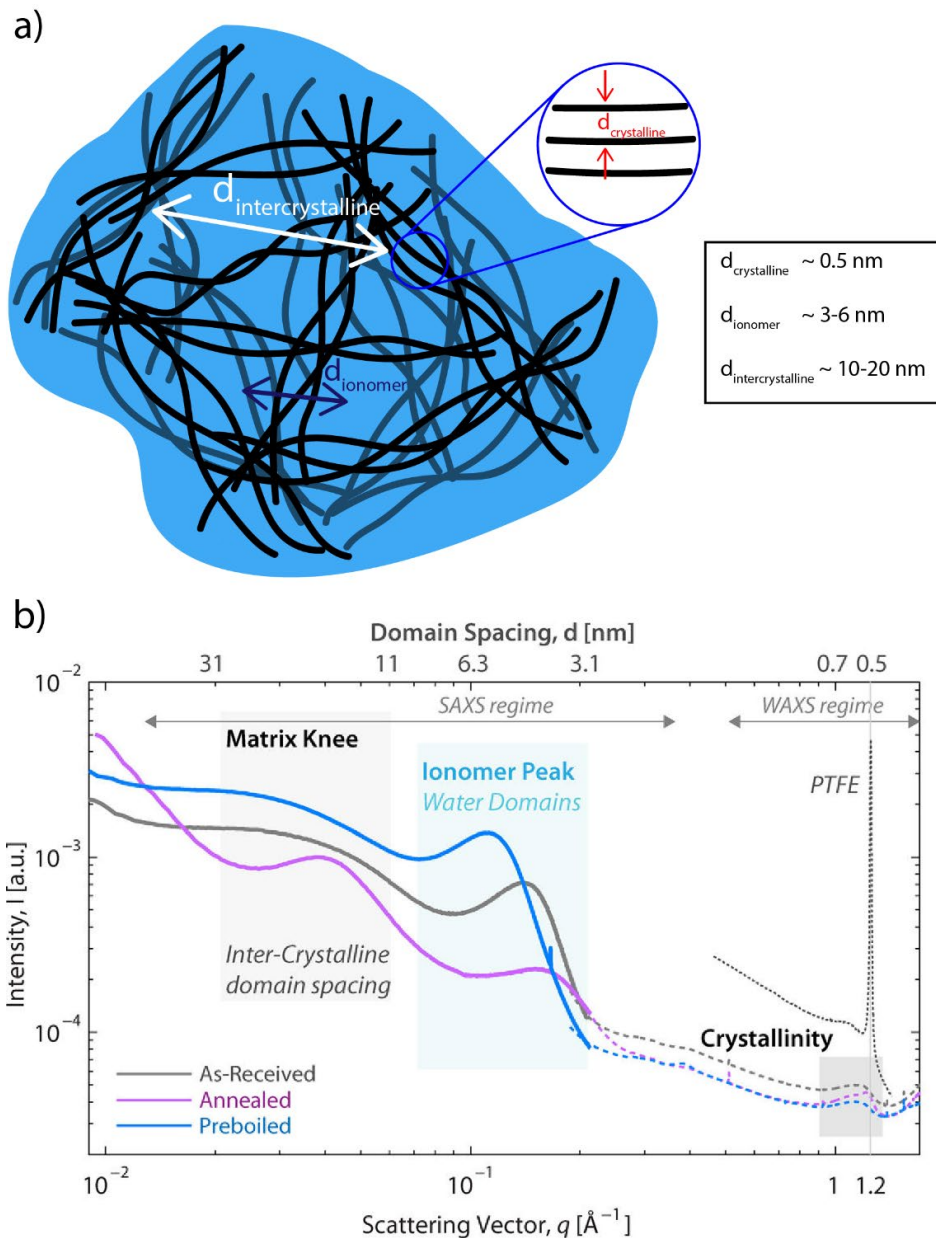
Figure 1.3. a) Schematic of PFSA phase-separated structure b) X-ray scattering line cuts for PFSA membranes with the individual features marked, as adapted from Ref. 3.

1.1.1 Morphology

Across different EWs and side-chain chemistry, PFSAs display similar phase-separated morphology (Figure 1.3). Hydrophobic regions of semi-crystalline backbone are interspersed with

the hydrophilic regions that consist of the side chain and terminal-acid group. At very small length scales (~0.5 nm), the semi-crystalline phase appears as a convoluted peak in wide-angle x-ray scattering (WAXS).[10] The crystallinity of these ionomers is both a function of EW and processing conditions. At longer length scales (3-6 nm), the phase-separated morphology has a characteristic distance that manifests as a broad peak in small-angle x-ray scattering (SAXS). Known as the "ionomer peak", its position is dependent on the hydration of the material (water volume fraction) and the side-chain length; the intensity of the peak is shown to be a function of EW, hydration, and cation identity. The largest feature generally probed is known as the intercrystalline peak or "matrix knee", which appears at 10-20 nm. This peak has been attributed to the distance between crystallites in PFSAs and has been shown to grow with increasing EW.[3, 11]

Upon confinement to thin films, the phase-separated structure is similar, but can be significantly altered. Grazing incidence small-angle x-ray scattering (GISAXS) has shown alignment of the phase-separated structure with the underlying substrate,[6, 12] and neutron reflectivity (NR) has revealed strong multi-lamellar ordering close to the substrate-film interface.[13-15] This strong ordering has implications for reactant transport to catalytic sites, and the connection between morphology, water uptake, and transport is critical to understand. At the start of my PhD, much of the thin-film work had been done on Nafion; part of my efforts has been directed towards studying additional PFSA chemistries to understand the universality of confinement effects as well as extend the knowledge and development for different property interrogations.

1.1.2 Physical Properties

The behavior of PFSAs is not well understood once they are confined within a catalyst layer. The heterogeneous nature of catalyst layers, composed of ionomer, inorganic catalyst, and carbon support, make it difficult to probe behavior and define structure-property relationships. Past research has employed model systems, looking at the effect of varying ionomer thin-film thickness and support material on planar architectures, to elucidate the nature of interactions present in catalyst layers. Upon confinement, reduced water uptake and conductivity, and increased mechanical properties, have been observed for Nafion thin films.[4-5] The magnitude of deviations in behavior due to confinement is a function of the wetting interactions between the thin film and substrate to which it is confined.[6]

Drawing from the larger polymer-physics community, confinement effects appear when the film thickness approaches the characteristic length scales of the polymer domains (which is usually on the order of nanometers), resulting in deviations in the glass-transition, melting, and crystallization temperatures, among others.[16-19] The glass-transition temperature, Tg, in glassy and semi-crystalline polymer is a particularly well-studied property. Depending on the nature of the polymer's interaction with a substrate, positive and negative deviations from the bulk Tg have been observed.[20] Such interactions are expected to become even more critical in ionomers. As a charged polymer however, PFSAs are not classical glassy materials and exhibit multiple thermal transitions. At room temperature, PFSAs are below their α-transition, which is the temperature at which the electrostatic network between sulfonic-acid group becomes weak enough that the polymer can attain long-range mobility.[21] While not a traditional glassy state, the material is not at a thermodynamic equilibrium and exhibits hysteresis in swelling-deswelling measurements. This has implications for mechanical properties, and how annealing and processing affects the α-transition remain unknown.

Because PFSA thin films exist in the heterogeneous environment of a catalyst layer, there is also a need to understand their behavior under the same conditions as a working PEFC. Very little work has been done to characterize the structure or physical properties of PFSA thin films under applied potentials. PFSA membranes have been incorporated into soft actuating devices driven by electric fields.[22-23] These devices have a strong actuation in response to applied electric fields, which is attributed to electroosmotic flux of water in the PFSA. Spectroscopic[24] and electrochemical[25] studies show strong local adsorption of the sulfonic-acid groups that is potential-dependent. How this adsorption and electroosmotic-driven water flux effects the larger length scale structure and macroscopic physical properties is an open question and the next step in understanding structure-property relationship in PFSA ionomer thin films.

1.2   Challenges and Open Questions

While differences between bulk membranes and thin films have been observed, many questions were unanswered during the start of my PhD and a number of them remain open. Are these differences rooted in film formation and can we control casting conditions such that we can tune the end functionality/behavior of these materials? Once cast, how is the nanostructural morphology related to the observed physical properties? Literature in the fuel-cell community for bulk membranes has demonstrated the genesis of transport properties lies with the molecular balance of water sorption/solvation and mechanical resistance to swelling. The resulting transport properties are governed by water content and the water content for a given humidity is governed by the backbone and crystallinity. For PFSA thin films, how are these relationships perturbed and are they universal across different PFSA chemistries?

Many of these questions were unanswered because of the difficulty in characterizing PFSA thin films. Structural characterization of the nanostructure is done with GIXS. The small amount of material (nanometer thicknesses) and the weak phase-separation leads to low scattering signal intensity. For the mechanical characterization, traditional stress-strain experiments used for bulk membranes are not applicable because the thin films are supported on a rigid substrate. To answer open questions regarding PFSA behavior in thin films, the techniques used to characterize their behavior also needed to be developed further, which is a major theme of this dissertation.

1.3   Dissertation Outline

This dissertation is organized into two themes. Chapters 2-4 discuss technique development for thin-film characterization, while Chapters 5-7 apply these techniques to characterize PFSA ionomer materials. Chapter 2 covers GIXS in detail. Basic concepts in x-ray scattering are introduced and the differences between transmission and grazing geometries are discussed. Development of electric field intensity (EFI)-modulated scattering is then detailed. In Chapter 3, a cantilever bending method for thin-film mechanical characterization is reviewed. The underlying polymer network theory is outlined and applied to model hydrogel thin films. Chapter 3 concludes with a discussion on extending the cantilever bending method beyond water sorption-driven experiments. Chapter 4 describes nanofabrication techniques for manufacturing heterogeneous substrates and devices for *operando* characterization. Devices made using these nanofabrication techniques are used in two case studies to characterize the structure of ionomer thin films under working potentials using GIXS. Chapter 5 discusses an *in-situ* GIXS study where Nafion ionomer dispersion was cast *in situ* at the beamline using a slot die coater. The morphological evolution is monitored using GIXS as the material goes from a dispersion to dried film. Chapter 6 examines the role of crystallinity on observed mechanical properties in Nafion thin

films using GIXS and the cantilever bending method. In Chapter 7, the relationship between annealing temperature, morphology, and water uptake is determined for a family of ionomer EWs. Together, this dissertation provides a methodology for elucidating structure-property relationships in ionomer thin films, and by applying this methodology, advances the understanding of PFSA ionomer morphology and its relationship to observed physical properties.

2 Concepts and Methods in Grazing Incidence X-Ray Scattering

2.1 Introduction

X-ray scattering is a non-destructive and extremely powerful method of characterizing the nanostructure of materials. First pioneered in the early 1900's, it has become a ubiquitous technique used in every discipline of the physical sciences from physics to biology. A considerably newer subset of x-ray scattering is performed in a grazing-incidence geometry. When the thickness of a material becomes less than a few micrometers, not enough material is present in the path of the beam to generate a strong scattering signal (at hard x-ray energies). By placing this material at a grazing angle to the x-ray beam, the path length through the material can be increased back towards millimeters to centimeters, which greatly increases the scattering signal. Grazing incidence x-ray scattering (GIXS) shares many of the same concepts as transmission scattering but is more complicated due to beam reflection and multiple scattering phenomena. This chapter covers many of the basic concepts in x-ray scattering and highlights the differences between transmission and grazing-incidence geometries. These concepts are then built upon to understand in more detail how to approach and analyze GIXS experiments and data. This culminates with electric field intensity (EFI)-modulated scattering, which is a novel way of collecting and analyzing GIXS data to determine the depth profile of thin film materials in greater detail than normal GIXS experiments. In total, this chapter serves as a general introduction to x-ray scattering and a reference for more advanced grazing-incidence data interpretation.

2.2 Concepts in X-Ray Scattering

X-ray scattering refers to the process of an incident x-ray interacting with electrons in a material. The interaction of this incident x-ray with the electron (details can be found elsewhere[26]) causes the electron to emit a spherical wave of radiation at the same energy as the incident x-ray. Because the incident and emitted x-rays are at the same wavelength, there is no change in energy and the scattering is elastic (Inelastic scattering is a separate domain of x-ray physics with its own applications). For a material with many electrons, spherical waves of radiation are emitted from each unique x-ray-electron interaction. This collective of spherically emitted x-rays sums constructively and destructively to form a scattering pattern that is indicative of how the electrons are arranged in the material. When two x-rays arrive in-phase with each other their amplitudes add up, and when they arrive out of phase, they cancel each other out. The phase between two waves depends on the distance between the points at which the x-rays were emitted, which can be described generally using Bragg's Law,

$$2d \sin \theta = n\lambda. \tag{2.1}$$

Bragg's law relates the angle, θ, at which two x-rays constructively interfere based on the distance, d, and the wavelength, λ. Because there are multiple distances that can satisfy this relation, n is the order or multiple at which this can occur. We can also define the scattering vector,

$$q = \frac{4\pi}{\lambda} \sin \theta, \tag{2.2}$$

and from Equations 2.1 and 2.2, we can relate the scattering vector to the real space distance,

$$q = \frac{2\pi}{d}.$$

(2.3)

Based on the angle at which a peak in the scattering pattern appears, we can calculate the distance between two electrons, atoms, or domains within a material. The scattering vector q is reciprocal to the distance: small distances lead to a large scattering angle and vector, and large distances have a small angle and vector. X-ray scattering is often divided in small- and wide-angle scattering (SAXS & WAXS), though there is no clear distinction between the two. WAXS generally looks at the crystalline structure of materials, while SAXS probes longer length scales that may occur in phase separated materials.

SAXS in particular is heavily utilized in the soft matter research community to understand how materials are arranged and distributed on length scales ranging from nanometers to microns. These length scales often dictate the performance or functionality of a material and by understanding how structure affects performance, materials can be better designed. The observed scattering intensity for SAXS can be defined generally as

$$I(q) \propto I_0 \, |\Delta\rho \, F(q) \, S(q)|^2,$$

(2.4)

where I_0 is the incident beam intensity, $\Delta\rho$ is the electron density contrast between two phases, $F(q)$ is the form factor, and $S(q)$ is the structure factor. The form factor describes the shape of a particle or domain in a material, and the structure factor describes how each of these discrete particles or domains are arranged with respect to one another. For materials with multiple phases or particles, the observed scattering intensity can have multiple contributions.
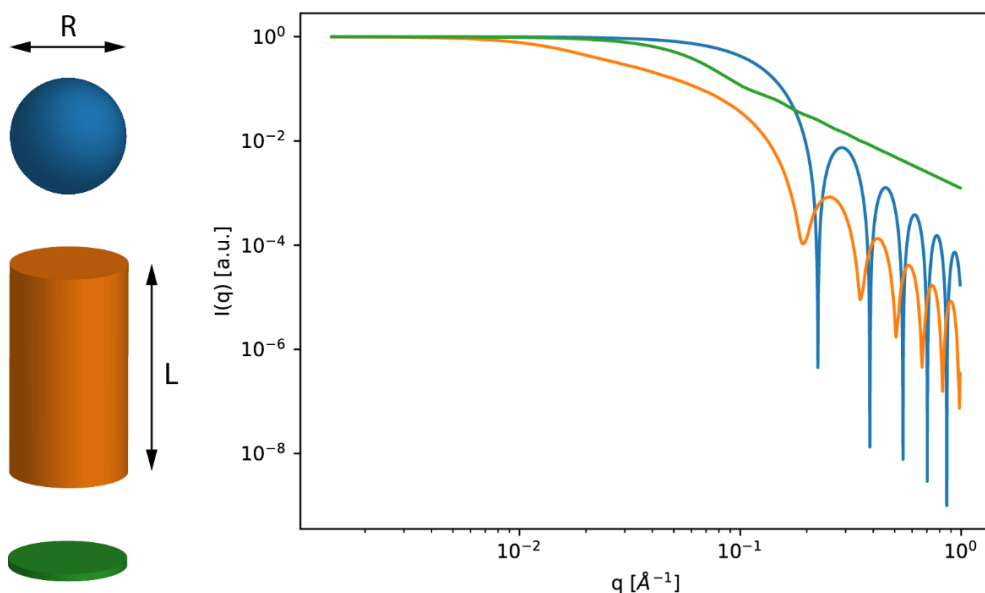
Figure 2.1. Form factors for a sphere, cylinder, and disk, all of radius R.

8

When a particle or domain is dilute enough such that there is no regular ordering on the same length scale, the structure factor goes to 1 and only the form factor and contrast contribute to the scattering pattern. Figure plots the form factor for a sphere, cylinder, and disk which all have the same radius, R. Each particle has a unique shape, and that shape is encoded in the observed scattering pattern. Because of this, x-ray scattering can determine the shape of domains and particles in addition to their size and how they are distributed.
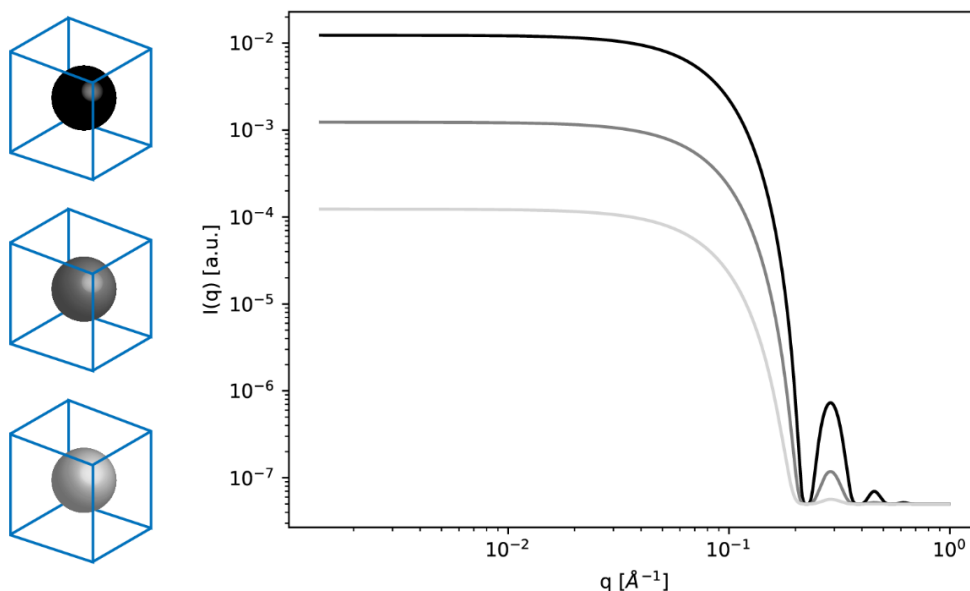
Figure 2.2. Effect of electron density contrast on the observed scattering for isolated spheres with a baseline noise background.

The effect of contrast between a particle and its surroundings is illustrated in Figure 2.2. For a sphere of three different electron densities in the same surrounding electron density material, there will be no change in the form factor; only the scattering intensity will change. For low contrast systems, signal-to-noise can become an issue. There are always background contributions to scattering patterns that come from a variety of sources including air scattering, surface scattering, and detector sensitivity. The peaks in the sphere's form factor in Figure 1.2 become less pronounced as the scattering intensity is reduced below the noise baseline, which would make it more difficult to fit and extract the sphere's radius.

These concepts are all valid whether performing x-ray scattering in a transmission or grazing-incidence geometry, but interpreting the scattering pattern in a grazing-incidence geometry becomes more complicated. This is because the GIXS pattern becomes 'distorted' relative to the transmission scattering pattern. Placing a material on a substrate breaks certain symmetries present in transmission geometry and necessarily makes the observed scattering pattern asymmetric. Additionally, the presence of the substrate reflects x-rays which changes the local electric field and adds contributions to the observed scattering. Section 1.3 describes these changes.

2.2.1 Additional Considerations in the Grazing-incidence Geometry

Figure 2.3 schematically shows a typical grazing incidence x-ray scattering experiment. A thin film sample is placed in the path of an incident x-ray beam at some incidence angle, α_i. X-rays scattered from the thin film sample are collected on a 2D area detector some distance from the sample. If the detector is close to the sample, it resolves wide-angle scattering and probes small length scales. When moved back to larger distances, the detector captures small-angle x-ray scattering and probes larger distances. Because the sample's substrate breaks symmetry relative to transmission scattering, the scattering vector q is now defined to have in-plane and out-of-plane components, which are q_p and q_z, respectively. The scattering vector components can be calculated from the in-plane and through-plane scattering angles, θ and α_f, respectively.
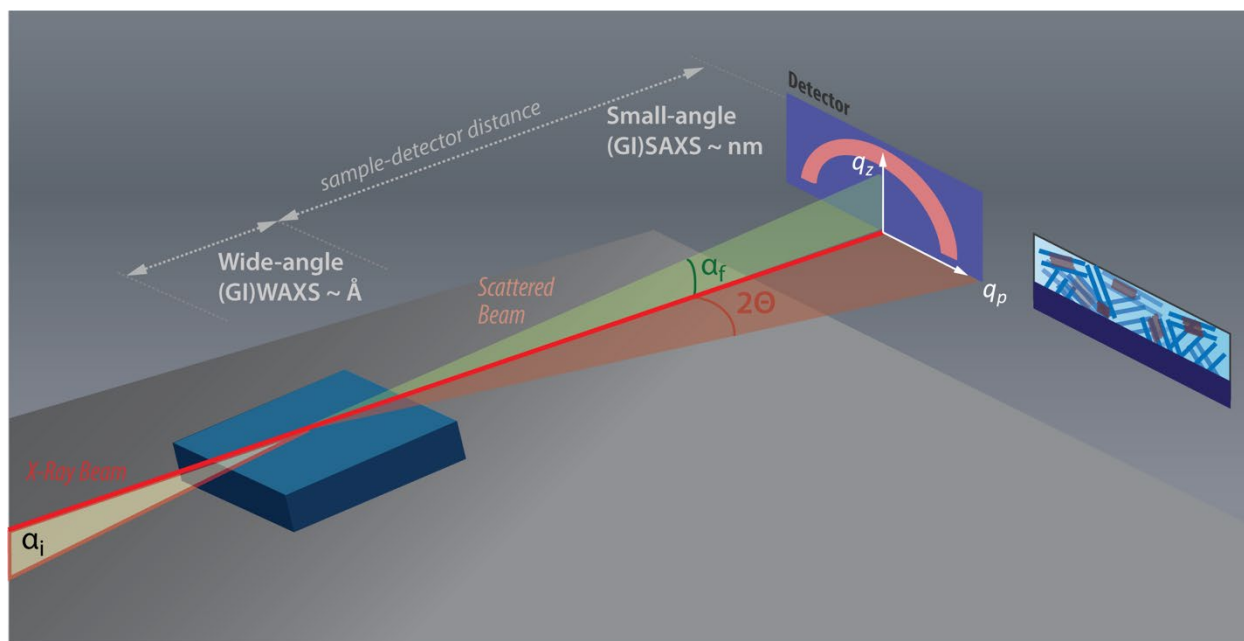
Figure 2.3. Schematic of a typical grazing incidence x-ray experiment.

2.2.2 Incidence Angle

The incidence angle at which an incident x-ray beam meets the thin film sample will dictate how much of the film is probed. Below the critical angle (α_c) of a material the x-rays will undergo total external reflection and not penetrate the material (except for an exponentially decaying evanescent wave). Above the critical angle, the penetration depth rapidly increases to the order of microns, and the entire thin film can be probed. The critical angle is directly proportional to the real part of the index of refraction, δ, and is calculated via

$$\alpha_c \approx \sqrt{2\delta}. \tag{2.5}$$

To enhance signal, the incidence angle is often chosen such that it is above the critical angle of a thin film, but below the critical angle of the underlying substrate. This causes the incident beam to reflect off the substrate and interfere with itself and induces strongly varying EFI within the film. This will be detailed further in Section 2.3.

2.2.3   Sample Orientation

For GIXS, it is useful to define the azimuthal angle, χ, which is the degrees from sample normal. Figure 2.4 diagrams this angle. χ ranges from 0 degrees, which is pointing normal to the substrate, to 90 degrees, which is parallel to the substrate. This quantity provides a reference frame for which to discuss how certain scattering peaks or correlations are oriented within the sample.
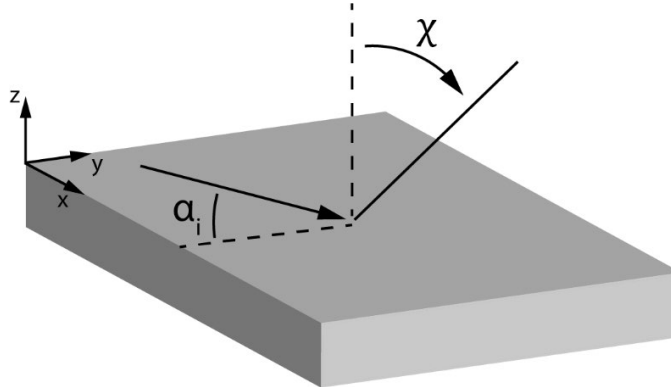
Figure 2.4. Diagram of a thin film sample, with the incidence angle and azimuthal angle marked.

Confinement to a substrate will often induce morphological orientation in thin film samples that is not present in bulk samples. This orientation can be a function of material-substrate interactions as well as the thin-film thickness. Figure 2.5 shows three different orientations that may occur in a thin film sample. The first scenario shows crystallites with their crystalline planes oriented through-plane which manifests in a scattering peak centered at some q_z with a small distribution in χ. There is also the correlation between crystallites, which is occurring in-plane at a longer length scale. This results in a scattering peak in-plane at a smaller q-value. The next scenario has the crystalline planes oriented in-plane. Now the scattering peak from the lattice planes is oriented in-plane, again with some small distribution in χ. The ordering between crystallites is unchanged, and the corresponding scattering peak at smaller q is also unchanged. The last scenario is a sample with crystallites that have a uniform distribution in χ. Now the scattering peak from the lattice planes appears as an isotropic ring, with the inter-crystallite peak still centered in-plane.
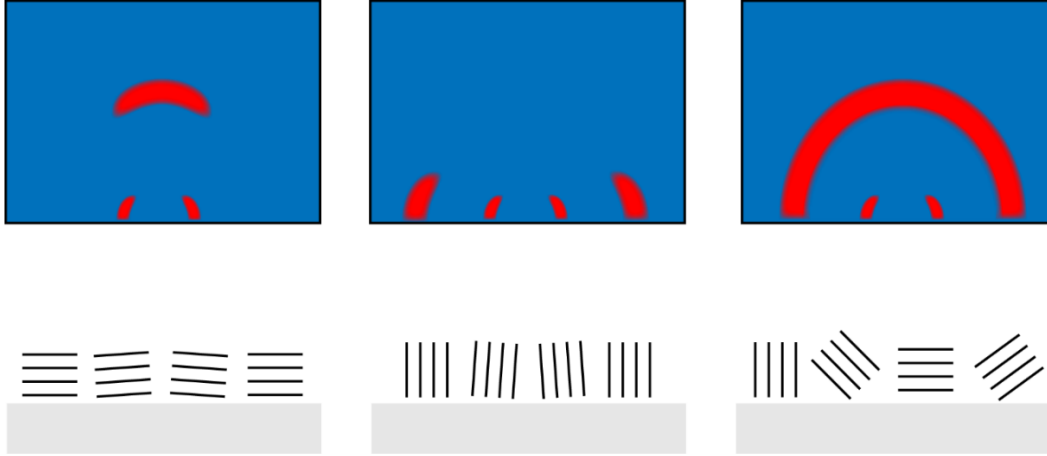
Figure 2.5. Different sample orientations and their scattering patterns.

To quantify the degree of orientation and the direction in which the orientation occurs, an Orientation Parameter (OP) can be defined as[27]

$$OP = \frac{\int I(\chi) \sin \chi \cos^2 \chi \, d\chi}{\int I(\chi) \sin \chi \, d\chi}. \tag{2.6}$$

Scenario 1 in Figure 2.5 would have an OP of 1, Scenario 2 would have an OP of 0, and Scenario 3 would have an OP of 0.33. It should be noted that this is over the full azimuthal range of 0 to 90°. Often times the Yoneda peak that occurs in GIXS prevents integrating the scattering intensity near 90° and reduces the integration range. As an example, an isotropic scattering peak integrated over 0 to 70° would have an OP of ~0.486. The Orientation Parameter is a useful metric to compare large sets of samples across different chemistries and preparation conditions to understand the effect on domain and crystalline orientation.

2.2.4 Calculation of the Relative Degree of Crystallinity

Related to the Orientation Parameter is the relative degree of crystallinity (rDoC), which is defined as

$$rDoC = \frac{1}{l_{path}} \int I(\chi) \sin \chi \, d\chi, \tag{2.7}$$

where l_{path} is a correction for path length through samples of different thicknesses. To calculate the relative degree of crystallinity, pole figures must be constructed from scattering images and then integrated over χ. Because scattering occurs spherically and the scattering pattern is collected on a flat area detector, there are distortions in a single image that must be corrected. Figure 2.6 shows uncorrected and corrected GIWAXS images, which demonstrates a missing piece of reciprocal space. This correction is done by converting the detector image into the sample reference frame. Based on the distance and incidence angle, each pixel can be assigned correct values for q_z, q_p, and χ.[28] For very large scattering angles, a polarization correction may be necessary,[29] but in our experience is not needed for the crystalline peak found in PFSA ionomers.
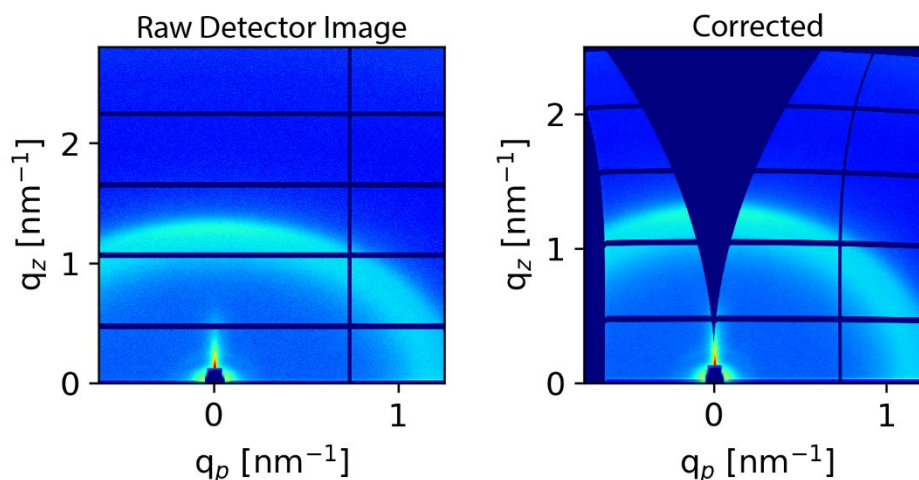
Figure 2.6. Raw and corrected 2D GIWAXS images. The wedge in the corrected figure is a missing piece of reciprocal space.

To fill in the missing portion of reciprocal space, an additional scattering image is taken at an incidence angle that is equal to the scattering angle for the peak of interest. This is known as the local specular condition. For the grazing incidence and local specular images, a sector cut is taken at a given χ value, the background is subtracted, and the scattering peak is integrated. This is repeated as a function of χ to generate the partial pole figures. For PFSA ionomers, the crystalline peak is convoluted with an amorphous peak; in addition to subtracting the background, the two peaks are deconvoluted by fitting a double Gaussian model. Figure 2.7 shows both the grazing incidence and local specular images transformed into q versus χ, and the merging of partial pole figures to generate the complete pole figure.
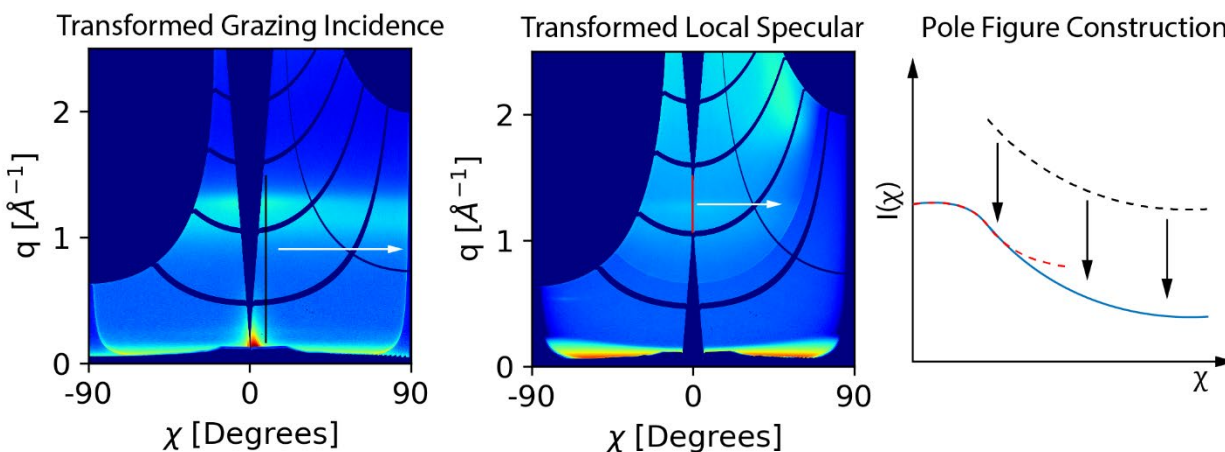
Figure 2.7. q versus χ plots for the grazing incidence and local specular conditions. Partial pole figures are generated from each image and the grazing incidence pole figure is scaled and merged with the local specular pole figure.

With each partial pole figure constructed, the grazing incidence pole figure is scaled to the local specular image. At the high incidence angle for the local specular condition, the EFI is

uniform through the depth of the film and will scale linearly with thickness. Once the full composite pole figure is merged, Equation 1.7 is used to integrate the pole figure and calculate *rDoC*. Similarly, OP can also be calculated from this pole figure using Equation 1.6. It should be noted that the relative degree of crystallinity is quantitative but can only be compared between samples that have the same crystal structure. Furthermore, it is relative in that one sample can be X-times as crystalline as another sample, but the absolute crystallinity for both samples is unknown.

2.2.5 Electric-Field Intensity and the Distorted Wave Born Approximation

At grazing-incidence angles close to the substrate's critical angle, a significant portion of the incident x-ray beam reflects off the substrate. This reflected beam interacts with the incident beam to create regions of high and low electric-field intensity (EFI). Figure 2.8 diagrams this interference.

Figure 2.8. Interference of incident and reflected x-ray beams, leading to regions of high and low electric field intensity.

When the two beams are in phase with each other, their amplitudes add to create regions of high EFI or anti-nodes. When the two beams are out of phase, their amplitudes cancel and lead to low intensity nodes. The EFI can vary an order of magnitude over angstroms or nanometers and is dependent on the incidence angle, the materials present, and the x-ray energy. Because the scattering is proportional to the local electric field, the large distribution in EFI leads to distortions in the scattering pattern relative to a transmission scattering experiment. Figure 2.9 compares the two scattering geometries and illustrates the differences between them.
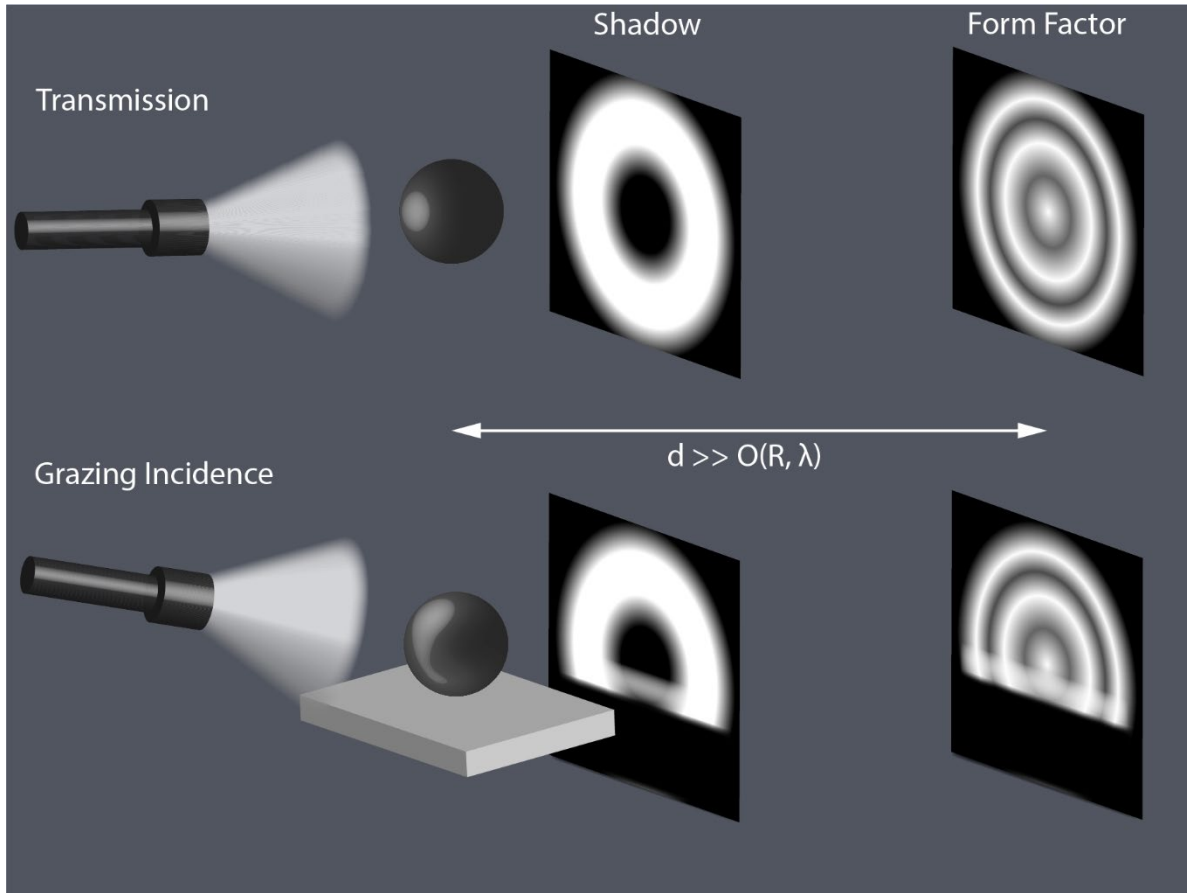
Figure 2.9. Schematic of the differences between transmission and grazing-incidence scattering and the resulting scattering pattern.

At a high level, the form factor can be thought of as a long-distance shadow that forms when an object is illuminated with a light source, which is represented here by a flashlight. In a transmission geometry, the flashlight illuminates the sphere uniformly and creates a uniform shadow and form factor. Scattering in transmission geometries is well described within the Born Approximation. With grazing incidence, the flashlight is now illuminating the sphere at some incidence angle. The light source shift and the presence of the substrate causes a non-uniform illumination of the sphere. Portions of the shadow and form factor are cut off entirely due to the substrate, and a region of high observed scattering intensity is present near the substrate horizon. Scattering must now be described within the Distorted-Wave Born Approximation (DWBA). Section 2.3 describes the DWBA in detail and describes a method to use the locally varying EFI as a depth-probe for thin films.

2.3   Electric Field Intensity Modulated Scattering as a Thin-Film Depth Probe

A large body of literature exists covering theory of the DWBA scattering cross-section in grazing-incidence geometry for both x-ray and neutron scattering;[30-35] this past work is reviewed briefly before extending these results to EFI-modulated scattering.

The total scattering cross-section for a rough film is shown below in Equation 1.[26]

$$\frac{d\sigma}{d\Omega} = \left(\frac{d\sigma}{d\Omega}\right)_{Fresnel} e^{-Q_z^2 \sigma^2} + \left(\frac{d\sigma}{d\Omega}\right)_{diffuse} \tag{2.8}$$

The first term in Equation 1 is the specularly reflected x-ray beam, which is the Fresnel reflectivity multiplied by a Debye-Waller like factor that dampens intensity with increasing surface roughness, σ. This is what is measured in XRR experiments, but is often blocked in grazing incidence x-ray experiments to prevent the intense specular reflection from damaging the area detector. The second term in Equation 2.8 is the diffuse scattering cross-section, which includes scattering due to interfacial roughness, and scattering from any density fluctuations within the film. DWBA modifies the scattering cross-section from the Born Approximation (BA) to account for multiple scattering events and has been generalized to rough multilayers for specular and non-specular XRR[36-37] and diffuse scattering from buried nanostructures.[35]

The multilayer DWBA expression for diffuse scattering derived by Jiang et. al[35] is

$$\left(\frac{d\sigma}{d\Omega}\right)_{diffuse} \approx r_e^2 \left\langle \left| \sum_{j=1}^{N+1} \sum_{m=1}^{4} \Delta\rho_j D_j^m F_j(\boldsymbol{q}_{||}, q_z^m) S_j(\boldsymbol{q}_{||}, q_z^m) \right|^2 \right\rangle, \tag{2.9}$$

where r_e is the classical electron radius, $\Delta\rho$ is the electron density contrast, $F_j(\boldsymbol{q}_{||}, q_z^m)$ is the form factor, $S_j(\boldsymbol{q}_{||}, q_z^m)$ is the structure factor, and D_j^m and q_z^m are defined as

$$\begin{aligned}
D_j^1 &= T_j^f T_j^i & q_j^1 &= k_{z,j}^f - k_{z,j}^i \\
D_j^2 &= R_j^f T_j^i & q_j^2 &= -k_{z,j}^f - k_{z,j}^i \\
D_j^3 &= T_j^f R_j^i & q_j^3 &= k_{z,j}^f + k_{z,j}^i \\
D_j^4 &= R_j^f R_j^i & q_j^4 &= -k_{z,j}^f + k_{z,j}^i
\end{aligned}$$

$T_j^{i,f}$ and $R_j^{i,f}$ are the transmitted and reflected complex amplitudes of the incoming and final waves, respectively. The z-component of the wavevector for each of these transmitted and reflected waves is $\pm k_{z,j}^{i,f}$.

Equation 2.9 takes in to account the local EF) varying across the depth of a scatterer, which can significantly distort the observed scattering pattern. EFI is defined as

$$EFI = \left| T^i e^{-ik_z^i z} + R^i e^{ik_z^i z} \right|^2. \tag{2.10}$$

Equation 2.9 can be cast into a form that shows an explicit dependence on the EFI. To do this, we note that the q_z^m dependence of the form and structure factors is just $e^{iq_z^m(z_j)z_j}$. Pulling this term out, part of Equation 2.9 can be refactored to show the initial and final wave eigenstates within the cross-section

$$\sum_{m=1}^{4} D_j^m e^{iq_z^m(z_j)z_j} = \left(T_j^i T_j^f e^{iq_z^1(z_j)z_j} + T_j^i R_j^f e^{iq_z^2(z_j)z_j} + R_j^i T_j^f e^{iq_z^3(z_j)z_j} + R_j^i R_j^f e^{iq_z^4(z_j)z_j} \right), \tag{2.11}$$

16

$$\sum_{m=1}^{4} D_j^m e^{iq_z^m(z_j)z_j} = \left(T_j^i e^{-ik_{z,j}^i z_j} + R_j^i e^{ik_{z,j}^i}\right)\left(T_j^f e^{ik_{z,j}^f z_j} + R_j^f e^{-ik_{z,j}^f}\right), \qquad (2.12)$$

Where the first and second grouping of terms are the z-components of the initial $\left(\psi_j^i\right)$ and final $\left(\psi_j^f\right)$ wave eigenstates, respectively. Plugging these terms back into Equation 2.9, we arrive at

$$\left(\frac{d\sigma}{d\Omega}\right)_{diffuse} \approx r_e^2 \left\langle \left|\sum_{j=1}^{N+1} \Delta\rho_j \psi_{z,j}^i \psi_{z,j}^f F_j(\mathbf{q}_{||}) S_j(\mathbf{q}_{||})\right|^2 \right\rangle. \qquad (2.13)$$

Continuing, if the scattering between layers is not coherent, then the sum can be taken outside the squared modulus and ensemble averaging. This leads to

$$\left(\frac{d\sigma}{d\Omega}\right)_{diffuse} \approx r_e^2 \sum_{j=1}^{N+1} |\Delta\rho_j|^2 |\psi_{z,j}^i|^2 |\psi_{z,j}^f|^2 \left\langle |F_j(\mathbf{q}_{||})|^2 \right\rangle |S_j(\mathbf{q}_{||})|^2. \qquad (2.14)$$

Comparing Equations 2.10, 2.12, and 2.14, one can see that $|\psi_{z,j}^i|^2$ is the EFI within the layer j and the diffuse scattering of layer j is directly proportional to it. This provides the theoretical underpinning for EFI-modulated scattering. Incidence angle resolved (IAR) data is generated by collecting scattering images across a range of incidence angles. Intensity is sampled from a specific spot on the detector at each of these incidence angles to generate intensity versus angle, or IAR plots. This spot on the detector will be at a constant k_z^f and $q_{||}$, so the only varying component of the diffuse scattering cross section is the local EFI present wherever the scatterer resides that is contributing to the signal on the detector (i.e. $I(\alpha_i) \propto EFI(\alpha_i)$). In this way, IAR data can be modeled using EFI calculations to provide depth information about the sample, including sample thickness, index of refraction, and where scatterers reside within a film. This modeling is simpler compared to traditional DWBA calculations because the form and structure factors do not need to be known; they are constant at fixed k_z^f and $q_{||}$. Finally, while this may be more complicated for systems where scattering is correlated between layers, modeling IAR data with EFI calculations may be a good approximation if the cross terms are small in Equation 2.13.

2.3.1 EFI Calculations

To calculate the EFI throughout a film, we use Parratt's recursion,[38] as laid out in M. Tolan's monograph *X-Ray Scattering from Soft-Matter Thin Films*.[39] These equations are derived for s-polarized x-rays, as typically produced by synchrotron bending magnets and undulators.

A sample is divided into N+1 layers, and the ratio of reflected to transmitted waves is calculated via Equation 2.15

$$X_j = \frac{R_j}{T_j} = e^{-2ik_{z,j}z_j} \frac{r_{j,j+1} + X_{j+1}e^{2ik_{z,j+1}z_j}}{1 + r_{j,j+1}X_{j+1}e^{2ik_{z,j+1}z_j}}, \qquad (2.15)$$

where

$$r_{j,j+1} = \frac{k_{z,j} - k_{z,j+1}}{k_{z,j} + k_{z,j+1}} \qquad k_{z,j} = k\left(n_j^2 - \cos^2 \alpha_i\right)^{\frac{1}{2}}.$$

and n_j is the complex index of refraction in layer j, α_i is the incidence angle, and k is the x-ray wave vector in vacuum. $r_{j,j+1}$ is the Fresnel reflection coefficient at the interface between layers j and $j + 1$. The substrate is assumed to be thick enough such that no reflections occur and $R_{N+1} = 0$. Starting at $j = N$, X_j is calculated recursively up to layer $j = 1$, where T_1 has been normalized to 1 and so $X_1 = R_1$ is known. $|R_1|^2$ is the specular reflection as measured in traditional x-ray reflectivity experiments.

Using Equations 2.16 and 2.17, the complex wave amplitudes through the rest of the film can be calculated

$$R_{j+1} = \frac{1}{t_{j+1,j}}\left[T_j r_{j+1,j} e^{-i(k_{z,j+1}+k_{z,j})z_j} + R_j e^{-i(k_{z,j+1}-k_{z,j})z_j}\right] \tag{2.16}$$

$$T_{j+1} = \frac{1}{t_{j+1,j}}\left[T_j e^{i(k_{z,j+1}-k_{z,j})z_j} + R_j r_{j+1,j} e^{i(k_{z,j+1}+k_{z,j})z_j}\right] \tag{2.17}$$

where

$$t_{j+1,j} = 1 + r_{j+1,j}.$$

Layer roughness can be incorporated via the Fresnel coefficients or treated as a graded interface with as smoothly varying index of refraction between the two layers. Once the reflected and transmitted complex wave amplitudes are known for each layer, the EFI can be calculated using Equation 2.10.

Calculating the EFI through a film as a function of incidence angle leads to EFI maps as shown in Figure 2.10.
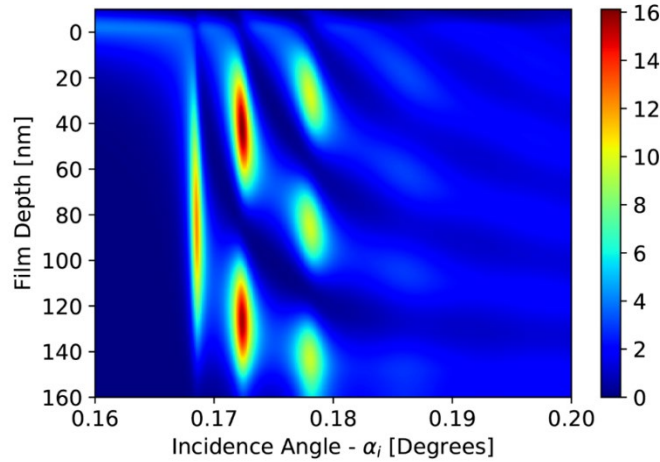
Figure 2.10. EFI map for a 150 nm Nafion thin film at 10 keV. Nafion is a perfluorinated sulfonic-acid ion-conducting polymer commonly used in fuel cells. The air-film and film-substrate interfaces are at 0 and 150 nm, respectively.

At specific incidence angles, the incoming x-ray beam couples into the film, leading to transverse electric (TE) modes and large EFI enhancement at certain depths within the film. The

angle- and depth-dependence of the EFI is what allows researchers to determine the *z*-position of specific atoms or scatterers within a sample. EFI-modulated fluorescence has been used to depth-probe surface-ion distributions[40-42] and polymer nanocomposites,[43] and GIXS data modeled with the multilayer DWBA has elucidated the positions of nanoparticles within polymer thin films.[44-46] More recently, EFI principles were applied to reveal stratification of crystallite orientation in semi-conducting polymer thin films based on modulation in diffraction peak intensities.[47] Our work applies these principles to develop a general depth-probe for thin-film systems using the specular rod signal in GIXS.

The EFI map in Figure 2.10 is calculated assuming a monochromatic plane wave. At a beamline, sources will have a finite angular divergence and energy resolution and may need to be accounted for depending on the magnitude of these values. These effects are considered using the energy resolution and angular divergence from Beamline 7.3.3 at the Advanced Light Source,[48] where the experimental data was taken.

2.3.1.1 Energy Resolution and Angular Divergence

To calculate the effect of finite energy resolution, EFI maps at each energy are calculated and then summed, weighted by the energy spectrum probability distribution function. The FWHM at 7.3.3 is ~100 eV and the full energy spectrum is shown in Figure 2.11. Correspondingly, the index of refraction for the film and substrate must also be adjusted for each energy, which are calculated here using the Center for X-Ray Optics (CXRO) online calculator.[49]
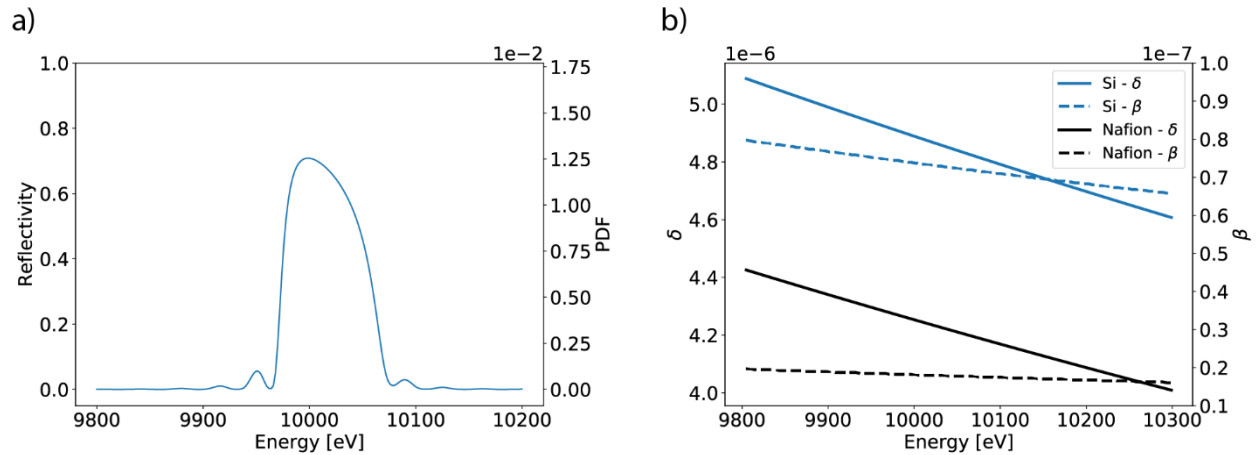
Figure 2.11. a) Reflectivity and probability distribution function (PDF) plotted versus energy for Beamline 7.3.3 at the Advanced Light Source. b) Real and imaginary parts of the index of refraction for Nafion and silicon versus energy.

Figure 2.12a compares the average EFI of a polymer thin film on silicon for a monochromatic wave with the energy resolution for 7.3.3. The relatively large energy resolution for 7.3.3 reduces the modulation magnitude and slightly shifts the positions of TE modes. This will be taken in to account for further calculations below. For beamlines that use a Si crystal (FWHM ~2 eV at 10 keV) or similar monochromator, this effect should be negligible at hard x-ray energies. More broadly, the impact of energy resolution will depend on how quickly the index of refraction changes for a given material, which is a function of the chemical makeup and the

energy range over which it is considered. It is expected that energy resolution will have a greater effect at lower energies where the index of refraction changes more quickly with energy.

a)

b)
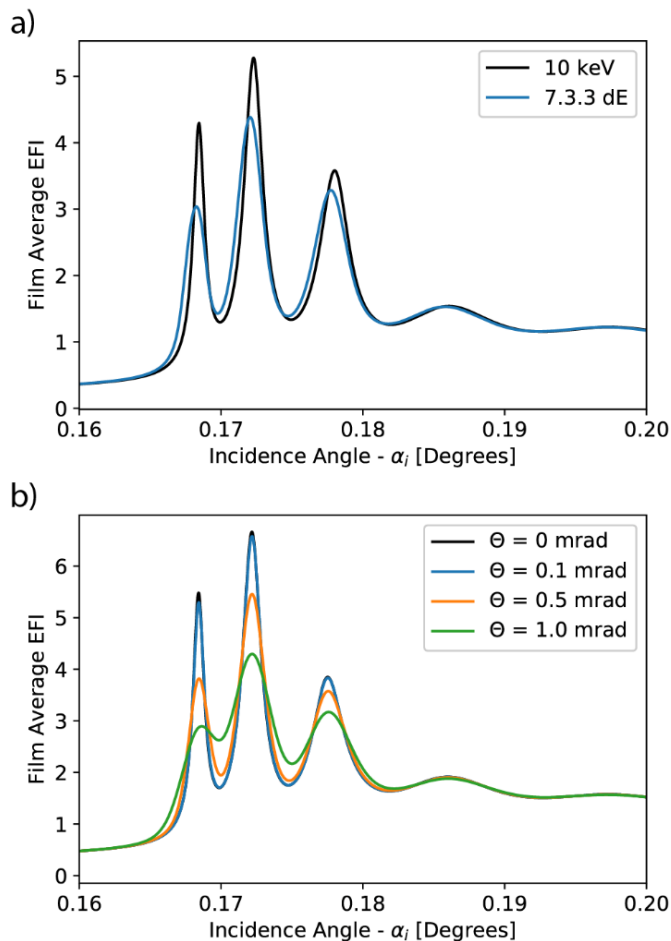
Figure 2.12. a) The average EFI for a 150 nm Nafion film calculated at 10 keV and the energy resolution of 7.3.3. b) Average EFI for the same Nafion film calculated for various values of angular divergence. 7.3.3's angular divergence is measured to be less than 0.1 mrad.

The second effect that may need to be accounted for is the angular divergence of the beam. At 7.3.3, this has been measured to be less than 0.1 milliradians. The divergence is approximated by convolving the EFI for a plane wave with a Gaussian distribution in incidence angle. Figure 2.12b shows the effect of multiple values of angular divergence. For 7.3.3's angular divergence, the effect on the EFI is negligible, and is neglected for further calculations.

2.3.2   Data Collection and Analysis

We demonstrate EFI-modulated scattering first with a set of single-layer polymer thin films of varying thickness to show how IAR data can be used to determine the index of refraction and thickness. Second, a set of bilayer thin films is analyzed to show that multiple sources of scattering can be depth resolved. The data collection and analysis for both sets of films is the same: Short-exposure GIXS images are taken across a range of incidence angles and the same area from each

image is binned into an intensity value to generate intensity versus incidence angle or IAR plots. Sets of IAR data are generated from scattering at layer interfaces (the "specular rod") and scattering peaks due to a layer's internal structure, respectively. Due to its strong scattering signal, the specular rod IAR data is fit using EFI calculations and the optimized fit is compared with the additional IAR data to confirm layer ordering. The multiple sets of IAR data from the specular rod and internal structure could potentially be co-refined; to do so, background contributions to the internal-structure IAR data would need to be accounted for because of its weaker signal. Figure 2.13 schematically shows the data collection and analysis procedures.
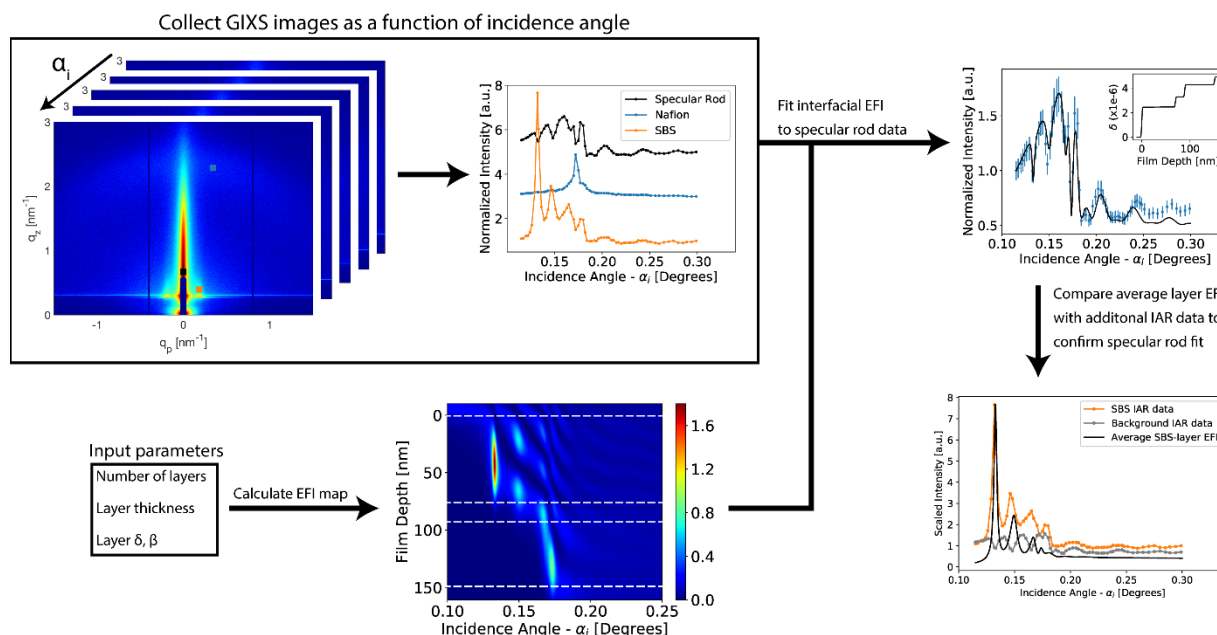
Figure 2.13. Data collection and analysis procedure.

The specular rod signal is due to interfacial roughness which causes the incoming x-ray beam to be scattered/reflected with some small change in q_x, q_y; this is proportional to the EFI at each of the interfaces present within a film. In the same way that knowledge of form and structure factors is not required, the specular rod signal can be broken down into the relative contributions from each interface without having to know the respective height-height correlation functions. Below the critical angle (α_c), an evanescent wave penetrates only a few nanometers into the film and for layers thicker than this penetration depth, only the top interface contributes to the specular rod signal for $\alpha_i < \alpha_C$. An EFI map for a film is calculated given input parameters of thickness, and the real (δ) and imaginary (β) parts of the index of refraction for each layer. The top surface from the calculated map is scaled to the specular rod IAR data below the critical angle and subtracted. The remaining intensity is from the EFI at the bottom interface for single layer films and from a combination of the EFI at the remaining interfaces in multilayer films. For very thin films, the evanescent wave will "see" the bottom layer below the critical angle, which may necessitate simultaneous fitting of the relative contributions. Each of these procedures are incorporated into respective differential evolution fitting routines to minimize error between the data and model using the SciPy python package.[50]

2.3.2.1   Single Layer Films

Thin films of Nafion (an ion-conducting polymer commonly used in fuel cells) were cast at 8 different thicknesses and sets of GIWAXS images were taken at incidence angles from 0.12°-0.25°. Film thickness, δ, β, and a scaling constant are the fitting parameters. Additionally, the sample alpha alignment procedure at 7.3.3 is not perfect and appears to shift the true incidence angle by up to 0.02°. This offset is determined by externally iterating through offset values to find a minimum in the fitting error.

Figure 2.14 shows experimental specular rod data and the fit for two films of different thicknesses, showing the contributions from the top and bottom interfaces. Nafion is a semi-crystalline polymer, and, in addition to the specular rod, the diffraction peak corresponding to the $\langle 100 \rangle$ lattice plane is also sampled to generate IAR data. Figure 2.14b/c plots this IAR data along with the average film EFI, using the parameters extracted from fitting the specular rod. These also show good agreement, suggesting crystallites are present throughout the entire film depth.
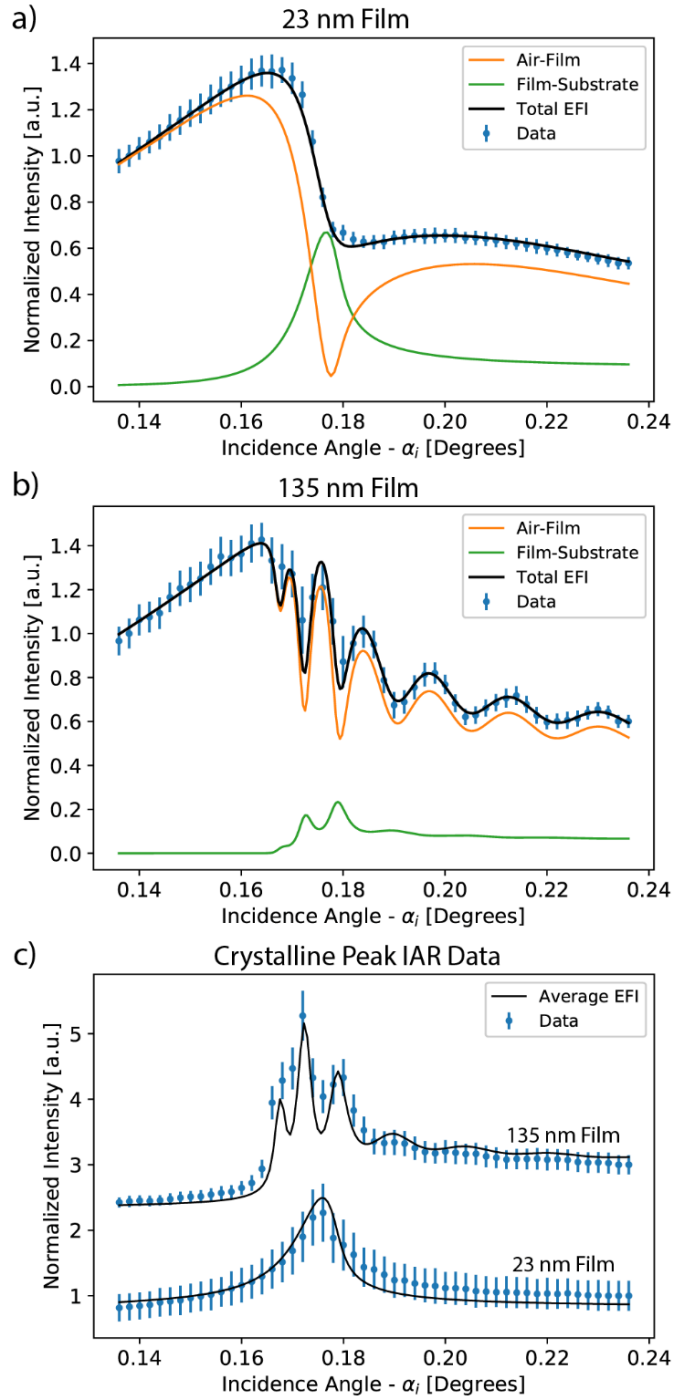
Figure 2.14. EFI-modulated scattering intensity data and model for a) 23 nm and b) 135 nm film thicknesses. The overall signal has contributions from the air-film and film-substrate interfaces, which is dependent on film thickness, and roughness and contrast at each interface c) For each film, the average EFI is plotted alongside IAR data generated from sampling the crystalline peak of Nafion. The agreement between data and model indicate crystallites are present throughout the film. Data in c) has been vertically shifted for clarity.

Each of the 8 samples' specular rod data is fit, and the film thickness extracted from fitting is plotted versus film thickness measured via ellipsometry (Figure 2.15). Across an order of magnitude in film thickness, there is excellent agreement between the two techniques. Continuing, the real part of the index of refraction at 10 keV is plotted versus film thickness in Figure 4b. At larger film thickness, δ is close to the value estimated from CXRO using the bulk membrane density of Nafion. Below 40 to 50 nm, δ steeply decreases as the films become less dense; this transition point in δ occurs in the same thickness range where prior studies observed changes in this material's physical properties.[4, 13]
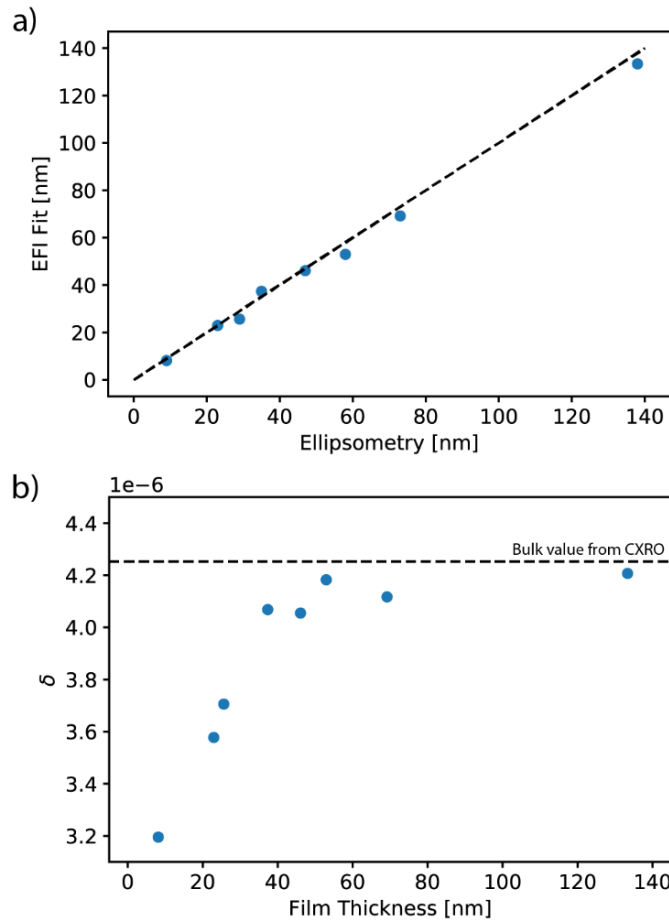
Figure 2.15. a) Film thickness extracted from EFI fitting plotted versus film thickness measured via ellipsometry. The dashed line is a 1:1 value between the two axes b) Real part of the index of refraction plotted versus film thickness at 10 keV. The dashed line represents the δ value estimated from CXRO using bulk Nafion density ($\rho = 2.1$ g cm^{-3}).

2.3.2.2 Bilayer Films

Two bilayer samples were prepared by spin casting Nafion and poly(styrene-b-butadiene-b-styrene) (SBS) layers on top of each other. These materials were chosen because they both exhibit scattering peaks in the accessible q-region for 3.6m GISAXS and can be cast from orthogonal solvents to form a macroscopically smooth thin film. Nafion is spun cast from a water/n-propanol solution and is a weakly phase separated material with a broad isotropic ring at 2.5 nm^{-1}. SBS is spun cast from a toluene solution and exhibits lamellar morphology with an anisotropic peak centered in plane at 0.17 nm^{-1}.
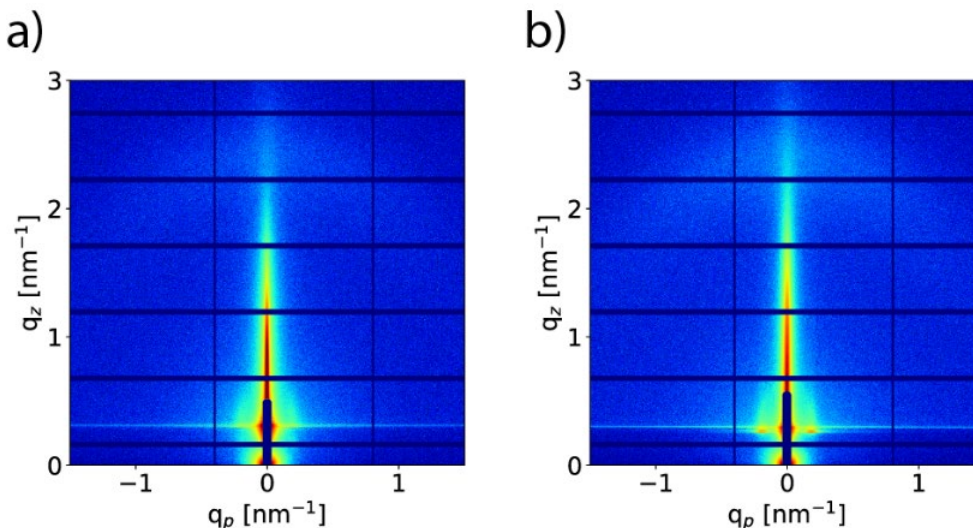
Figure 2.16. 2D GISAXS images of Nafion-SBS bilayer thin films. a) Scattering of Sample 1 at $\alpha_i = 0.163°$ b) Scattering of Sample 2 at $\alpha_i = 0.172°$. The incidence angles were chosen such that visibility of both scattering peaks is maximized.

Sample 1 is SBS spun cast first, then Nafion; Sample 2 is Nafion spun cast first, then SBS. Figure 2.16 shows the 2D GISAXS images for both samples. There are only small differences in the scattering patterns, and it would be difficult to discern the order of each layer from a single image. To distinguish between them, data is collected as a function of incidence angle to generate IAR data. Three regions of interest were chosen for these samples. One at the scattering peak due to Nafion, one at the scattering peak due to SBS, and one at the specular rod. Figure 2.17a,b shows the IAR plots for the three regions of interest.
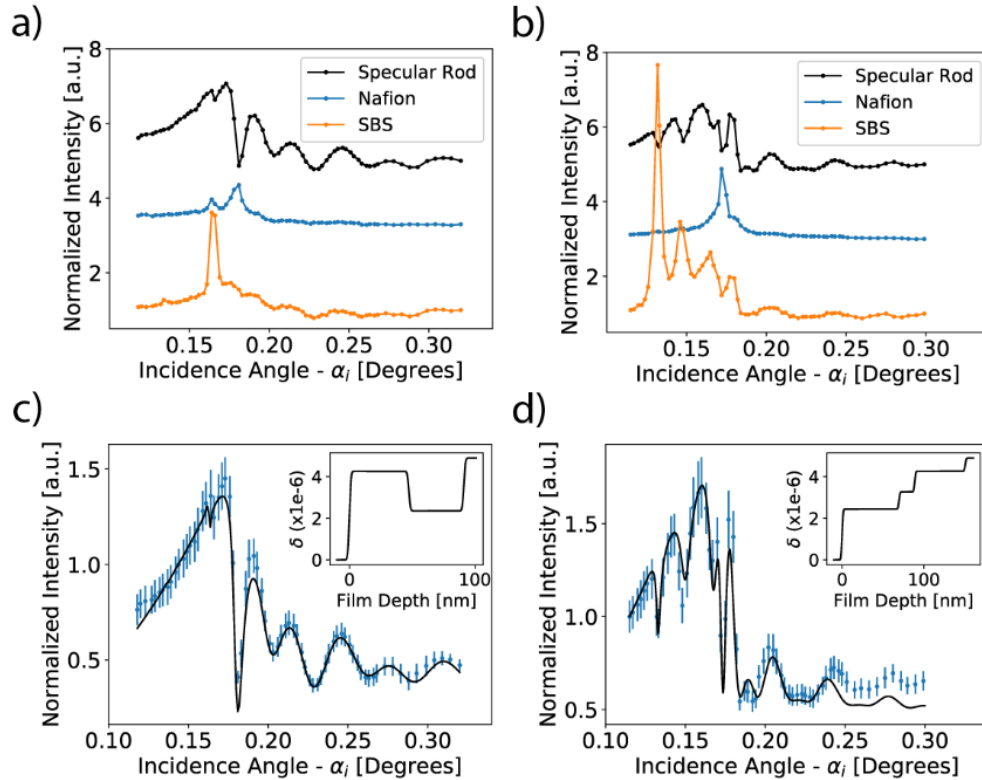
Figure 2.17. a), b) IAR data sets for each sample. c), d) Fits of the specular rod data with the resulting electron density profile shown inset.

Each data set is normalized by their last value to compare the degree of signal enhancement/modulation. All three IAR data for each sample show different modulations in the scattering intensity corresponding to their unique z-positions within the sample. There is a clear difference between the specular rod IAR data for Sample 1 and Sample 2 that is less apparent with a single GISAXS image. SBS IAR data between samples is also distinctly different, highlighting that SBS is present at different depths between samples. In Sample 2, the higher electron density of the Nafion underlayer creates multiple TE modes in the SBS with an almost 8 times higher intensity at the 1st TE mode compared to higher incidence angles. For weakly scattering samples, shooting at the incidence angle for a specific TE mode could be useful for enhancing scattering above the background.

To extract further information, the specular rod IAR data is fit using the same differential evolution algorithm. The fitting parameters are the thickness of each layer, the index of refraction of SBS, and the relative contribution from the buried interfaces. The index of refraction for Nafion is held constant at the bulk film value because these layers are expected to be thicker than the transition point observed in the single layer films.

The specular rod fit and extracted electron density profile for Sample 1 are shown in Figure 2.17c, which is fit well with a two layer model. For Sample 2, a 20 nm-thick interlayer of intermediate electron density is needed between the SBS and Nafion layers to adequately fit the specular rod data (Figure 2.17d). This layer is not present in Sample 1, indicating that Nafion is partially soluble in toulene while SBS is insoluble in water/nPA. Though all the features in the data are recreated, further agreement at $\alpha_i > 0.225°$ may be achieved by also fitting Nafion's

index of refraction. Contributions to the total specular rod signal from each of the interfaces for Samples 1 and 2 are plotted in Figure 2.18.
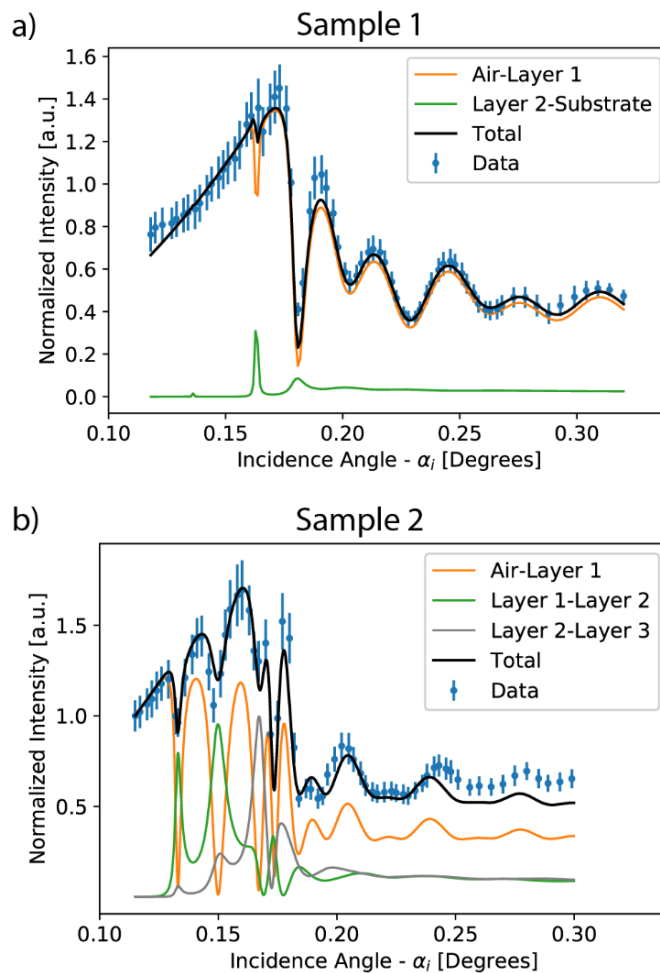
Figure 2.18. Breakdown of contributions to the total specular rod signal for a) Sample 1 and b) Sample 2.

Each sample has a unique combination of EFI signal from the different interfaces which is a function of layer ordering and roughness. In Sample 1, the Nafion/SBS interface does not appear to contribute to the specular rod signal. As x-rays propagate downwards and encounter this interface, they are more likely to refract/scatter downward into the lower electron density SBS underlayer, rather than upwards which would contribute to the specular rod signal. Moreover, the bottom-layer/silicon interface has a small contribution to the signal for Sample 1 and no apparent contribution to the signal for Sample 2. This is ascribed to polished silicon's low surface roughness, especially in comparison to polymer/polymer and polymer/air interfaces.
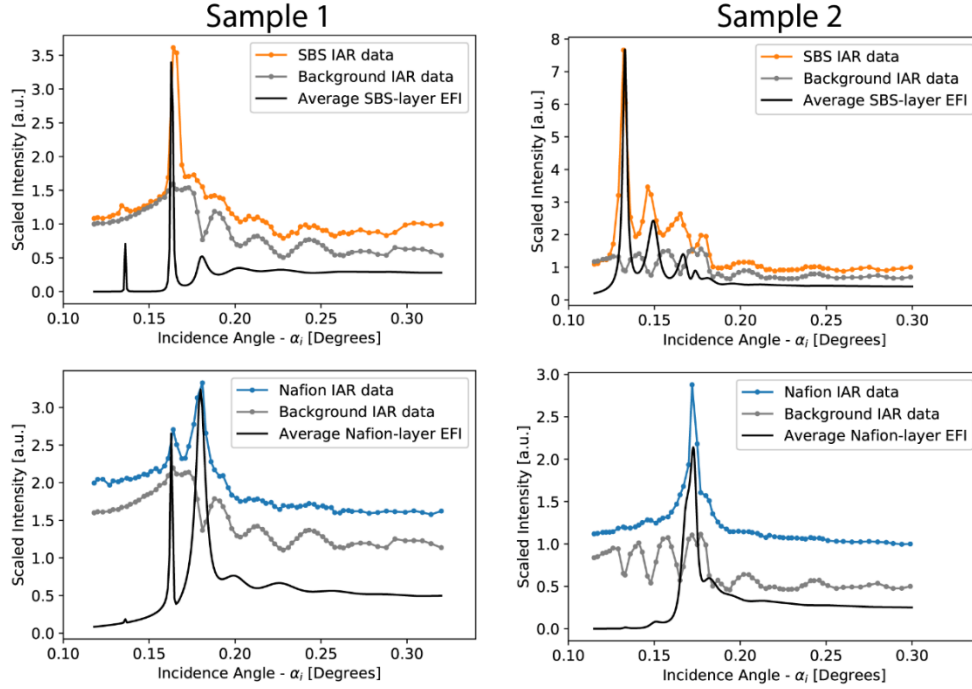
Figure 2.19. Comparison of Nafion and SBS IAR data with background IAR data and calculated average layer EFI.

Using the optimized parameters from fitting the specular rod, the average layer EFI is plotted with the IAR data from the SBS and Nafion peaks in the data (Figure 2.19). For both Sample 1 and Sample 2, there is good agreement between the position of the TE modes within each layer, which confirms their respective positions within the film. However, since the scattering signal from SBS and Nafion is relatively weak, there is also a contribution from background that scales similarly to the specular rod. Away from the TE modes in each layer, the Nafion and SBS IAR data have similar modulations to the background IAR data. While the specular rod appears as a sharp rod near $q_p = 0$, scattering from interfacial roughness extends in q_p and q_z with some non-zero intensity and contributes to observed EFI modulations in weakly scattering signals. While this technique has the potential to elucidate significantly more information from grazing incidence scattering images, various contributions to the observed EFI modulation must carefully accounted for.

28
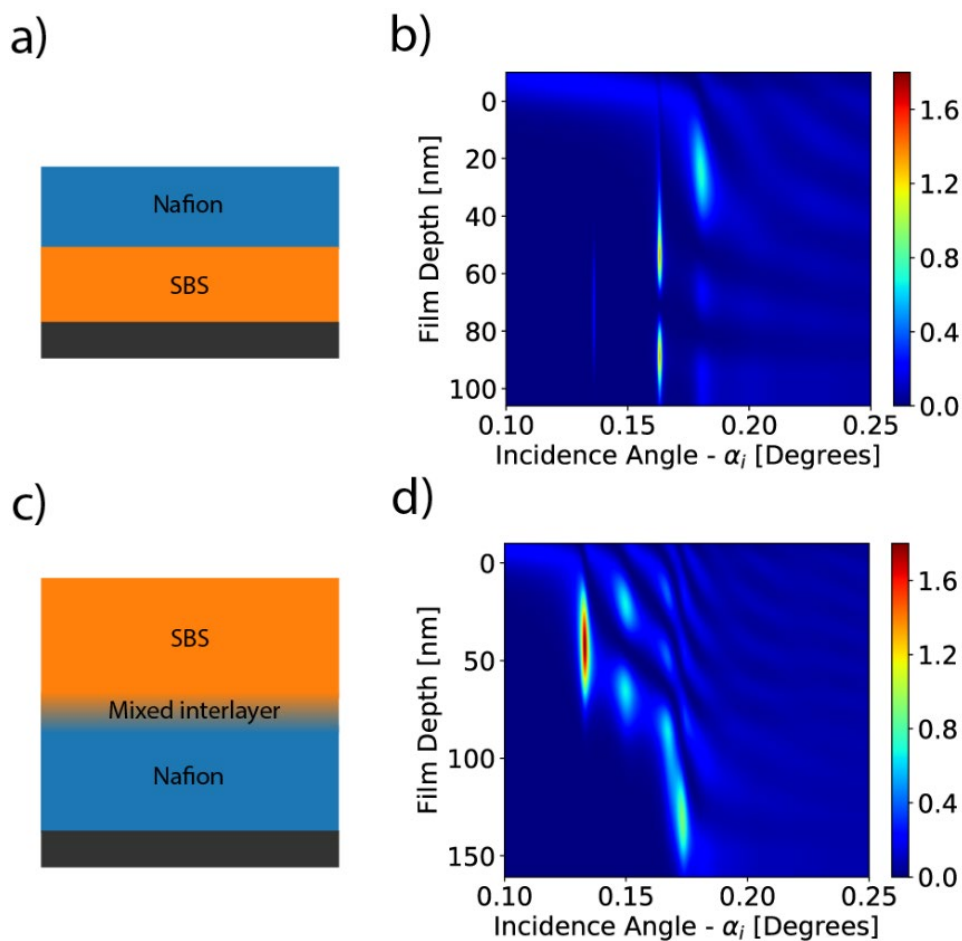
Figure 2.20. a), c) A schematic of each film, illustrating the layer ordering and b), d) full EFI maps for each sample.

Figure 2.20 shows a schematic of each film and the full EFI maps, which help illustrate where specific peaks in the IAR data occur spatially within the film. The layering of Sample 1 leads to interesting and subtle features observed in the IAR data. The dip in the specular rod signal and peaks in the Nafion and SBS IAR data at $\alpha_i = 0.163°$ is unexpected (Figure 2.18a), since this is below the critical angle of Nafion, but is explained through the full EFI map (Figure 2.20b). At this incidence angle, the evanescent wave penetration depth is high enough to reach and couple into the SBS underlayer leading to TE modes in the SBS layer and higher EFI in the Nafion layer. EFI-modulated scattering could be applied to thin film waveguides to study behavior like this in more detail.

Using EFI-modulated scattering, the difference between these two samples is easily identified and the source of each scattering signal can be mapped depth-wise by fitting IAR data. Significantly more information is elucidated when compared to a single or few scattering images, and the data can be modeled without knowledge of the form or structure factors. Furthermore, the technique is inherently *in situ*, and does not require any special experimental set-up beyond what is required for GIXS. This enables the film thickness and index of refraction to be tracked without additional equipment to connect macroscopic properties with nanostructural morphology changes in one experiment. The intense specular rod signal allows for short exposure times to depth resolve

transport and thermodynamic phenomena occurring on the order of seconds to minutes, including nanoparticle diffusion and the ordering of polymer systems.

Beyond *in-situ* experiments, EFI-modulated scattering can be applied to characterize any thin film system. Organic electronics, polymer nanocomposites, and layer-by-layer films are all examples of systems where critical processes occur through the depth of the film. EFI-modulated scattering has the ability to define through-plane ordering with considerable detail, which opens up a new paradigm for characterization and enables more robust structure-property relationships in these and other materials.

2.3.3 Beamline Integration

EFI-modulated scattering can be translated into a beamline plugin for on-line data analysis: A portion of the specular rod is selected on the detector over which to integrate intensity and an incidence angle scan is performed at short exposure times, integrating the region of interest (ROI) for each angle and returning the IAR data to the user. From these plots, critical angles and TE modes are easily identified, and the researcher can make a more informed decision on which incidence angles to collect longer exposures (e.g. at the 1st TE mode to maximize signal, or a specific TE mode to highlight some depth of the film). The current method reduces a set of 2D-data off-line; immediately returning the IAR data reduced into a text file will reduce the amount of data that needs processed by the researcher and facilitate more efficient material exploration.

Some grazing-incidence scattering beamlines have a diode installed as a reflectivity point detector in addition to an area detector, which would make sampling the specular rod somewhat redundant. Where this technique becomes useful even on beamlines with simultaneous reflectivity is the ability to sample multiple ROIs on the area detector. Multiple scattering peaks can be sampled simultaneously to generate IAR data for each peak that could then be co-refined with reflectivity data to precisely characterize the film morphology as a function of depth.

For this technique to be applied successfully, a few conditions are recommended. The first criterion is an x-ray source of small angular divergence and energy FWHM. As these increase, the magnitude of EFI signal modulation becomes smaller. The second criterion recommended is a goniometer with uncertainty in the incidence angle of less than $\sim 5\%$ ($\sim 0.005°$ for 10 keV). Uncertainty in the motor position could shift data points in a non-uniform way and lead to poorly resolved data. For longer sample-to-detector distances where the angular resolution per pixel is higher, an alternative strategy is to use the substrate's Yoneda peak position as an internal standard for calculating the incidence angle of each image.

2.4 Summary

X-ray scattering is introduced with some of the basic concepts relevant to soft matter research. Additional considerations are covered for grazing incidence x-ray scattering and the common concepts between transmission and grazing geometries are highlighted. The multilayer Distorted-Wave Born Approximation is reviewed, and its framework is used to show how incidence angle-resolved (IAR) data is proportional to the local electric field intensity (EFI). Applying these principles, we demonstrate how EFI-modulated scattering can be used to extract optical constants and film thickness from Nafion polymer thin films ranging from 10 - 140 nm. Extracted film thickness closely agrees with ellipsometry measurements and the electron density of Nafion thin films shows a decrease below 40 to 50 nm. This transition point is consistent with previous studies. Bilayer thin films of Nafion and poly(styrene-b-butadiene-b-styrene) are analyzed to show how multiple sources of scattering can be depth-resolved within a sample. EFI-

modulated scattering is a general technique, enabling *in-situ* optical characterization and depth profiling for any thin-film system.

3 Background and Technique Development for the Cantilever Bending Method

3.1 Introduction/Background

The mechanical characterization of PFSA ionomers is a key necessity in understanding their structure-property relationship. Numerous studies have shown a chemical-mechanical balance exists composed of driving forces related to water sorption by hydrophilic domains versus those due to mechanical pressure exerted by PFSA's hydrophobic domains. The mechanical properties of these materials dictate equilibrium water content and associated transport properties, and how these properties evolve over time will influence PFSA durability and performance.[2-3]

Within the catalyst layer, PFSA ionomer exists as a thin film where it is responsible for ion and reactant transport to electrocatalytic sites, and product transport away from these sites. As an example, oxygen transport is one of the limiting factors in fuel-cell performance, and this transport decreases with decreasing water content. Thus, to improve oxygen transport, it is important to be able to predict and control the water content in these materials. A similar chemical-mechanical balance should exist in PFSA thin films, so by characterizing and controlling the mechanical properties across chemistries, the water content of these materials can be predicted and optimized. Thus, one needs a reliable way to characterize the mechanical properties of thin films.

Mechanical characterization of thin films is more difficult compared to bulk membranes. As a thin film, the material needs to be supported on a substrate, making it a challenge to separate the mechanical response of the polymer from the mechanical response of the substrate. Nano-indentation is one method for thin-film mechanical characterization.[51] This experiment works by indenting a thin film with small, well-defined probe and measuring the force response as a function of indentation depth. By analyzing the force-displacement curves with a model of the probe geometry, a compressional modulus can be obtained. For very thin films though, the mechanical response can be dominated by the underlying substrate and separating the different contributions in the analysis is non-trivial.

Another technique for mechanical characterization of polymer thin films is a buckling-based method.[52] A polymer thin film is cast onto a hard substrate and then float-transferred to a PDMS underlayer. The sandwich-composite sample is stretched and differences in compliance between the two polymers causes buckling of the top polymer layer. The wavelength of these buckles is proportional to the modulus of the top polymer. Unlike nano-indentation, the mechanical properties of the PDMS underlayer and top polymer layer can be separated easily.

There are downsides to the buckling-based method though. The float-transfer method requires the thin films to be able to release cleanly from the silicon substrate. For PFSAs, this can be more difficult once annealed.[5] Catalyst layers are often heat treated, so being able to study the effect of annealing is important. The films may be annealed after transfer to the PDMS, but substrate interactions are an important factor to consider. Additionally, the soft rubbery interface of PDMS is different than the hard, non-compliant interface of silicon (or carbon in a catalyst layer) and how PFSA thin films are affected by this difference is an open question.

The second downside to the buckling-based method is the buckles that form are a plastic deformation, which means a supported film can only be tested once. It is desirable to test the mechanical properties at different environmental conditions (e.g., relative humidity (RH), temperature). Testing films at different conditions with the buckling method requires a new sample for each condition, increasing the number of samples that need to be made. The ability to study

the effect of repeated RH or temperature cycling is also desirable to understand effects of conditioning or "break-in" protocols, as well as long-term performance and durability. Since these cyclic tests cannot be performed with the buckling method, another experimental technique is required.

3.2 Cantilever Bending Method

The cantilever bending method is a mechanical characterization technique that can measure the mechanical response of thin films supported on a rigid substrate and does not have the drawbacks of nano-indentation or the buckling method. Samples can undergo annealing, the response of the film can be separated from the substrate, and sample deformation is elastic allowing for repeatable characterization. This method was originally conceived for thin films by G.G. Stoney in 1909.[53] He observed that electrochemically deposited metal films peeled off underlying glass substrates, and he was able to derive a relation for the curvature of the underlying substrate to stresses in the metal thin film. Stoney's thin film equation in its modern form is

$$\Delta F = \sigma t_f = \frac{E_s t_s^2 \Delta \kappa}{6(1 - \nu_s)},$$
(3.1)

where E_s is the Young's modulus of the substrate, t_s is the substrate thickness, ν_s is Poisson's ratio of the substrate, and $\Delta \kappa$ is the change in curvature of the substrate. The force per width applied on the cantilever, ΔF, is equal to the average stress in the thin film, σ, times the thickness of the thin film, t_f. If the material properties of the supporting substrate and the thickness of the thin film are known, Stoney's thin-film equation can be used to calculate the average stress in a film. Stoney's thin-film equation and the cantilever bending method has been used to study to thin-film deposition,[54-55] electrochemical lithiation and adsorption,[56-57] and residual stresses.[58-59]

This cantilever bending method was adapted by Page et. al. to measure PFSA thin film modulus.[60-61] PFSA thin films are spin cast onto ~100 μm-thick silicon wafers, and then diced into a cantilever (~4cm x 0.5cm). The sample is loaded into an environmental cell and the curvature of the silicon substrate is monitored using a laser (Figure 3.1).
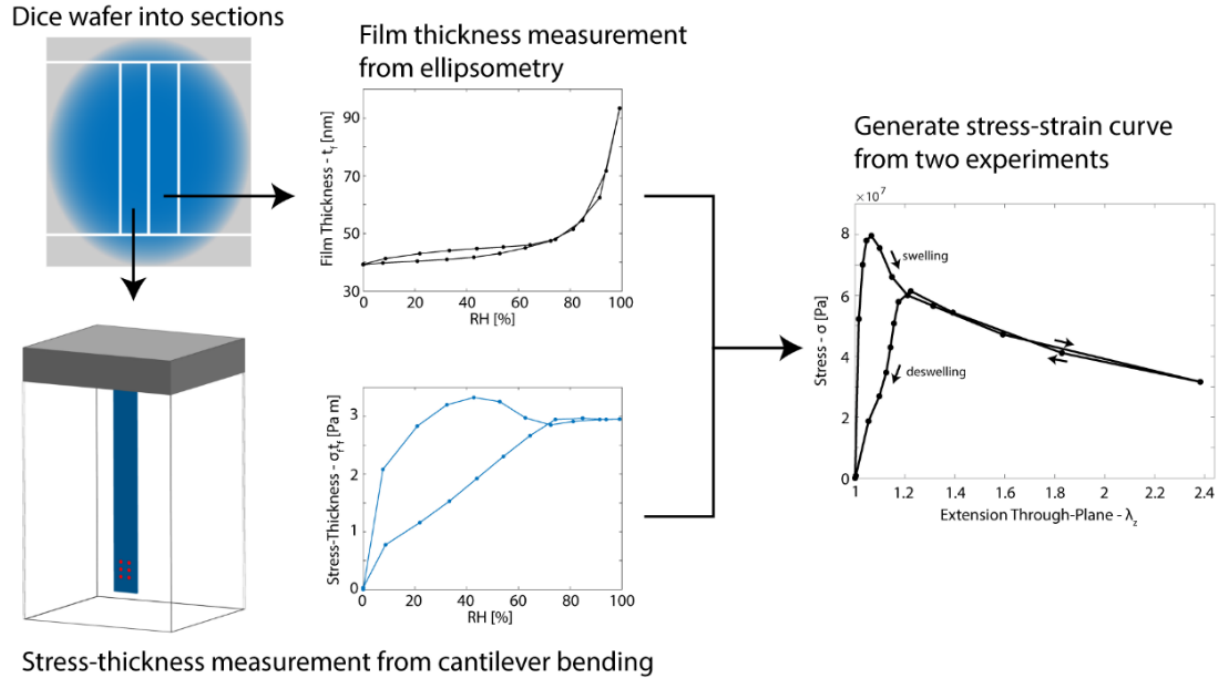
Figure 3.1. Overview of the cantilever bending method and ellipsometry experiments. Data from the two experiments are combined to generate stress-strain curves.

The environmental cell is humidified, which swells the PFSA thin film. The thin film wants to swell equally in all directions, but because it is confined to the underlying substrate it can only swell perpendicular to the substrate, or through-plane. This restriction in swelling causes an in-plane stress, which bends the substrate, changing the curvature. The sample is cycled through humidity steps to collect stress-thickness versus humidity. Another section of the larger sample is run on an ellipsometer to extract film thickness under the same humidity conditions. From these two experiments, stress-strain curves can be created. In the limit of zero deformation, the slope of the stress-strain curve is twice the shear modulus,

$$\lim_{\varepsilon_z \to 0} \frac{\partial \sigma}{\partial \varepsilon_z} = 2G. \tag{3.2}$$

Page et. al measured the mechanical response for Nafion thin films as a function of thickness, which demonstrated an increase in the modulus with decreasing thickness. A corresponding decrease in the equilibrium water content was observed with the increased modulus. This is likely responsible, in-part, for the increased transport resistances observed in PFSA thin films.

Because water sorption is causing the deformation/stress response, it is not possible with this method to measure mechanical properties while holding water content constant. It is desirable to have these mechanical properties as a function of water content, to build structure-property relationships and ultimately to predict water content in catalyst-layer thin films at different operating conditions. For bulk polymer networks, there exists theories derived from statistical mechanics to relate swelling to the equilibrium modulus. Below, these theories are applied to polymer thin films adhered to substrates.

3.3 Polymer thermodynamics and solid mechanics

Polymers are well-described using a statistical-mechanics approach relating chain stretching and stress to the shear modulus of rubbers and polymer networks. This description was extended to the swelling of crosslinked polymer networks by Flory and Rehner,[62] where they consider free-energy contributions from mixing of polymer and solvent, and elastic deformation of the polymer network,

$$f_{gel} = f_{el} + f_{mix}. \tag{3.3}$$

Flory-Rehner theory hypothesizes that polymer networks will swell until the change in free energy due to mixing is equal to the change in free energy due to chain deformation,

$$\Delta f_{gel} = 0 = \Delta f_{el} + \Delta f_{mix}. \tag{3.4}$$

The functional forms for free energy of elasticity and mixing vary depending on the polymer architecture, but the general theory has been very successful in describing the swelling of crosslinked polymers. This relationship is analogous to the chemical-mechanical balance observed in the swelling of PFSA membranes.[2-3, 63-65]

Applying Flory-Rehner theory with solid mechanics analysis, we can relate the stress exerted on the cantilever to the equilibrium modulus of the film. Using an affine network model and following Kang et. Al,[66] the free energy of elasticity for a crosslinked polymer is

$$f_{el} = \frac{1}{2} N k_b T \left(\lambda_x^2 + \lambda_y^2 + \lambda_z^2 - 3 - 2 \ln[\lambda_x \lambda_y \lambda_z] \right) + \Pi \left(1 + \nu C - \lambda_x \lambda_y \lambda_z \right), \tag{3.5}$$

where Π is the osmotic pressure, ν is the molar volume of the solvent, and C is the molar concentration of the solvent. λ is the extension ratio for the principle axes x, y, and z, and is defined as

$$\lambda = \frac{L}{L_o}. \tag{3.6}$$

The osmotic pressure term is a Lagrange multiplier, and we can include it under the assumption of molecular incompressibility. This assumption is only valid when a polymer is in the rubbery state; glassy polymers are not at thermodynamic equilibrium and violate the assumption of molecular incompressibility.

Taking the derivative of the free energy with respect to an extension ratio, λ_i, gives a principal stress, s_i, along that axes,

$$s_i = \frac{\partial f_{el}}{\partial \lambda_i} = N k_b T \left(\lambda_i - \frac{1}{\lambda_i} \right) - \Pi \lambda_j \lambda_k. \tag{3.7}$$

We can use the Equation 3.7 to determine the stresses for the swelling of a surface-attached thin film. In the plane there will be no change in dimensions, and $\lambda_x = \lambda_y = 1$. Through-plane, there

is no external resistance to swelling and $s_z = 0$. Plugging these values into the above equation for stress we arrive at

$$\Pi = Nk_bT\left(\lambda_z - \frac{1}{\lambda_z}\right). \tag{3.8}$$

What Equation 3.8 tells us physically is that the polymer network will swell until the elastic pressure is equal to the osmotic pressure, which is the original hypothesis of Flory and Rehner. Plugging this result back into the stress equation for the x and y axes leads to

$$s_x = s_y = -\Pi\lambda_z. \tag{3.9}$$

Dividing by the through-plane extension ratio, λ_z, yields true stress,

$$\frac{s_{x,y}}{\lambda_z} = \sigma_{x,y} = -\Pi. \tag{3.10}$$

Equation 3.10 tells us that the true in-plane stress, $\sigma_{x,y}$, is equal and opposite to the osmotic pressure. This true in-plane stress multiplied by film-thickness is what is measured in cantilever bending. By measuring the stress-thickness via the cantilever bending method, and thickness via ellipsometry, the osmotic pressure of a surface-attached polymer film can be measured. Furthermore, at swelling equilibrium, the osmotic pressure will be equal and opposite to the elastic pressure, which is the shear modulus of the surface attached film.

3.3.1 Polyacrylic Acid Hydrogels

To test the solid mechanics theory, a model system of a surface-attached hydrogel is measured using the cantilever bending method. Polyacrylic acid is ene-functionalized, then mixed with dithioerythritol, a crosslinking molecule. Polyacrylic acid and dithioerythritol are spin cast from solution onto a silicon substrate and the film is annealed under vacuum at 120°C overnight to activate the thiol-ene click reaction. The substrate can be thiol functionalized as well to crosslink the polymer covalently to the surface. Figure 3.2 shows the reactions for functionalization and crosslinking.
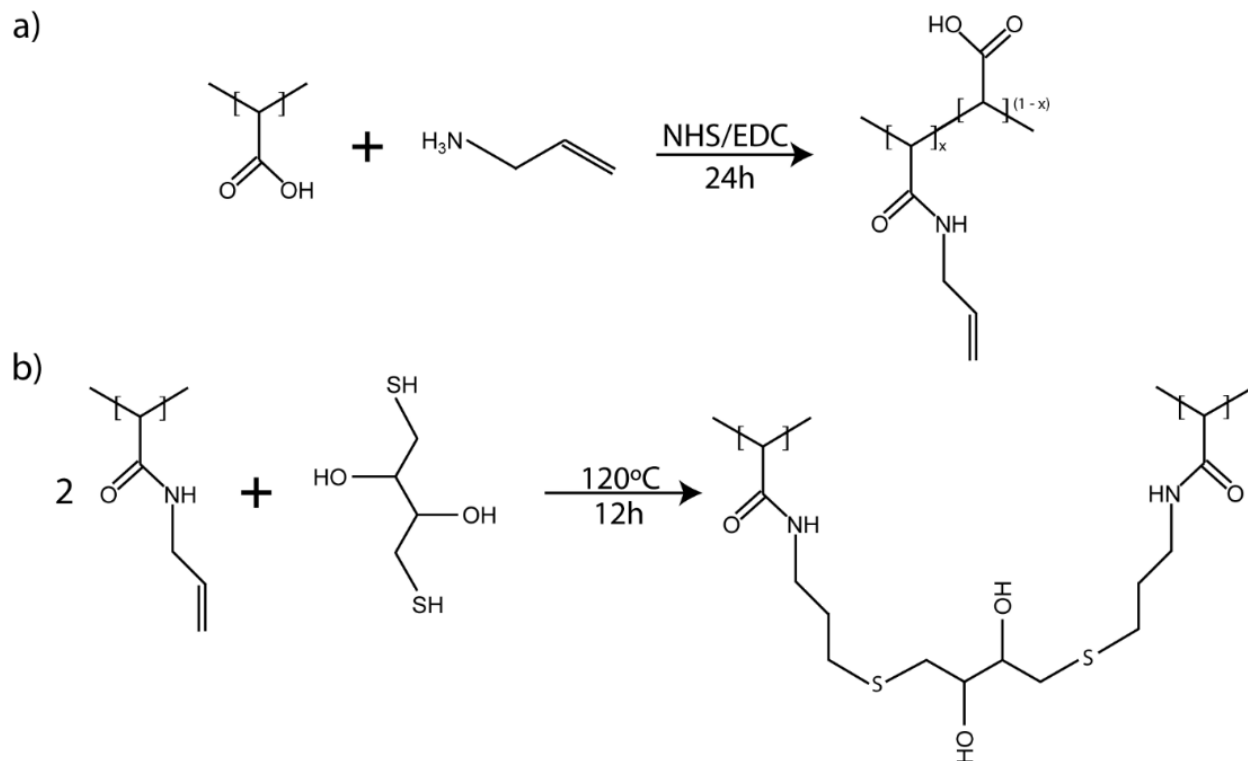
Figure 3.2. a) Polyacrylic acid ene-functionalization reaction b) Crosslinking reaction with ene-functionalized polyacrylic acid and dithioerythritol.

3.3.1.1 Polyacrylic Acid Functionalization

Polyacrylic acid functionalization follows the method by Li et. al.[67] Polyacrylic acid with a molecular weight of 250 kg/mol is used and the reactant amounts are such that 10% of the acrylic acid monomers are functionalized, assuming complete conversion. 15.429g of 35 wt% polyacrylic acid solution is diluted to 3.47 wt% with 137g H_2O and 7.49 mmol of EDC and 7.49 millimoles NHS are added to the vessel while stirring. The solution is adjusted to pH 4.5 with HCl and left stirring for 2 hours. 7.49 millimoles of allylamine is then added and the solution is adjusted to pH 10 with NaOH. After adjusting to the correct pH, the reaction mixture is left stirring, covered, for 24 hours to allow for complete reaction. The solution is then dialyzed; first in a 0.1 M NaCl solution to remove any trace reactants, followed by de-ionized (DI) water. The functionalized polymer is then freeze dried before re-dispersing in a water/THF solution for spin casting.

After functionalized PAA and dithioerythritol is spin cast and annealed to form the crosslinked polymer, it is soaked in DI water for 24 hours to remove any unreacted dithioerythritol. The sample is diced into a cantilever for the bending method, and a section to be run on the ellipsometer under the same conditions.

3.3.2 PAA Cantilever Bending Results

Plotting the fractional swelling and stress-thickness versus RH in Figure 3.3, there is a large hysteresis below ~70% RH. The point at which the hysteresis disappears for both film thickness and stress-thickness is the solvent-induced glass-rubber transition. Since the solid mechanics

analysis assumes molecular incompressibility, it will be invalid for the glassy state as further illustrated below.
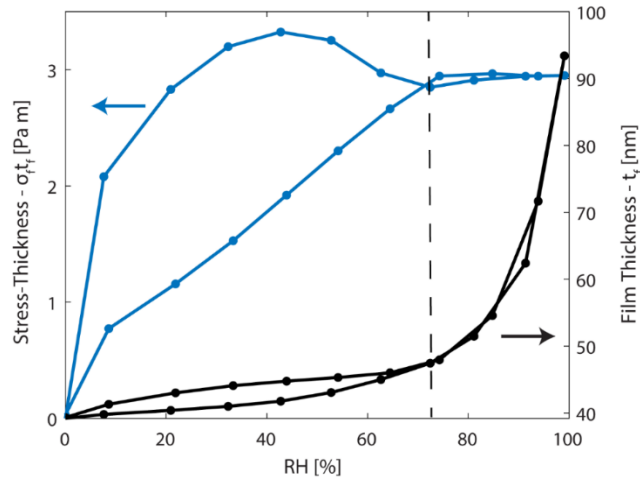
Figure 3.3. Stress-thickness and film thickness of a PAA hydrogel plotted versus relative humidity. The dashed line indicates the solvent-induced glass-rubber transition.
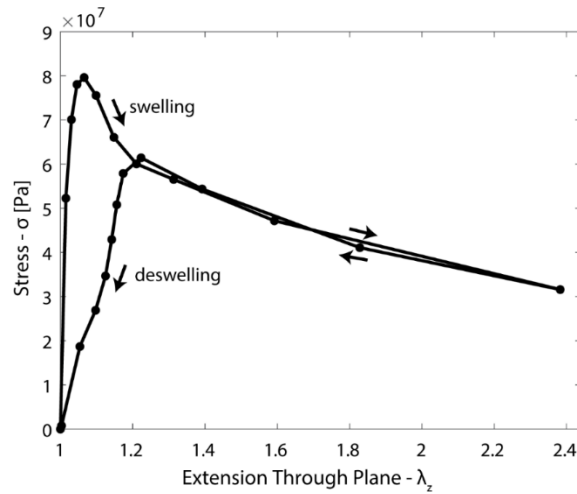
Figure 3.4. Stress-strain curve for the PAA hydrogel. The glass-rubber transition occurs at $\lambda_z \approx 1.2$.

Stress is plotted versus swelling strain in Figure 3.4 and is equivalent to the osmotic pressure in the rubbery state. Flory-Rehner theory also states that this osmotic pressure is equal to the equilibrium shear modulus at that water content. From scaling literature theory, Rubinstein *et. al.* have shown that the shear modulus for bulk polyelectrolyte gels in the no-salt limit scale inverse linearly with the volumetric swelling ratio.[68] For surface attached films, the through-plane extension is equivalent to the volumetric swelling ratio, Q. Plotting the stress/osmotic pressure versus Q on a log scale, we see that the stress has a slope of −1 in the rubbery state (Figure 3.5). This is the same scaling predicted by Rubinstein et. al, and indicates that the cantilever bending method directly measures the shear modulus of a swollen polymer network in the rubbery state.

38
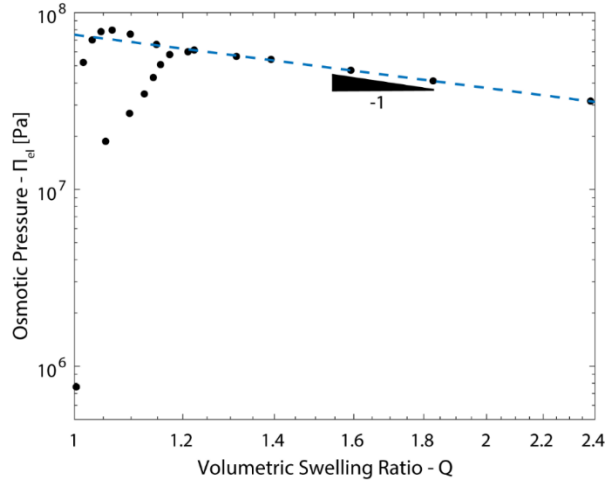
Figure 3.5. Osmotic pressure of the PAA hydrogel plotted versus the volumetric swelling ratio on a log-log scale. The −1 scaling agrees with theoretical predictions for polyelectrolytes in the no-salt limit.

We can use the measured osmotic pressure, Π_{el}, of the PAA hydrogel to calculate the ionic contribution using[69]

$$\Pi_{el} - \frac{RT}{v_m}(\phi_2 + \chi\phi_2^2 + \log[1 - \phi_2]) + \Pi_{ion} = -\frac{RT\ln[\alpha]}{v_m}, \qquad (3.11)$$

where ϕ_2 is the polymer volume fraction, χ is the Flory-Huggins interaction parameter, and v_m is the molar volume of water. At a given water activity, α, the elastic pressure is balanced by a Flory-Huggins mixing term, and a term for the additional driving force of ion solvation. From the cantilever bending and ellipsometry experiments, the only unknowns in the above equation are χ and ionic osmotic pressure, Π_{ion}. Using a value of 0.41 for χ,[70] ion osmotic pressure can be calculated as a function of polymer volume fraction, ϕ_2 (Figure 3.6).
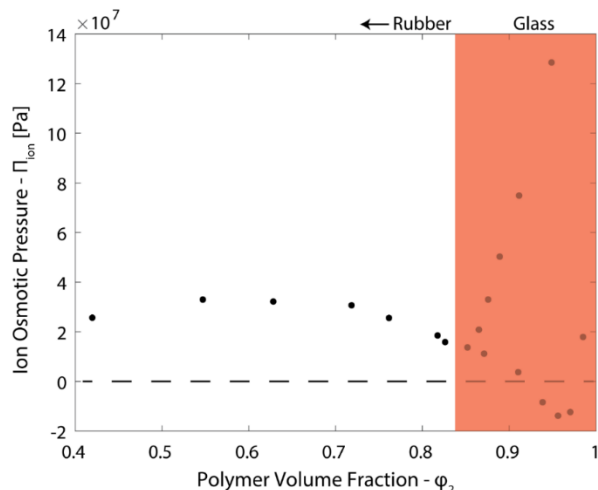
Figure 3.6. Ion osmotic pressure versus PAA polymer volume fraction. The ion contribution to the total osmotic pressure is calculated using Flory-Rehner theory, which gives aphysical results in the glassy state (shaded orange).

In the glassy state, Flory-Rehner theory predicts aphysical results for the ion concentration, which confirms that molecular incompressibility is an invalid assumption for glassy polymers. In the rubbery state, this equation predicts physical values and physical trends with polymer volume fraction. As more water is absorbed into the PAA hydrogel, decreasing the polymer volume fraction, more ion-pairs dissociate, and the ion osmotic pressure increases before leveling off. For the lowest polymer volume fraction measured, the ion osmotic pressure starts to decrease, indicating further water sorption into the PAA hydrogel begins to dilute the local ion concentration. If lower polymer volume fractions were accessible (through a lower crosslink-density sample or higher water activity), the osmotic pressure should display a linear dependence on polymer volume fraction in this region.[69] Nonetheless, this framework provides a way to calculate ion osmotic pressure that could be useful for studying polyelectrolyte thin films. While Flory-Rehner theory is not applicable for the glassy state, the measured stresses can inform a non-equilibrium thermodynamic model in a similar way to calculate different pressure contributions.

3.4 Calculating the Shear Modulus of PFSAs

The above Flory-Rehner and solid-mechanics analysis tells us that the measured stress is the osmotic pressure, and that, at a swelling equilibrium, the osmotic pressure is equal to the shear modulus of the polymer network. This analysis assumes that the polymer is in a rubbery state and thermodynamic equilibrium. PFSA ionomers are a complex material- they are phase-separated, semi-crystalline, and exhibit multiple thermal transitions. At room temperature, where the cantilever bending method is used, these materials are above their β-transition but below their α-transition.[71] Previous studies have assigned this β-transition to be the true glass transition temperature of the materials, while the α-transition is related to mobilization of the SO_3-group bonding network.[21, 72] Despite measuring the materials above their true glass transition temperature, there is still hysteresis in stress-strain curves for swelling and deswelling. This hysteresis indicates that these materials are not attaining a thermodynamic equilibrium, and we cannot apply the above theory. These materials obey the general Flory-Rehner hypothesis that a material will swell until the chemical and mechanical free energies are equal, but it appears that

we cannot directly measure the modulus of PFSA materials versus water content using the cantilever bending method. Instead, non-equilibrium thermodynamic models would need to be used, informed by the measured stresses, to calculate modulus versus water content.

While the true modulus cannot be directly measured, one can calculate an effective shear modulus, G_{eff}, by rearranging Equation 3.8,

$$Nk_bT = \frac{\sigma}{\left(\lambda_z - \frac{1}{\lambda_z}\right)} = G_{eff}. \tag{3.12}$$

This effective shear modulus is the modulus that a hypothetical affine network would possess to generate the stress at a given through-plane extension. As PFSAs uptake more water, the strength of the SO3-group interactions decrease, decreasing the effective number of crosslinks, N, present in the material. Comparing G_{eff} across processing conditions and counterion identity may prove useful for determining correlations in structure-property relationships.

To elucidate a more correct value for the shear modulus, a micromechanics approach could be utilized. Prior work by Kusoglu et. al used a representative volume element (RVE) model to estimate the modulus of PFSA materials by fitting water-uptake data in bulk membranes.[64] This approach could be applied to thin films but would need to be modified for non-uniform swelling that comes from being adhered to a substrate. Furthermore, anisotropy in the nanostructural morphology is observed via GIXS and would also need to be accounted for in the RVE model.

3.5 Generalizing the Cantilever Bending Method

The cantilever bending technique is based on strain misfit between the thin film and substrate. In the case of water sorption, the polymer wants to swell in plane, but cannot. This misfit in strain causes stress and changes the curvature of the cantilever. In principle, the stress of a thin film can be measured via the cantilever bending method due to any type of strain misfit. Two additional scenarios are explored here for polymer networks, the first being a misfit between thermal expansion coefficients to measure thermal transitions and the shear modulus, and the second is volume transitions due to temperature and pH.

3.5.1 Thermal Transitions and Temperature Dependent Shear Modulus

The thermal expansion coefficient (α) of silicon and polymers is likely to be different. For polymer thin films adhered to silicon, the difference in α will generate a strain mismatch versus temperature, and this will lead to a non-zero stress in the polymer film. The functional form of the thermally-induced misfit strain is

$$\varepsilon_{misfit} = (\alpha_{film} - \alpha_{substrate}) * (T - T_o). \tag{3.13}$$

This strain causes a stress and can be related back to the curvature of the cantilever. Rearranging Stoney's thin-film equation, the curvature of the substrate has the form

$$\Delta\kappa = -\varepsilon_{misfit}\frac{E_{film}(1 - \nu_{substrate})6t_{film}}{E_{substrate}(1 - \nu_{film})t_{substrate}^2}. \tag{3.14}$$

The curvature is a function of the strain misfit, and the modulus and thickness of both the film and substrate. Through a polymer's thermal transition, there will be a corresponding transition in the values for α_{film} and G_{film}, leading to a change in the curvature.

Using literature values for the material properties of Nafion and silicon, we can use Equation 3.14 to illustrate what the change in curvature might look like for a Nafion thin film heated through a thermal transition. The thermal expansion coefficient as a function of temperature is taken from cooling-rate ellipsometry experiments,[73] and bulk values for Nafion's modulus are used[74] since thin-film mechanical properties are not available as a function of temperature. Silicon is an extremely well characterized material, and empirical equations for the modulus and thermal expansion coefficient are both readily available in literature. Nafion thermal expansion and modulus data are shown in Figure 3.7 and fit to piecewise functions for further calculations.
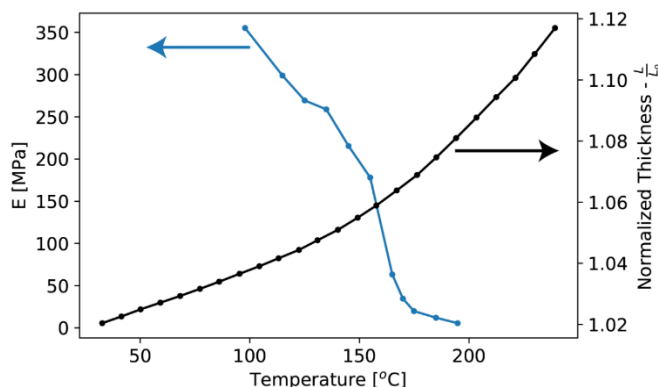
Figure 3.7. Young's modulus and normalized thickness plotted versus temperature. The data is fit to piecewise functions to calculate curvature.

With functional forms for Nafion and Silicon properties versus temperature, the curvature of a Nafion thin film on a silicon substrate can be calculated (Figure 3.8). A precipitous drop in the curvature is observed at ~160°C, which corresponds to the α-transition of Nafion. This distinct transition in the curvature is due mainly to the large drop in the modulus of Nafion. The mismatch in the thermal expansion coefficients is what generates the stress, but the relative change in the thermal expansion coefficient is small. As Nafion's modulus decreases sharply, the stress within the film also decreases; this decrease in stress is what is captured in the hypothetical cantilever experiment. Figure 3.8 is promising evidence for using the cantilever bending method to measure thermal transitions in polymer thin films. The transition is clearer in the curvature than it is in the cooling rate ellipsometry data and may potentially be more sensitive to thermal transitions.
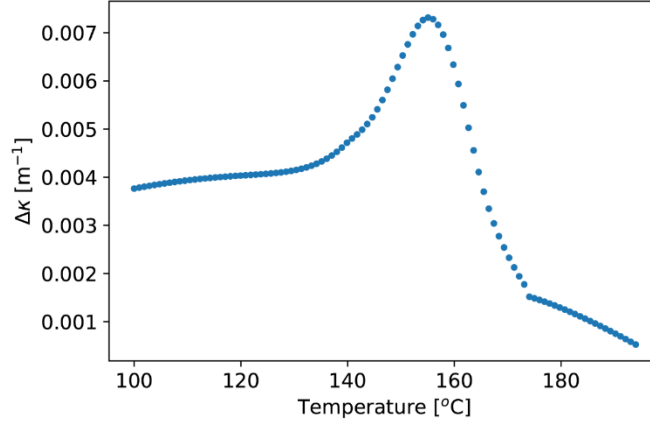
Figure 3.8. Curvature plotted versus temperature for a hypothetical Nafion thin film on a thin silicon cantilever. The sharp transition in the curvature is where Nafion goes through its α-transition.

Beyond identifying thermal transitions, the cantilever bending method can also be used in conjunction with ellipsometry to measure the shear modulus of polymer thin films using temperature as the perturbing stressor. By measuring film thickness and curvature of a polymer thin film versus temperature, Equation 3.14 can be used to calculate the modulus of the polymer film. Silicon's values for α, ν, and E are all known, and α_{film} can be calculated from the ellipsometry experiment. The two unknowns in Equation 3.14 are E_{film} and ν_{film}, but these can be combined to instead calculate the polymer film's shear modulus

$$2G = \frac{E}{1-\nu}. \tag{3.15}$$

Plugging Equation 3.15 into 3.14 and rearranging,

$$G_{film} = -\frac{E_{substrate}t_{substrate}^2 \Delta\kappa}{6(1-\nu_{substrate})t_{film}} \frac{1}{\varepsilon_{misfit}}. \tag{3.16}$$

Equation 3.16 provides a straightforward way to calculate a polymer thin-film's modulus as a function of temperature. Heating PFSA thin films at different water contents may also be an alternative strategy to measure the modulus as a function of water content and temperature. In the standard water-vapor-sorption experiments done via the cantilever bending method, the water absorption is the stressor perturbing the system, thereby making it difficult to extract the modulus at different water contents. Here, one can hold water content constant and vary temperature to perturb the system, measure the curvature, and calculate a shear modulus. Holding water content versus temperature, however, is non-trivial, and care must be taken to recreate the same experimental conditions for the cantilever and ellipsometry experiments. With temperature as an additional stressor, the cantilever bending method holds promise to characterize modulus as a function of temperature and water content and identify thermal transitions in polymer thin films.

3.5.2 Volume Transitions

While polymers in air heated through a thermal transition experience a large change in their modulus, polymers in water can experience drastic changes in volume. Hydrogels can experience volume transitions due to temperature and pH, and these characteristics are used to design responsive polymers for a variety of applications including marine coatings, sensors, drug delivery, catalysis, and enzyme immobilization. The cantilever bending method can also be used to study the stresses that are induced through volume transitions. An example of a temperature-induced volume transition material is poly(n-isopropylacrylamide) (PNIPAM). Hydrogels of this material, when heated in water, experience a drastic volume shrinkage around 30°C due to a lower critical solubility temperature (LCST).[75-77] Above this temperature, it becomes thermodynamically unfavorable to be solvated by water. Volume transitions in PNIPAM hydrogels are well studied in bulk, where the volume transition is a function of crosslinking density.[78-80] In these systems, the stresses can be estimated through Flory-Rehner theory but cannot be directly measured. By attaching PNIPAM hydrogels to surfaces as thin films, the stress can be directly measured and used to validate the thermodynamic theories often applied. Extracting energetics of the volume transition can be used to design temperature-responsive materials. This same analysis can be applied to pH-responsive polymers, and by combining temperature- and pH-sensitive moieties together through polymer chemistry, one can design next-generation multi-responsive films and coatings.

3.6 Summary and Outlook

The chemical-mechanical energy balance that dictates water content in PFSA membranes and thin films is an important one. While it has been well characterized for bulk membranes, this relationship is less defined for thin films due to the difficulty in measuring their mechanical properties. This chapter reviewed the techniques used for characterizing the mechanical properties of PFSA thin films, before applying Flory-Rehner theory and solid mechanics analysis to understand better the stresses measured in the cantilever bending method. For rubbery polymers and cross-linked polymers in the rubbery state, the stress measured is the osmotic pressure and the equilibrium shear modulus. Unfortunately for PFSA materials, which exist in a non-equilibrium state, such a straightforward relationship does not exist. An effective modulus with water content can be used for correlations, but further development of non-equilibrium thermodynamic models is needed to calculate the shear (and Young's) modulus with water content.

4 Patterned Substrates for *Operando* Studies and Thin-Film Conductivity

4.1 Introduction

In the catalyst layer of many electrochemical energy-conversion devices, PFSA ionomer is in the presence of metallic catalyst particles supported on carbon nanoparticles. In these devices, there are also applied potentials to drive the electrochemical reactions. The heterogeneous environment and electrochemical potentials may affect the structure and behavior of PFSA ionomers. Thus, it is desired to study PFSA ionomer thin films on metal substrates *operando*. To achieve this, fabrication of heterogeneous substrates and planar electrode cells are necessary that can mimic the local catalytic environment. In this chapter, I cover the basic fabrication methods used to create patterned substrates and discuss two *operando* x-ray studies looking at Nafion and 3M perfluorinated anion exchange material (PFAEM) thin films. Also discussed is the design of interdigitated electrodes for thin-film conductivity measurements.

4.2 Micro/Nanofabrication Procedure
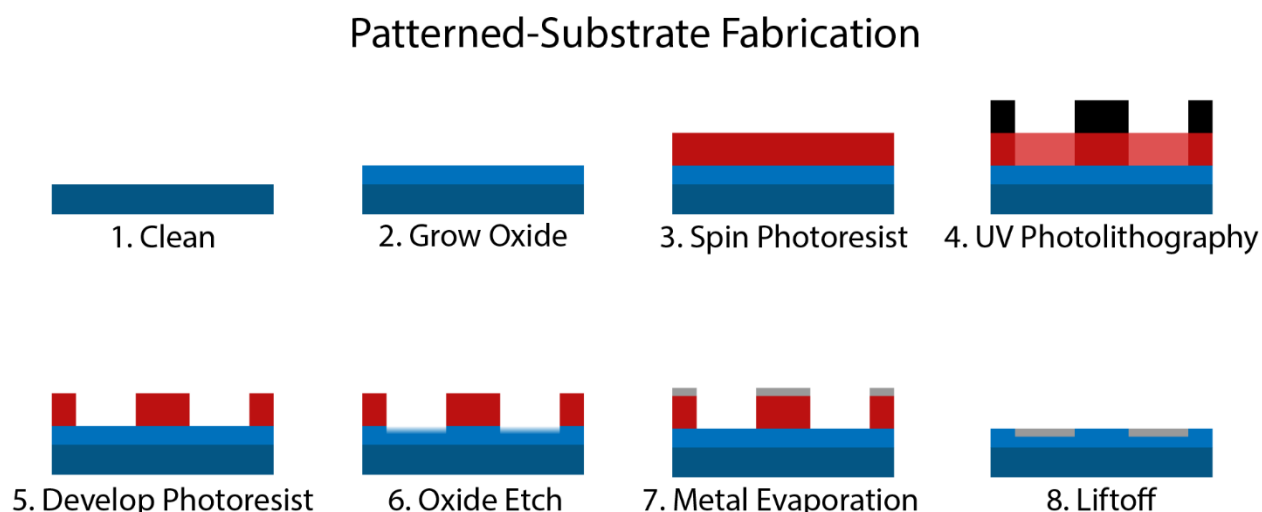
Figure 4.1. Schematic of patterned substrate fabrication using standard micro/nanofabrication techniques. Dimensions are not to scale and are only meant to illustrate the processes.

Relative to the fabrication of many semiconductor devices, the process of creating patterned substrates for studying PFSA thin films is straightforward. Figure 4.1 shows a schematic of fabricating the patterned substrates. Silicon wafers are cleaned in successive baths of boiling piranha and hydrofluoric acid solutions to remove trace organic material and the native oxide layer, respectively. The cleaned wafers are then put into an oven to thermally grow a silicon dioxide layer; oxygen and water vapor are fed in at 1000°C to grow a uniform oxide layer. This process has been well studied, and the time required to reach a certain thickness can be calculated using the Deal-Grove model.[81] After thermal oxide growth, photoresist is spin coated onto the wafer for patterning. For patterning larger feature sizes (> 2 µm), contact UV photolithography is used. Feature sizes can be reduced further using projection UV lithography (~0.6-2 µm), and for nanometer-scale features electron-beam lithography is required; the lithography method used will

45

dictate the type of photoresist. UV photolithography and a positive i-line photoresist are used here, as our feature sizes are all greater than 2 μm. Patterns are designed using L-edit software and etched into a chrome mask. The chrome mask blocks UV light and only exposes certain areas of the wafer. UV light causes chain scission of the positive photoresist and areas exposed to UV light will be soluble to the developing solution.

After the photoresist is exposed and developed, the patterned wafer is plasma etched. A mixture of CF_4, CF_3H, and Argon are fed into a vacuum chamber under a high AC potential, which creates a plasma that selectively etches the exposed silicon dioxide areas. The plasma etch is anisotropic, which creates vertical trenches in the silicon dioxide. These trenches are filled back in with metal to create planar patterned substrates. Metal can be deposited via thermal/electron-beam evaporation or sputtering. Measuring the thickness of the silicon dioxide layer before and after etching with ellipsometry allows us to calculate the trench depth, and precisely fill it with metal such that the resulting pattern is planar. The final step is to liftoff the metal-coated photoresist, which is done using heated N-Methyl-2-pyrrolidone (NMP). From here, the wafers can be diced into individual substrates for polymer thin-film studies.

4.3   Planar Electrodes for *Operando* X-Ray Studies

Using the fabrication procedures described in Section 4.1, I designed and fabricated a planar 3-electrode device (Figure 4.2) to use at Beamline 7.3.3 of the ALS. A working, counter, and reference electrode made of platinum are embedded within silicon dioxide to create the planar electrode device. In designing the device, considerations were made for the x-ray beam size at 7.3.3, which measures ~700 μm wide by ~300 μm tall. To probe the ionomer structure spatially at each electrode and in the gap between them, each of these areas must be larger than the relevant beam dimension. The gap between electrodes is 1 mm. This distance creates large resistances for ion conduction but is necessary so that the structure of the ionomer in this gap can be probed without contributions from structure on the electrodes. Ideally, with a smaller beam size this gap could be reduced to minimize ohmic resistance. The second design consideration is the electrode length. In the grazing-incidence geometry, the x-ray beam footprint is ~1.5 cm; thus, the electrode length is 1.7 cm to ensure the entire beam is on the electrode. With this device, we have been able to study the structure of Nafion and PFAEM thin films under applied potentials in humidified N_2 and H_2/N_2 environments.
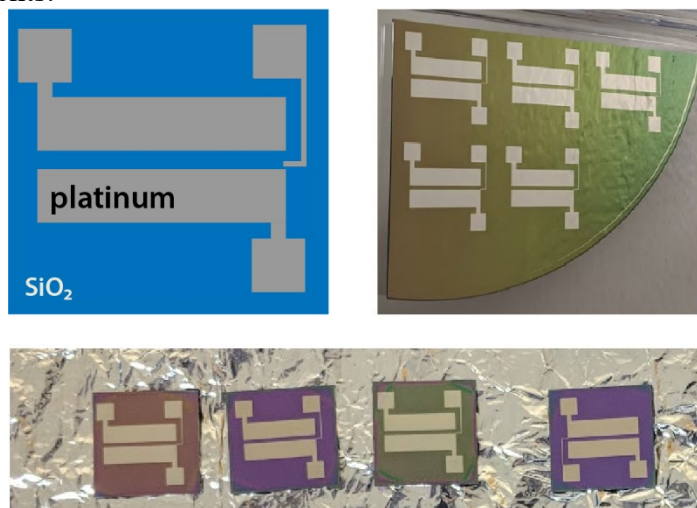
Figure 4.2. Schematic and pictures of planar electrode design for *operando* GIXS.

4.3.1 Nafion Thin Films

A 185 nm Nafion thin film was spun cast onto the planar 3-electrode device for structural characterization using GIXS. At each operating condition, the structure of Nafion was probed spatially across the working electrode, electrode gap, and counter electrode. From each image, the ionomer peak was fit to extract peak intensity, position, and FWHM. Because the device is planar and the Nafion film thickness is uniform across the device, we can probe the effect of substrate and applied potential upon the ionomer structure.
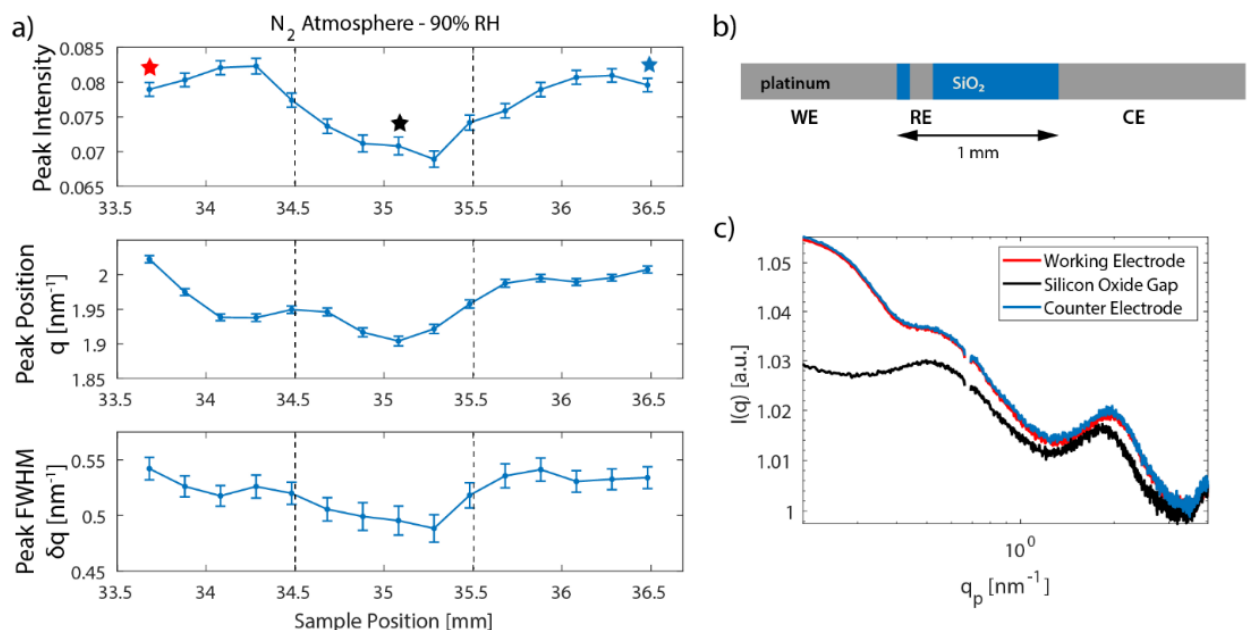
Figure 4.3. a) Spatially resolved parameters extracted from ionomer peak fitting. Dotted line shows the 1mm SiO_2 gap b) Schematic of scan area c) Horizontal line-cuts taken at each electrode and the SiO_2 gap.

At 0 V in an N_2 atmosphere, the Nafion thin film is subject to the same conditions used for swelling and conductivity measurements and serves as a baseline from which to compare experiments under H_2/N_2 and applied potentials. Figure 4.3a plots the extracted ionomer peak parameters across the device alongside a cross-sectional view of the device (Figure 4.3b). The ionomer peak in the SiO_2 gap has a slightly lower q-spacing (higher d-spacing) and lower FWHM compared to either electrode. This indicates the ionomer has a slightly higher water content between the electrodes, but it is a subtle effect. Additionally, the ionomer peak intensity is higher at each electrode compared to SiO_2, but this is likely due to EFI and background effects. As such, it is only useful to determine where the respective electrodes are. Horizontal linecuts are taken at each electrode and the SiO_2 gap (positions denoted with stars in Figure 4.3a), and plotted in Figure 4.3c. The main difference in the linecuts is the absence of the platinum paracrystalline peak at ~0.1 nm^{-1} for the SiO_2 linecut. This platinum paracrystalline peak is from the surface morphology of the evaporated platinum. While platinum may affect the local hydration of the ionomer, it does not appear to change the observed morphology. This is also reflected in the orientation parameter of the ionomer peak, which is 0.485 to 0.486 (isotropic) at all three positions.
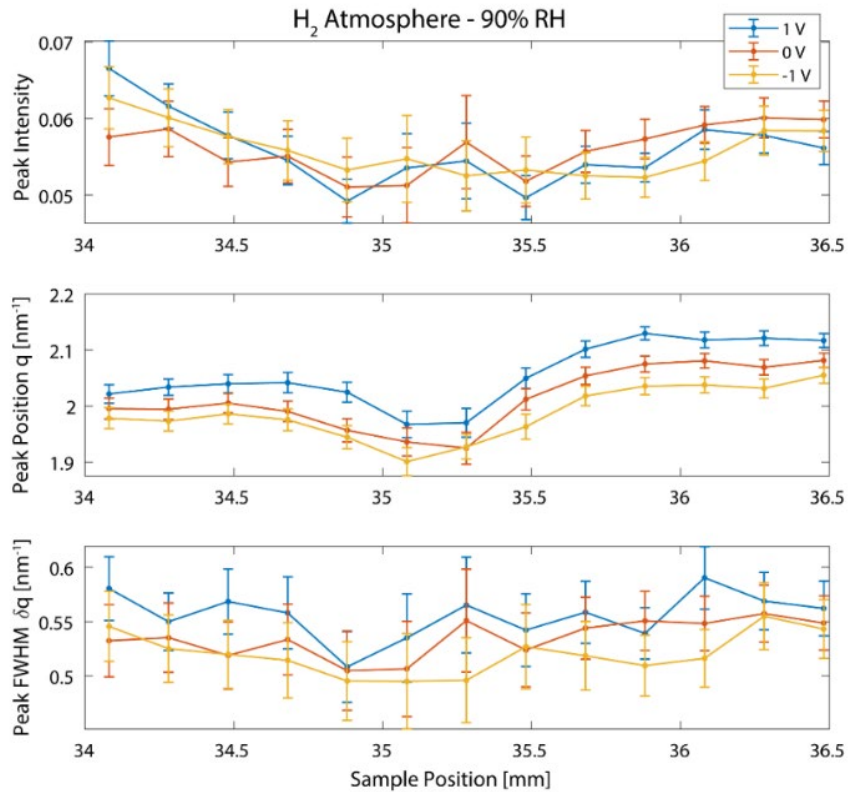
Figure 4.4. Spatially resolved extracted parameters for three different operating conditions under hydrogen atmosphere.

Moving to an H_2/N_2 atmosphere, the same spatial scanning and peak fitting is performed at 1, 0, and −1 V. The extracted ionomer peak parameters for each of these conditions is plotted in Figure 4.4. There are no observable trends in the ionomer peak intensity with applied voltage. While the ionomer peak intensity and FWHM appear to decrease with decreasing applied voltage, this is due to a slow increase in the relative humidity (RH) over the course of the successive scans rather than a change associated with applied voltage.
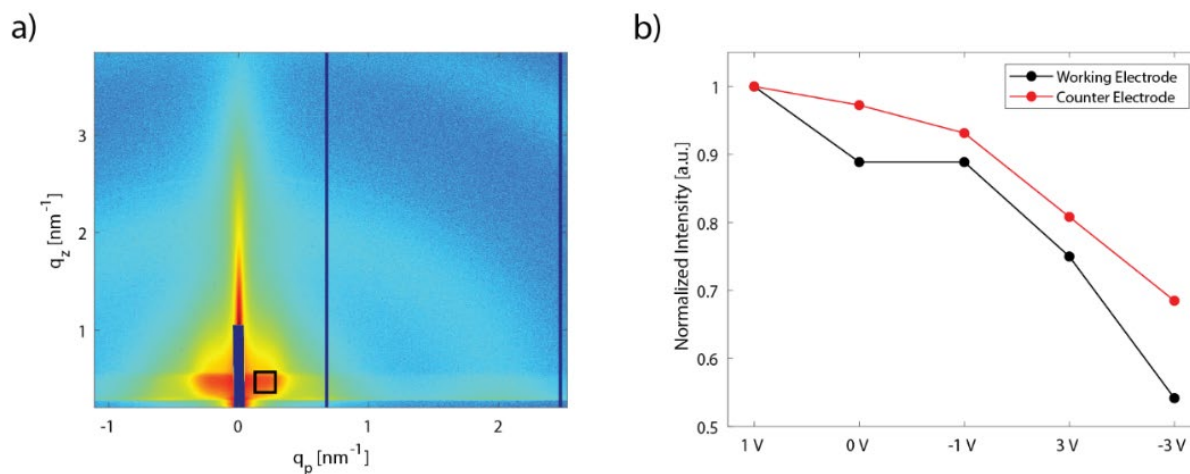
Figure 4.5. a) 2D GISAXS image of Nafion on a platinum planar electrode. The black box denotes where the paracrystalline peak intensity was sampled. b) Normalized intensity of paracrystalline peak versus voltage under N_2/H_2 atmosphere.

Despite no observable change in the ionomer peak, there is a change in the platinum paracrystalline peak intensity. Figure 4.5a shows where this peak occurs in the 2D scattering image and the voltage dependence of its intensity. The platinum paracrystalline peak intensity decreases at both the working and counter electrodes with successive sets of applied voltages. Because there is only a decrease in intensity and no change to the peak shape, this suggests that the ionomer film is densifying such that contrast between platinum and film is decreased. Comparing 1, 0, and −1 V, there appears to be a slightly larger decrease at the electrode performing hydrogen reduction. At 3 and −3 V, however, intensity at both electrodes decreases commensurately. At this high potential, water splitting is also occurring, which may affect the structure of Nafion more dramatically. To investigate the hydrogen-pump conditions further, scattering images of the working electrode were taken across a range of incidence angles to generate incidence angle resolved (IAR) plots.
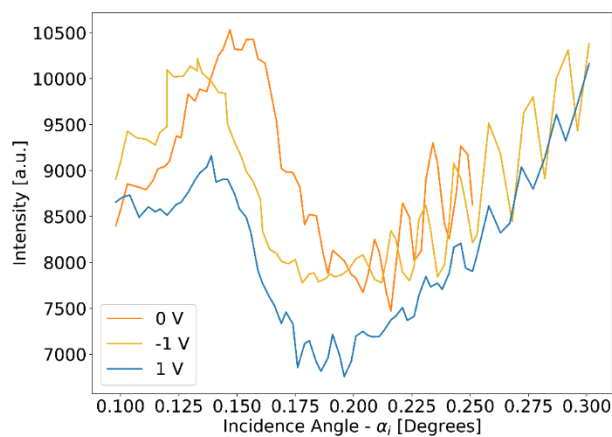
Figure 4.6. Incidence angle resolved plots of specular rod intensity for three applied voltage conditions under a humidified N_2/H_2 atmosphere.

Figure 4.6 shows the IAR plots at the working electrode for 0, −1, and 1 V. Comparing 0 and −1 V, the critical angle of the ionomer film decreases at −1 V, indicating a decrease in the film density. This is counterintuitive to the results shown in Figure 4.5b, which would support an increase in the density of the ionomer film. For both observations to occur, there would need to be a distribution in density of the ionomer film as a function of depth. A denser layer may form near the electrode surface, with a less dense layer above it. The shift in transverse electric (TE) modes at $\alpha_i > 0.2°$ also supports a change in density. Going from −1 V to 1 V, the critical angle slightly increases and the amplitude of the TE modes decrease. This decrease in TE amplitude suggests a smaller contrast between platinum and the adjacent Nafion layer compared to 0 and −1 V. From these IAR plots, there is a clear effect of voltage on the through-plane density of the Nafion thin film, but EFI modeling will need to be done to determine exactly where the density shifts are occurring and to what degree the Nafion densifies. Prior work on hydrated Nafion thin films on silicon using neutron reflectivity has demonstrated lamellar ordering near the substrate interface,[13-14, 82] so we are likely capturing this structure in the IAR data. To what degree a platinum interface and applied voltage affects this lamellar ordering is unknown. Future IAR experiments probing the structure on silicon versus platinum at different applied voltages will be done to answer these questions.

4.3.2 PFAEM Thin Films

The planar 3-electrode device with a Nafion thin film operates as a hydrogen pump under applied voltage in an H_2/N_2 atmosphere. Hydrogen gas is reduced at the anode and protons are transported to the cathode where they are oxidized back to hydrogen gas. Nafion's sulfonic-acid moieties natively have protons associated with them and during hydrogen-pump operation this does not change. For ion-exchanged PFSAs or other ionomer chemistries where the counterion identity changes during reaction, or the flux of reactants from one electrode to another changes the concentration profile, there may be an associated change in structure. An example of this is perfluorinated anion exchange material (PFAEM), which reacts with CO_2 in the air to form bicarbonate and carbonate as the counter ion to the charged groups on the backbone. A prior study demonstrated a change in structure that accompanied this reaction with CO_2.[83] We hypothesized a change in structure would also occur when electrochemically converting the carbonate species back into CO_2 and OH^-. A PFAEM thin film was spun cast and annealed at 150°C for 1 hour under vacuum. After annealing, the sample was placed in a humidified H_2/N_2 environment and 2 V was applied to drive the water splitting reaction. Scattering images were taken every 1 minute for the first 10 minutes, followed by every 5 minutes till 80 minutes of total time had elapsed.
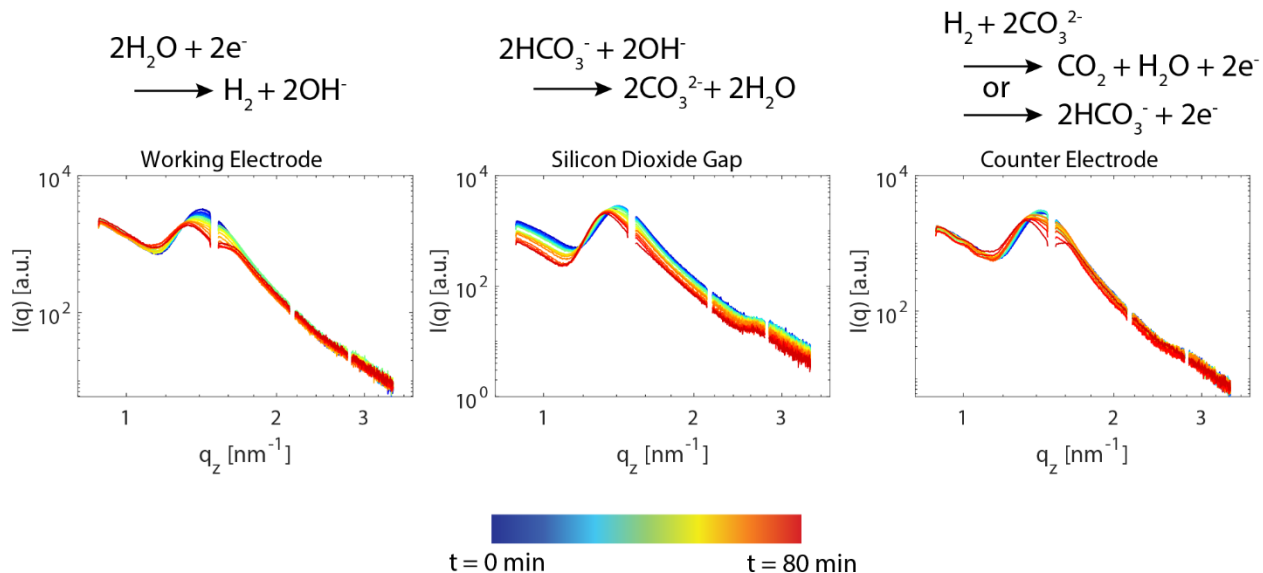
Figure 4.7. Time-resolved vertical linecuts at the working electrode, silicon dioxide gap, and counter electrode under a humidified N_2/H_2 environment with the associated reactions. Line color denotes the time.

Figure 4.7 shows the time-resolved vertical linecuts for the PFAEM thin film at both electrodes and the silicon dioxide gap and the associated chemical and electrochemical reactions. The structure starts off lamellar at all three positions with a first order peak at ~1.4 nm^{-1} and a weak second order peak at ~2.8 nm^{-1}. Over the course of 80 minutes, the first order peak splits into two peaks at ~1.3 and ~1.6 nm^{-1} at both electrodes. This $\sqrt{6}, \sqrt{8}$ peak spacing is observed in gyroid morphologies. At the working electrode, water splitting is taking place and generating hydrogen and hydroxide anions. At the counter electrode, carbonate is electrochemically reduced either to CO_2 or bicarbonate. As the local carbonate concentration decreases, the PFAEM transitions to a bi-continuous morphology. The second order lamellar peak disappears completely at the working electrode and has mostly disappeared by 80 minutes at the counter electrode. This change in morphology may be due to the change in anion charge from -2 to -1. In the silicon dioxide gap, the lamellar ordering is preserved, but the peaks move to lower q-spacing as the water content in the PFAEM thin film increases. At 80 minutes, the first order peak appears to begin splitting into two peaks. The different degrees in which ordering has changed reflects the non-monotonic distribution of carbonate, bicarbonate, and hydroxide in the film from electrode to electrode. A previous modeling study showed that at low currents, carbonate concentrations will be highest in the middle of the membrane between electrodes.[84] In the case of our planar electrode device, this is in the silicon dioxide gap. The experiment was stopped at 80 minutes due to time constraints, but if run further, the film may have reached a steady-state structure across the device once anion species concentrations reach a steady-state distribution.

The structural study looking at bicarbonate formation from CO_2 took place over the course of 140 minutes. Driving the reverse reaction electrochemically is also a slow process,[85] and the large ohmic resistance from the 1 mm electrode spacing resulted in a small current from the applied 2 V. Shrinking this gap to reduce resistance could speed up this reaction and using a smaller beamsize would allow one to still spatially resolve the structural change in *operando*. Other beamlines have smaller beamsizes to make this possible. While the large electrode gap has downsides, the planar 3-electrode device as a general platform is a promising tool to investigate

the structural changes that accompany applied potentials and is a step towards understanding how ionomer materials behave *in operando*.

4.4 Towards Connecting Structure and Water Content to Ion Conductivity

The 3-electrode planar device is useful for structural characterization during chronoamperometry experiments. However, the 1 mm electrode spacing creates a large resistance and it is unclear how far onto the platinum electrodes electrochemical reactions occur. These two factors make it difficult to characterize and model the system electrochemically. Illustrating this is Figure 4.1 which shows a cyclic voltammogram (CV) of the Nafion thin film from section 4.2.1. Small redox peaks appear at approximately ±1.23 V, but the large film resistance dominates the CV data. The large resistance would have a similar effect in electrochemical impedance spectroscopy (EIS) and measuring different transport phenomena would be difficult. It is desired to connect structure and swelling measurements to detailed electrochemical measurements, which necessitates a different cell design.
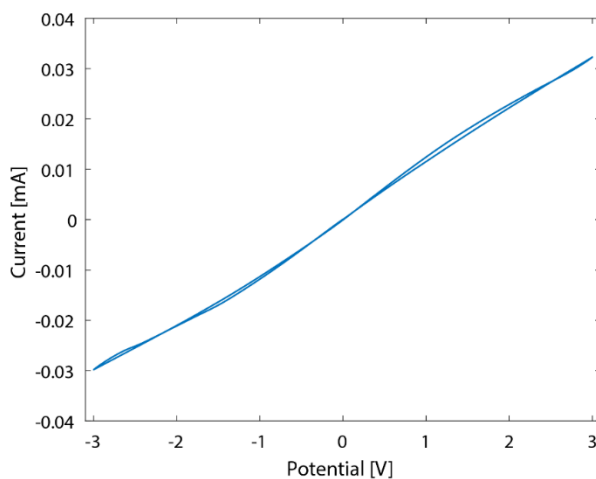
Figure 4.8. Cyclic Voltammogram of a Nafion thin film on the planar electrode device under humidified H_2/N_2. Sweep rate is 20 mV/s.

The interdigitation of electrodes is a strategy that has been used to enhance sensitivity for electrochemical measurements. Interdigitated electrodes (IDEs) have applications in small solution-volume electrochemistry[86], chemical-[87] and bio-sensing[88-89] and have also been used to determine the capacitive properties of polymer thin films.[90] Within PFSAs, the conductivity of thin films was investigated with IDEs, though the devices used were not planar.[12, 91] More recent work from Sharon et. al[92] demonstrated IDEs as a robust measurement platform for interrogating the electrochemical properties of polymer thin films. In this paper, they designed planar IDEs and investigated LiTFSI-doped PEO thin films using EIS. The effect of electrode dimension, spacing, and film thickness were all demonstrated, and compared to equivalent circuit models for bulk and interfacial ionic transport. Their results lay out a framework for investigating ionic transport in polymer thin films, which we follow in designing our IDEs.
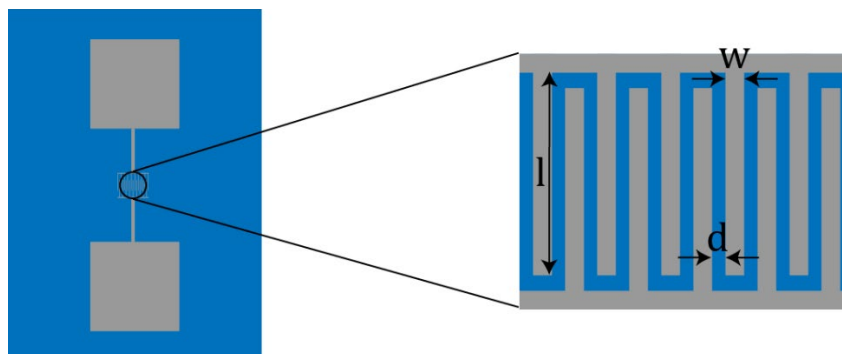
Figure 4.9. Schematic of IDE device for thin film conductivity.

Figure 4.9 shows a schematic of the general IDE device designed and fabricated with platinum as the electrode material using the procedures outlined in Section 4.1. The relevant dimensions of the IDE array are the width, length, and spacing of each electrode digit or tooth, as well as the number of teeth in the array. Two sets of arrays were manufactured, and their dimensions are listed in Table 4.1. The teeth spacing for both arrays is 4 μm to minimize the film resistance as prior studies have shown a large decrease in conductivity for nanometer-thick films.[12, 91] Array 1 has a tooth width of 4 μm and Array 2 has a tooth width of 12 μm. The larger width for Array 2 will be more sensitive to interfacial phenomena that may occur under applied potentials; by modeling and fitting the impedance spectra from both arrays, additional information on the effect of platinum interactions may be elucidated.

Table 4.1- Interdigitated electrode array dimensions

Array	Teeth length – l [μm]	Teeth width – w [μm]	Teeth spacing – d [μm]	Teeth number - N
1	898	4	4	150
2	898	12	4	150

Using platinum as the electrode material also enables additional experimental conditions. Prior studies used inert gold electrodes which restricts the measurement of film resistance to 0 VDC. With platinum electrodes, EIS can be performed at applied DC potentials to probe transport phenomena and faradaic processes at the electrode interface. Nafion on planar electrodes shows a change in through-plane density with applied potential, and local adsorption or densification could change the measured capacitance; such processes may be elucidated through fitting impedance spectroscopy with proper models.

A rigorous description of planar IDEs has been done using elliptic electric field lines.[92-93] While the full expressions are complex, they can be simplified because the film thickness is much smaller than the electrode spacing, and the long teeth length and large number of teeth minimize electric field fringing at the edges of the array. Using conformal mapping, the planar IDE can be transformed into an equivalent array of parallel-plate electrodes which follows the expression

$$\kappa = \frac{1}{R}\frac{d}{l(N-1)h},\tag{4.1}$$

where κ is the film conductivity, R is the film resistance, h is the film thickness, and $l, d,$ and N are the teeth length, spacing, and number, respectively. With the resistance measured via EIS, the conductivity can be calculated using Equation 4.1. Conductivity measurements can be combined with data from swelling experiments to understand how tortuosity is affected in PFSA thin films and this can be correlated to structural information from GIXS. GIXS can probe how domains are oriented and how strong the correlations between domains are, but it does not provide direct information on hydrophilic domain connectivity.

A phenomenological expression for conductivity in PFSA bulk membranes is

$$\kappa(\phi) = \kappa_o (\phi - \phi_o)^n, \tag{4.2}$$

where κ_o is a material parameter, ϕ is the water volume fraction, ϕ_o is the volume fraction at percolation of hydrophilic domains, and n is a scaling exponent that accounts for hydrophilic domain connectivity. In bulk PFSA membranes, n is close to 1.5, which is the expected value for an isotropic system with random domain connectivity.[3] As PFSAs are confined to nanometer-thicknesses, this scaling exponent will change as the hydrophilic domains orient. The water volume fraction can be calculated from ellipsometry swelling experiments under the same conditions, and Equation 4.2 can be fit to extract the different material parameters.

Another expression for conductivity can be derived from mesoscale transport[94-95]

$$\frac{\kappa}{F^2} = u_{H^+} c_{H^+} \frac{\phi}{\tau(\phi)}, \tag{4.3}$$

where F is Faraday's constant, u_{H^+} is proton mobility, c_{H^+} is proton concentration in the hydrophilic domain, and τ is the tortuosity. Hydrophilic domain proton concentration can be approximated as

$$c_{H^+} = \frac{1}{\lambda \, V_w} \tag{4.4}$$

where λ is the number of water molecules per sulfonic-acid moiety and V_w is the molar volume of water. The proton mobility, u_{H^+}, is expected to be constant across equivalent weights (EWs) of the same side-chain chemistry at the same water volume fraction and could be fit across data sets from different EWs. Equation 4.3 provides an additional way understand the connectivity of hydrophilic domains in ionomer thin films and yields more physical parameters than Equation 4.2, but there is a large body of literature using Equation 4.2; comparing the extracted values for thin films to bulk literature may provide additional insight into how PFSA structure and connectivity changes under confinement.

4.5 Summary

Using standard nanofabrication techniques, I designed and fabricated a 3-electrode planar cell for *operando* GISXS studies of ionomer thin films. Nafion thin films on this device are shown to have very similar structure on platinum versus silicon dioxide at 0 V, with only small differences in hydration inferred. Under applied potential, there is no observable change in the ionomer peak which is related to the distribution of hydrophilic domains in the material. Incidence angle resolved (IAR) data does show there is a change in density of the ionomer through plane and future IAR

experiments are planned to investigate this phenomenon further. The planar electrode device was also used to drive the electrochemical conversion of carbonate species into CO_2 and OH^- in a PFAEM thin film. This conversion was monitored using GIXS. As the carbonate species are converted, the PFAEM thin film went from a lamellar morphology to a bi-continuous one. From the Nafion and PFAEM experiments, design improvements to the planar electrode device for future experiments are discussed. The last section of this chapter discusses the design and fabrication of interdigitated electrodes for studying ion transport in ionomer thin films. Based on previous work, two different IDEs were fabricated and will be used by others to investigate ionic transport and faradaic processes.

5 Evolution of Ionomer Morphology from Dispersion to Film[*]

5.1 Introduction

There has been a growing interest in understanding ionomers as thin-films (< 100 nm thickness), which stems from the need to understand their behavior in the catalyst layers (CLs) of a fuel cell or electrolyzer.[1, 3, 96-98] In CLs, ionomer thin-films act as a binder and conducting media, transporting reactants and products to and from the catalytic sites (e.g., platinum) supported on carbon.[1, 5] CLs are cast from inks, where ionomer and catalyst-coated carbon particles are dispersed in a mixture of solvents, typically water/alcohol mixtures. To date, these inks and CLs have been empirically formulated, relying only on the end performance for guidance.[1, 5, 97-98] In an effort to understand the underlying science governing CL formation and, in turn, performance, more recent studies focused on ionomer/solvent interactions, ink formulations, and structure.[97-104] Furthermore, the dynamic processes that occur when inks are cast is an essential step in CL formation. In particular, it is important to know how the more volatile solvents preferentially evaporate first and affect ionomer structure and aggregation behavior in the drying ink. Then, to what extent do the structures in the colloidal state persist in the cast film and impact ionomer properties and performance? To begin to answer these questions, we start with a model system of PFSA ionomer in solution. Understanding gained from this model system can be applied to more complex ink systems and other ionomer-solvent compositions and inform the relative impact of components and their binary interactions on CL formation. Herein, we report the morphological changes during film formation of Nafion PFSA ionomer *in-situ* using grazing incidence x-ray scattering (GIXS).

A number of studies have utilized *in-situ* GIXS to understand the formation of organic electronics. Films are prepared using either a slot-die printer,[105-107] spin coater,[108-109] or spray-coater[110] and morphological data is collected as solvent evaporates and the film dries. These studies have shown that solvent, temperature, and organic composition affect both the transient and final morphologies, the latter of which can be correlated to device performance.[111] Ionomers present a distinctly different system to study, where protons (or ions) are the conducting species and conduction occurs through the water-filled domains of the phase-separated nano-morphology.[3] A slot-die printer is used to cast 5 wt% Nafion ionomer solution onto a diced silicon wafer, and morphology of the solution/film is collected via GIXS as a function of time (Figure 1a). Films were cast and imaged *in-situ* at small and large sample-to-detector distances to monitor the morphology evolution at multiple lengthscales.

5.2 Experimental Methods

Ionomer solutions. Nafion®-ionomer dispersion (5-wt% solids of 1100 g polymer $(molSO_3^-)^{-1}$ in alcohol-water mixture) were obtained from Sigma Aldrich. (St. Louis, MO) and used as purchased. For the solvent ratio dispersions, Nafion D2021 (20-wt% solids of 1100 g polymer $(molSO_3^-)^{-1}$ in alcohol-water mixture) was diluted in varying water/nPA ratios to 4-wt% solids. Nafion D2021 was purchased from Ion-Power Inc. (New Castle, DE).

Thin-film Casting. PFSA thin-films were cast in-situ using a custom-built mini slot-die printer.[105] After priming the line with solution, the films were cast from the slot-die head onto a silicon wafer

---

with a head-substrate gap height of 50 um and an injection rate of 5 uL/s. The print head was stationary while the substrate was translated underneath at a rate of 5 mm/s.

Grazing-incidence X-ray Scattering (GISAXS/GIWAXS). GISAXS/GIWAXS measurements were performed at beamline 7.3.3 of the ALS at LBNL.[112] The X-ray energy was 10 keV (λ=1.24 A^{-1}) with a monochromator energy resolution E/dE of 100, and the patterns were acquired with a Dectris Pilatus 1M or 2M CCD area detector (172 μm x 172 μm pixel size). GISAXS images were collected at grazing incidence angles (α_i) of 0.18° with 2 sec exposure. GIWAXS images were collected under He at α_i = 0.16° with a 3 second exposure time and corrected to account for the missing wedge of the Ewald sphere. Through-plane intensity vs. scattering wave vector I(q) profiles were obtained from 1° sector cuts and in-plane I(q) profiles were obtained using horizontal line-cuts ($\Delta q = 0.278\ nm^{-1}$). The core-shell cylinder form factor was fit in the SANS Toolbox within Igor Pro[113] and the Tuebner-Strey and double Gaussian models were fit using scripts written in Matlab. Error bars on the extracted parameters represent a 95% confidence interval. Exposure times and total dose were selected to mitigate x-ray induced damage to the sample. Included in the supplementary information is a more detailed discussion on Distorted Wave Born Approximation effects, fitting, and the models used in this work.

5.3   Results and Discussion

Immediately after casting, the "film" is still in a solution state and from prior studies, a rod-like aggregate of polymer chains is expected.[114-116] Figure 5.1b shows merged horizontal line-cuts from both GISAXS and GIWAXS for the early-time morphology. To accurately reproduce the shoulder at ~0.3 Å^{-1} and peak at ~0.6 Å^{-1}, a core-shell cylinder model is chosen. The extracted parameters indicate a dense core of PTFE backbone with a radius of ~0.8 nm, and a much less dense shell layer with a thickness of ~1.8 nm (Figure 5.1c). The shell is composed of side-chain, solvated ionic moieties and solvent, and represents an average electron density of these components. This cross-sectional representative volume has previously been employed for SAXS, and is now confirmed in this study with the higher-q data obtained from GIWAXS. While the core-shell cylinder can also be fit to the low-q region, the initial solution is 5 wt% and therefore a structure factor is expected due to interparticle interactions.

(a) Schematics of *in-situ* GIXS technique for monitoring ionomer film morphology during casting

ionomer dispersion
ionomer solid in
water:alcohol
solution

slot-die printer head
moving along the substrate

images are collected *in-situ*
structural evolution from
time-resolved GISAXS = f(time)

Detector
GISAXS

q_z

X

substrate

x-ray
incident
beam

α

stage

q_p

ionomer film formation
with solvent evaporation
morphology evolves with time (t)

$t = t^*$
film

$t = 0$
solution

(b) GIXS profiles at selected phases

63 nm   6.2 nm   6Å   3Å

solution

transition

ionomer
peak

crystalline
features

gel

10^1

10^0

I(q) [a.u.]

10^{-1}

10^{-2} 10^{-1} 10^0

q_p [Å^{-1}]

(c) Structural representation of ionomer aggregate

side-chain
backbone
side-chain
ionic group

~5.2 nm

~1.6 nm

solvated shell
backbone

Figure 5.1. (a) Schematic of *in-situ* printing technique for monitoring ionomer film morphology. (b) Composite GIXS linecuts showing evolution of morphology across lengthscales. (c) Schematic of Nafion aggregate and core-shell cylinder model used to fit the solution data.

Figure 5.2. (a) Horizontal GISAXS linecuts showing evolution of morphology from solution to film (b) Structure factor derived from dividing intensity by core-shell cylinder form factor (c) Peak positions from (b) evolving with time.

To extract an approximate structure factor, each linecut (shown in Figure 5.2a) is divided by the core-shell cylinder form factor, with a length of 40nm (from previous dilute-solution studies),[117] and the cross-sectional parameters obtained from fitting the high-q region. While the aggregate length may change from dilute solution to film, the form factor in the q-region of interest is insensitive to this parameter (Figure S5.2). Because of this insensitivity, changes in the form factor length will not change the approximate structure factor in this q-region and for this reason

59

we leave it constant. Two peaks are present in the structure factor (Figure 5.2b), and their positions vary with time (Figure 5.2c). As the solvent evaporates and the primary rod-like particles aggregate further, Peak 1's position monotonically increases with time, eventually collapsing as the solution transitions into a gel. This corresponds to a decrease in correlation length, i.e., d-spacing, from d_1 ≈ 12 nm to 6 nm in less than 50 seconds. Peak 2 shows non-monotonic behavior, first moving to lower q as the solution concentrates, before quickly advancing to higher q as the solution transitions to a gel. At 48 seconds, the film is now completely in the gel state and the second peak in the solution structure factor has become the "*ionomer peak*," which is related to the hydrophilic domain spacing in the film, d_2 ≈ 3 nm, and observed in previous GISAXS studies of spin-cast PFSA thin films.[27-28]. The evolution of the second structure factor peak into the ionomer peak highlights that the film morphology is set and mediated by interactions in ionomer solution, and by controlling these interactions one may be able to tune the final film morphology. As an example, it has been demonstrated that solvent composition affects the measured pH of PFSA dispersions, indicating differences in acid dissociation and ionomer aggregation.[118] It is expected that both the differences in solution interactions, as well as the mixed-solvent volatility, will impact the specific morphology and rate of the drying process. Subsequently, the film morphology continues to evolve slowly over the course of the next 600 seconds. In the film phase, the ionomer peak is fit to the Tuebner-Strey model for bi-continuous media (Equation S5.1),[119-120] and the extracted parameters $(\xi, \langle \eta^2 \rangle, \kappa)$ are plotted as a function of time in Figure 5.3 for both through-plane (thickness direction) and in-plane (parallel to the substrate) directions.
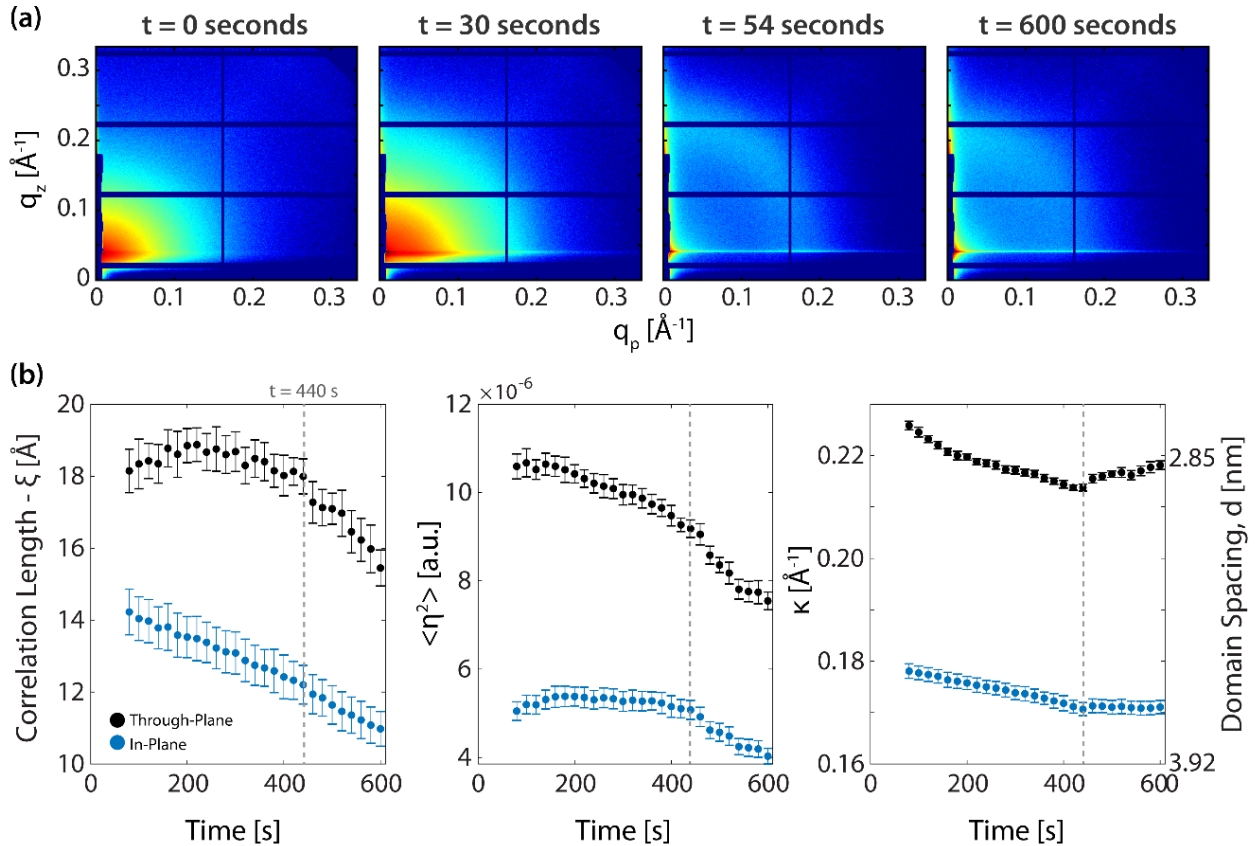
Figure 5.3. (a) 2D GISAXS images at selected time points (b) extracted parameters plotted as a function of time from fitting the Tuebner-Strey model to parallel and perpendicular line cuts.

60

In this model, ξ is the correlation length of ionomer domains and analogous to a full-width half max (FWHM) of the ionomer peak. $\langle \eta^2 \rangle$ is proportional to the scattering length contrast between phases, and κ is inversely proportional to the hydrophilic-domain spacing. Through the first 400 seconds, κ steadily decreases, corresponding to an increase domain spacing. Typically, a decrease in κ is observed as these materials hydrate with water, corresponding to nano-swelling of hydrophilic domains.[3] Since this is occurring as solvent continues to evaporate and the film dries, it suggests that the hydrophilic domains are coalescing into fewer domains that are spaced further apart. After ~440 seconds, κ begins to increase through-plane while leveling off in-plane as the hydrophilic domains stop coalescing and the film shows usual dehydrating behavior. After this transition point, $\langle \eta^2 \rangle$ and ξ both decrease more rapidly through-plane as the contrast between hydrophilic and hydrophobic domains decreases with reduced hydration. The in-plane transition does not show such a clear change in-plane, and this may be due to the evaporative flux occurring through-plane. As such, there is less of a driving force for morphological rearrangement in the plane of the film. While domain coalescence is complete at 440 seconds, mesoscale connectivity of the hydrophilic domain-network within the film may continue to evolve through dynamic fluctuations in a chemically heterogeneous, non-equilibrium structure. Notably, the film exhibits structural anisotropy immediately upon forming a gel or film, and that anisotropy is present throughout the morphological development.

An identical sample was cast in the GIWAXS configuration to probe smaller lengthscales, particularly crystalline features (Figure 5.4a). PFSAs have a PTFE backbone, and crystallize into the same structure as PTFE, but with a much lower degree of crystallinity due to side-chains interrupting the hexagonal packing of backbone chains. In the dispersion state, there is initially no crystallinity. Instead, there is a peak at 0.9 Å^{-1} (d ≈ 7Å) which is part of the core-shell cylinder form factor, and a solvent correlation peak at 1.5 Å^{-1}(d ≈ 4Å). Between t = 40–60 seconds, these peaks collapse, and a convoluted amorphous and crystalline peak appears at 1.2 Å^{-1}. This crystalline peak is from the <100> lattice plane and is commonly observed in PFSAs.[3] Thus, the onset of crystallization is concurrent with the solution-to-gel transition observed in GISAXS. The parameters extracted from the deconvoluted crystalline peak are plotted as a function of time after the first 60 seconds in Figure 5.4b-c. Immediately upon film formation, there is an observable orientation in the crystallites. Peak intensity is higher through-plane than in-plane, and the full-width half-max (FWHM) exhibits the opposite trend, indicating a preferential alignment of crystallites through-plane. This alignment continues to increase over time; the through-plane intensity increases, while the in-plane intensity remains constant. FWHM decreases marginally for both orientations as a function of time, indicating a slow growth in film crystallite size, a_c (which is inversely proportional to the FWHM through the relation, $a_c \propto 2\pi/\text{FWHM}$). The amorphous peak intensity decreases slightly for both orientations, again indicating marginal crystallization with time. Unlike ionomer domain coalescence, marginal crystallization appears to continue at ambient conditions very slowly, affecting the network connectivity of hydrophilic domains surrounded by the crystallites at longer lengthscales.
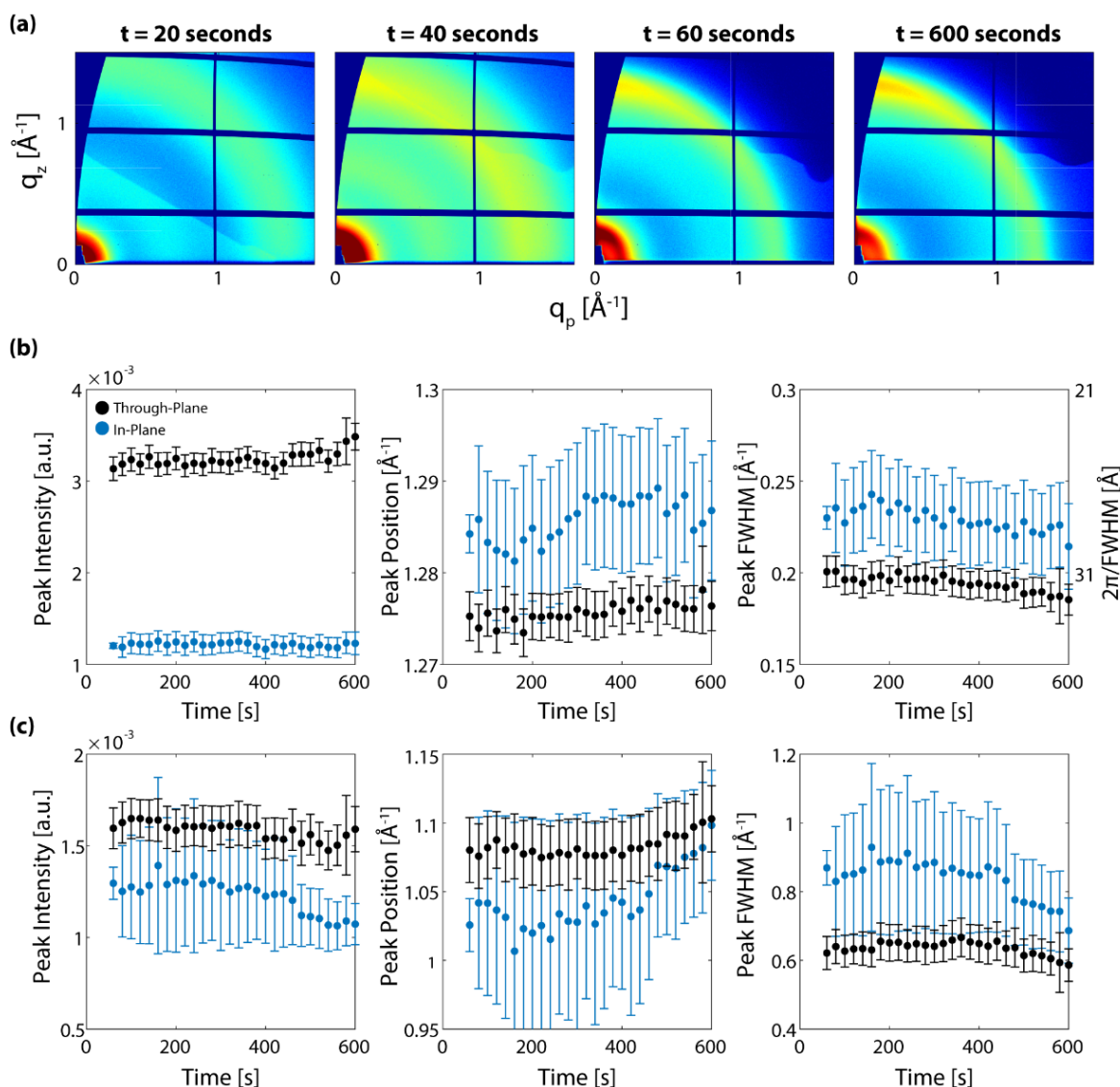
Figure 5.4. (a) 2D GIWAXS images at selected times, extracted (b) crystalline and (c) amorphous parameters as a function of time. A double-Gaussian was used to fit and deconvolute amorphous and crystalline peaks.

With the two experiments probing multiple lengthscales of ionomer film formation, a picture of the overall morphology emerges (Figure 5.5). The film formation of PFSA ionomer cast via slot-die printing proceeds through four stages: I. *Solution phase*, II. *Sol-Gel transition*, III. *Gel phase*, IV. *Film drying*. In Stage-I as the film is initially cast, solvent evaporates, concentrating the solution and inducing further primary particle aggregation. No backbone crystallinity is observed in this first stage. Then, the solution concentrates to a point where ionomer aggregates percolate into a gel-like phase and the structure factor peaks begin to collapse into the ionomer peak (Stage-II). In this stage (II), GIWAXS data shows the onset of crystallization and the convoluted amorphous/crystalline peak from the ionomer backbone is present in the GIWAXS patterns. The majority of crystallization is completed in Stage-II, although the crystallites continue to ripen marginally through stages III-IV. In Stage-III, the ionomer domains coalesce, forming fewer

domains that are spaced further apart. Thus, the decrease in κ, which proceeds steadily until Stage-IV, where the film exhibits drying behavior as the hydrophilic domains shrink and move closer together. While domain coalescence is complete at the end of Stage-III, crystallites continue to develop through Stage-IV and beyond the timescale of the experiment, impacting overall crystallinity and perhaps network connectivity.
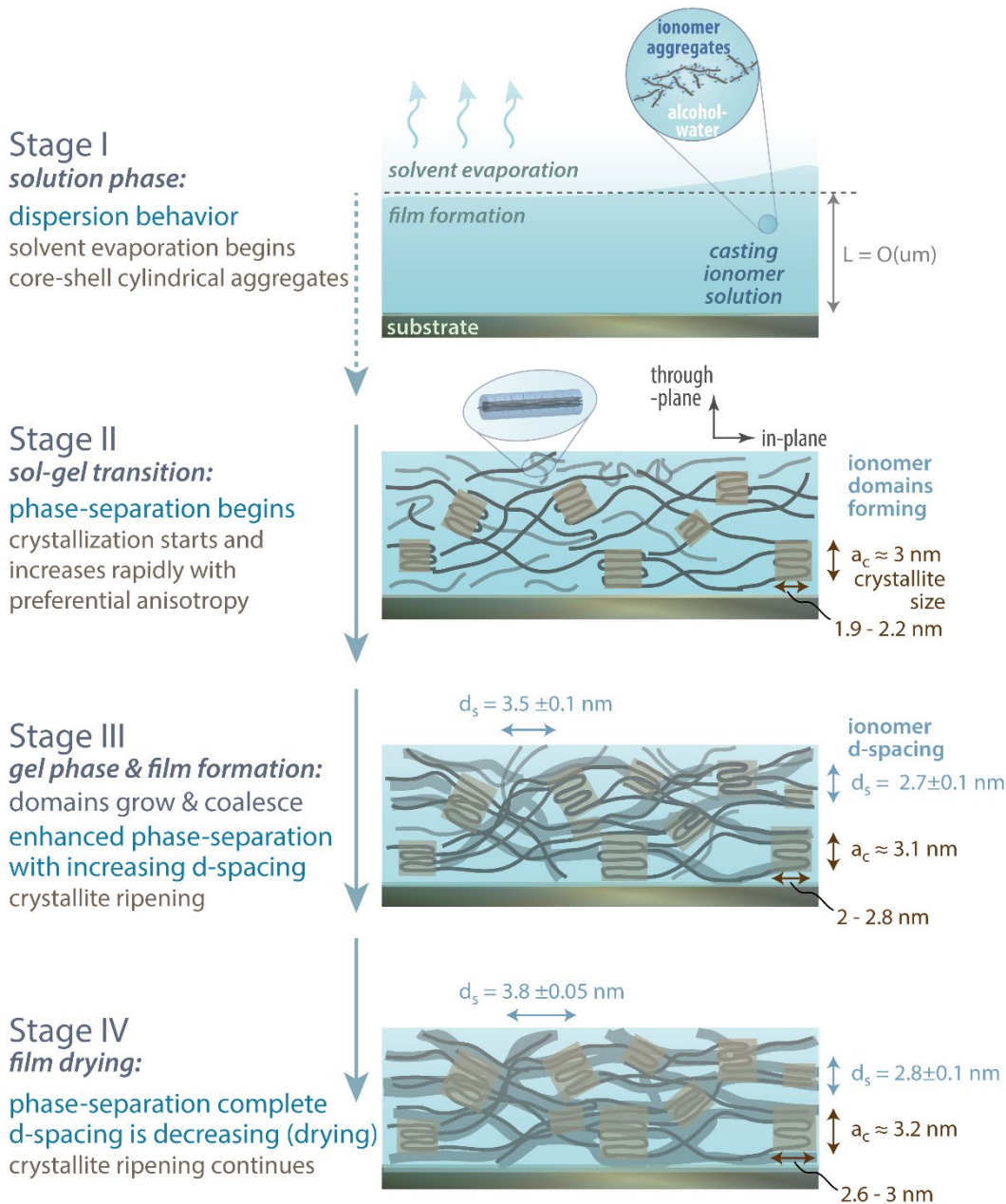
Figure 5.5. Illustration of the evolution of morphological features during formation of a PFSA thin-film from a dispersion based on the time-resolved GI(SAXS-WAXS) data.

Throughout the film formation process, there is an anisotropy in both the ionomer and crystalline peaks, highlighting the impact of confinement on the system. Crystallites are

63

preferentially aligned through-plane and the ionomer domains are spaced closer through-plane, which has implications for water and ion transport and subsequently catalyst layer performance. While preferential orientation of domains has been reported in spin-cast thin-films,[6, 14, 96, 121-123] this study reveals that the origin of such structural anisotropy is rooted in the film formation, during which crystallites and nano-domains orient with the substrate. Likely, this is due to the stiff rod-like aggregates aligning parallel to both interfaces as the solution evaporates and transitions into a thin film. The preferential interaction of ionomer moieties with the substrate interface through the ionic groups facilitate this alignment of the backbone chains constituting the polymer aggregates.[124] Prior work has demonstrated anisotropic transport and proton conductivity in ionomer thin-films,[125-127] accompanied by higher stiffness,[5] which is attributed to preferential alignment of domains within the film.[6, 14, 123-126, 128] Controlling this alignment and ultimately the phase-separated morphology is important for improving catalyst-layer performance, and how to achieve tunability is an open question.

Findings herein illustrate the key role of film formation during casting in setting a morphology, which indicates tuning of ionomer-solvent interactions, processing via casting method, and temperature control as possible routes to control film functionality.
The fact that hydrophobic semi-crystalline domains and polar domains evolve at different timescales during film formation underscores the key role of ionomer's chemically dissimilar phases and their preferential interactions with the solvents (*e.g.,* alcohol vs. water) in morphology.
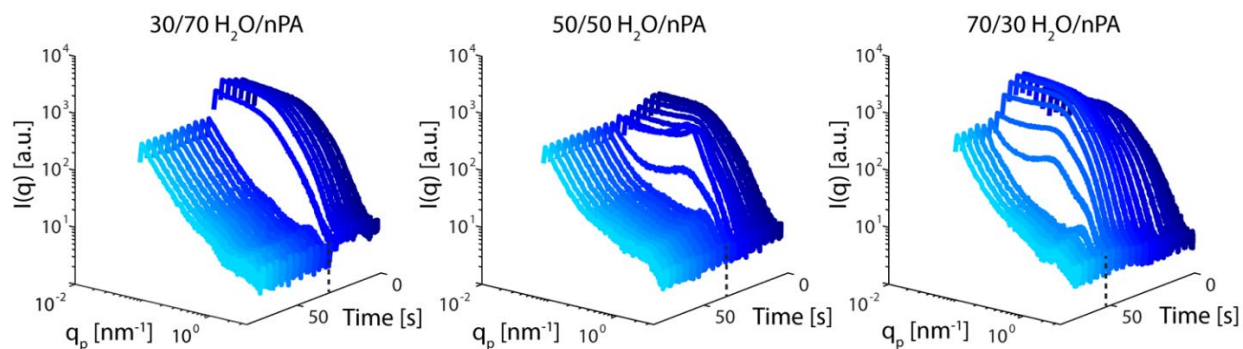
Figure 5.6. *In-situ* GISAXS casting of different solvent ratios, demonstrating the effect of solvent composition on non-equilibrium morphology evolution. Dashed lines in each plot denote the time at which the film transitions from solution to gel.

To demonstrate this further, we cast Nafion films from different solvent ratios of water to n-propanol (nPA) at the same weight percent and have plotted horizontal GISAXS linecuts with time (Figure 5.6). Across the three solvent ratios, all show markedly different transitions from solution to film and reach their gel point at different times. This gelation time scales with increasing water content in the solution; less-volatile mixtures have a lower evaporative driving force. In addition, the structure factor peaks across the samples all differ due to local solvent environment around the ionic group. These differences subsequently lead to varying interaction strengths and degrees of aggregate ordering. While the impact of these structural changes on properties warrant further investigation, the solvent type and composition appears to have a significant impact on the evolution of morphology from solution to film.

To conclude, the continued ripening of crystallites beyond the timescale of the initial experiment, along with their preferential orientation, brings up the questions of film aging and long-term relaxation, and how they impact film behavior and functionality. Demonstration of this powerful technique for ionomer film formation serves as a baseline for subsequent studies to explore roles of materials and processing parameters in understanding and manipulating structure-functionality of ion-exchange thin-films for various technologies, including the electrodes of energy conversion devices.

5.4 Supporting Information

5.4.1 Distorted Wave Born Approximation (DWBA)
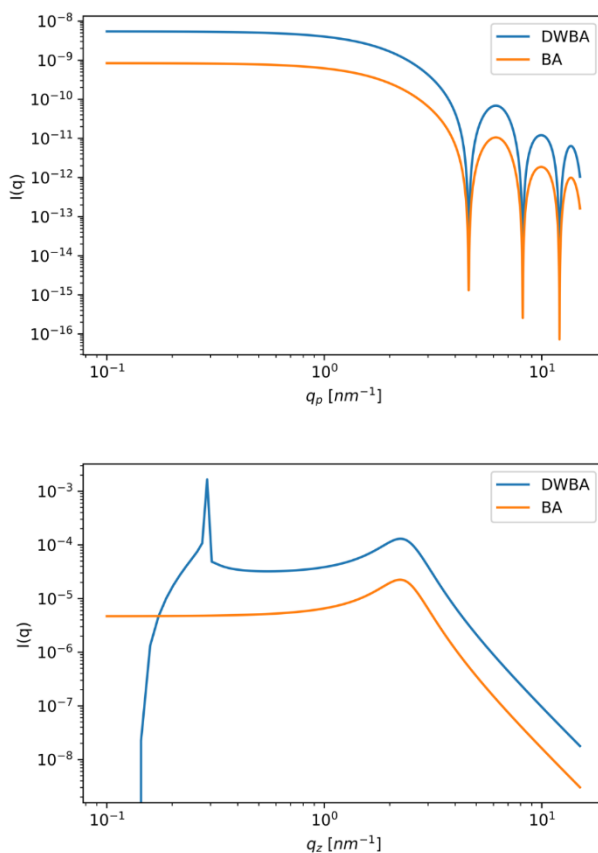
Figure S5.1. a) Form factor for a single core-shell cylinder, oriented perpendicular to sample normal. The simulated horizontal linecuts are at $q_z = 0.4$ nm^{-1}, the same location as the horizontal linecuts in the main manuscript. b) Teubner-Strey Model simulated in DWBA and BA. The vertical linecut is take at $q_p = 0.4$ nm^{-1}.

Due to the grazing incidence geometry, reflection and refraction events within the film and at interfaces can occur.[30] If these are significant enough, it can modify the form factor and observed scattering, making it necessary to fit within the Distorted Wave Born Approximation (DWBA) framework. The form factor for a core shell cylinder is simulated in the DWBA and Born Approximation (BA), shown in Figure S5.1. There is a slight difference in scaling, but the positions

65

of the form factor minima remain the same. Thus, the additional scattering events are negligible for the solution portion of the analysis, and don't modify the observed particle shape. Because of this, the core-shell cylinder fitting in this paper is done within the BA for its simpler models and existing software packages. The Teubner-Strey model was also considered in the DWBA framework.[129] Figure S5.1 compares the model in DWBA and BA, assuming a Nafion layer of 200 nm on top of a silicon substrate. Away from the Yoneda peak, there are no differences.

Refraction can also affect the observed peak position. For this system, as the film is drying, the index of refraction (and thus the critical angle) will increase with solvent evaporation and it should be slightly different for each image. Unfortunately, the angular resolution at the Yoneda peak is not high enough to resolve the critical angle of the drying film versus the critical angle of silicon. Without resolving the film's Yoneda peak, we cannot take into account the refraction effects in a consistent manner. Future experiments can be conducted with an in-situ interferometer to collect optical constants with time. Despite this, the trends observed in the main text through-plane are consistent with the trends in-plane, where refraction does not affect q-spacing. Additionally, as solvent evaporates and the index of refraction increases with time, the shift due to refraction would only enhance the trend we observe through plane.

5.4.2 Core-Shell Form Factor

Figure S5.2 shows the core-shell cylinder form factor, plotted with a composite linecut from the solution portion of the manuscript. To extract the structure factor in Figure 5.2b of the main text, the linecut was fit at high-q (0.24-3 Å⁻¹). For this disordered system, the structure factor should be 1 in this q-range, and only the form factor will contribute to the observed scattered intensity. As the solution dries, it is possible for the length of the cylinders to change. For this reason, we have plotted the form factor with a wide range of cylinder lengths. Because the cylinder length is much greater than the cross-sectional dimension, the form factor is relatively insensitive to this parameter in the region of interest (q > 0.015 Å⁻¹).
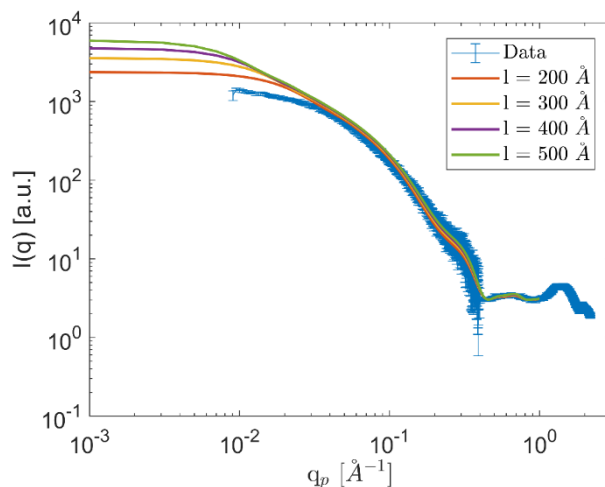
Figure S5.2. Early time solution morphology and Core-Shell Cylinder form factor of various lengths.

Figure S5.3 shows linecuts and sectorcuts of the film as it evolves from solution to gel. The peak at 0.9 Å^{-1} is part of the core-shell cylinder form factor. The peak at ~1.5 Å^{-1} is attributed to solvent-solvent correlations. This peak disappears as the film dries and enters the gel stage.
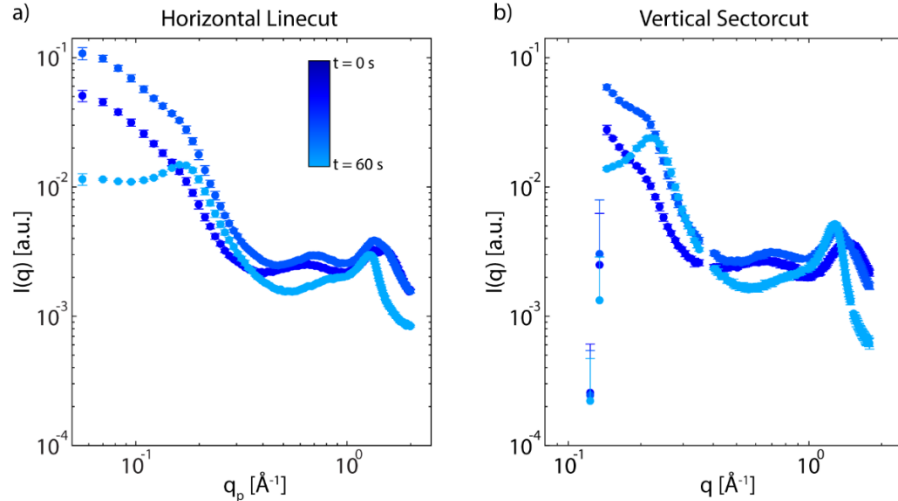
Figure S5.3. a) Horizontal line-cuts and b) vertical sector-cuts of GIWAXS images at early time.

5.4.3   GISAXS Ionomer Peak Fitting

The ionomer peak was fit to the Teubner-Strey Model (Equation S5.1), originally developed for micro-emulsions but applicable for random bi-continuous structures.[120, 130] The fittings parameters are $\langle \eta^2 \rangle$, κ, and ξ.

$$I(q) = \frac{8\pi \langle \eta^2 \rangle}{\xi(a - 2bq^2 + q^4)} \tag{S5.1}$$

$$a = \left(\kappa^2 + \frac{1}{\xi^2} \right)^2 \qquad\qquad b = \left(\kappa^2 - \frac{1}{\xi^2} \right)$$

As discussed in the main text, $\langle \eta^2 \rangle$ is a function of volume fractions and the scattering length contrast. κ is inversely related to the spacing between domains, and ξ is the correlation length of domains. Typically, PFSA ionomer studies will report domain spacing as

$$d = \frac{2\pi}{q_{max}} \tag{S5.2}$$

Here we note that q_{max} is related to the extracted parameters via

$$q_{max} = \sqrt{\kappa^2 - \frac{1}{\xi^2}} \tag{S5.3}$$

The difference between q_{max} and κ is small for this set of data, but the authors note this for clarity. Below is a typical fit of the data on log-log and linear scales.
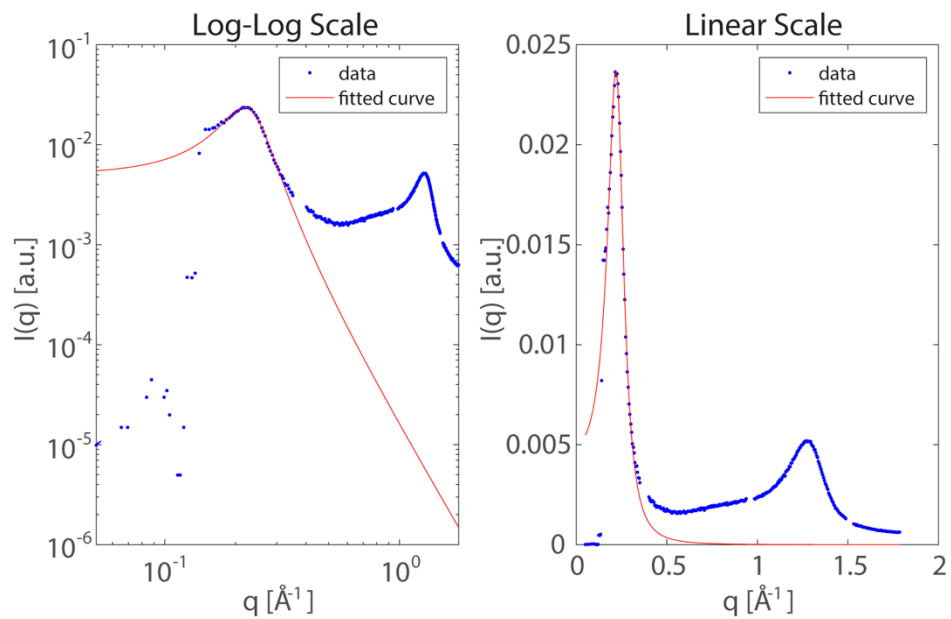
Figure S5.4. Fit of the Teubner-Strey model to experimental data on log-log and linear scales.

6 Role of Crystalline Structure in Modulus-Swelling Relationship for Annealed PFSA Thin Films

6.1 Introduction

The phase-separated nanostructure of PFSA material confers it the ability to have robust mechanical properties and high ion-conductivity.[3] The hydrophobic-backbone-phase provides a majority of the mechanical stability to the material, while the hydrophilic region consisting of the pendant side-chain and acid group provides a pathway for ion-conduction upon hydration. Despite being phase-separated, mechanical and transport properties are nonetheless closely correlated. This is due to the transport properties' strong dependence on water content, which is ultimately influenced by the mechanical properties.[131-132] In bulk PFSA membranes, numerous studies have demonstrated the inverse chemical-mechanical relationship between modulus and water content, where the modulus is a function of annealing temperature,[132] cation type,[11] and the environmental measurement conditions.[133]

One of the more facile ways to control the modulus is via annealing, where the modulus increases with increasing annealing temperature, and the water content and transport properties decrease.[132] Studies have also correlated the modulus to the PFSA nanostructure via small-angle x-ray scattering (SAXS). One of the characteristic features observed with SAXS is the "matrix knee," which has been attributed to the distance between crystallites within the material. With increasing annealing temperatures, a growth in the matrix knee peak is observed and credited to an increase in crystallinity.[10] Fewer studies have quantified the effect of annealing temperature on the degree of crystallinity using wide-angle x-ray scattering (WAXS), and the studies that have been conducted using WAXS offer conflicting results.[134-135]

Within porous electrodes or catalyst layers, PFSAs exist as nanometer-thick thin films and function as an electrolyte binder. To understand and optimize reactant and water transport in PFSA thin films, it is necessary to elucidate the chemical-mechanical relationship of PFSA thin films. One assumes that the governing hydration-modulus relationship in thin films could be altered/tuned by means of thermal annealing similar to that in bulk PFSA, yet very few studies have looked at the mechanical properties of PFSA thin films with annealing temperature,[61] and no studies currently exist looking at the effect of annealing temperature on PFSA thin-film crystallinity. Thus, to understand how structure-property relationships established for bulk PFSAs are affected in thin films, it is critical determine how the nanostructure is affected by different processing conditions and how it impacts mechanical and hydration properties.

In this study, the crystallinity of Nafion thin films is quantified via GIWAXS and correlated to mechanical properties measured using a cantilever bending method. By varying film thickness and annealing temperature, the impact of confinement and processing on the nanostructure and mechanical properties is determined.

6.2 Experimental Methods

6.2.1 Sample Preparation
Ionomer solutions. Nafion®-ionomer dispersion (5-wt% solids of 1100 g polymer (mol SO_3^-)$^{-1}$ in alcohol-water mixture) were obtained from Sigma Aldrich. (St. Louis, MO) and diluted with isopropyl alcohol (IPA) to achieve different thicknesses upon spin coating.

Substrate preparation. Samples for GIWAXS were prepared on silicon wafers diced into 1.5x1.5 cm pieces. Samples for the cantilever bending method were prepared on thin double-side polished silicon wafer diced into 5x4 cm pieces. Each silicon wafer piece was rinsed successively in acetone and IPA followed by drying under a dry nitrogen stream directly prior to spin coating.
Spin coating. Films were spun cast using a Laurell Technologies WS-650-23B spin coater. Nafion solution was pipetted onto the silicon wafer piece and spun cast at 3000 rpm for 1 minute. 250 µL of solution was used for the 1.5x1.5 cm pieces, and 2 mL of solution was used for the 5x4 cm pieces.
Annealing. Each set of spun-cast films were loaded into a vacuum oven and annealed at the respective annealing temperature (150, 175, or 200°C) for 12 hours. After 12 hours, the oven was turned off to let the samples cool slowly under vacuum to room temperature over the next 24 hours.

6.2.2 GIWAXS
Data Collection. GIWAXS measurements were performed at beamline 7.3.3 of the ALS at LBNL.[48] The X-ray energy was 10 keV (λ=1.24 A^{-1}) with a monochromator energy resolution E/dE of 100, and the patterns were acquired with a Dectris Pilatus 2M CCD area detector (172 µm x 172 µm pixel size). GIWAXS images were collected under helium at α_i = 0.16° with a 5 second exposure time and α_i = 7.1° with a 20 second exposure time.
Relative degree of crystallinity (rDoC) and Orientation Parameter (OP). Calculation of the rDoC and orientation parameter follow previously established methods[27-28] and is described in greater detail in Chapter 1. For the low angle image, 5° sector-cuts were taken from 10°-80° after correcting for the geometry. The background was fit to a power law and subtracted for each sector cut, and amorphous and crystalline peaks were deconvoluted by fitting a double-gaussian. Once deconvoluted, each peak was integrated to create a pole figure, or intensity versus azimuthal angle, χ. The procedure was repeated for the high-angle image for 0° to 30°, and the low-angle pole figure was scaled and merged with the high-angle pole figure. This composite pole figure was integrated to calculate rDoC using

$$rDoC = \frac{1}{c_a} \int I(\chi) \sin[\chi] \, d\chi, \qquad (6.1)$$

and OP using

$$OP = \frac{\int I(\chi) \sin[\chi] \cos[\chi]^2 \, d\chi}{\int I(\chi) \sin[\chi] \, d\chi}, \qquad (6.2)$$

where χ is the azimuthal angle, $I(\chi)$ is the integrated intensity as a function of χ, and c_a is an absorption correction.

6.2.3 Cantilever Bending Method
Samples were diced into sections for the cantilever bending method and ellipsometry. Each section was measured in both experiments simultaneously under the same relative humidity protocol: The sample was dried at 0% RH for 30 minutes, followed by 30 minutes at >95% RH. Then the sample was dried again at 0% RH for 60 minutes. The end of the second 60-minute drying period was taken as the reference point for thickness in ellipsometry and curvature in the cantilever bending method. Humidity was stepped in 10% RH increments for 30 minutes at each step, up to a 100% RH setpoint (actual between 95 and 100%). From each set of experiments thickness and curvature are plotted versus RH, respectively. Any differences in the reached setpoints in the two

experiments was accounted for by interpolating between data points. Thickness and curvature versus RH were used to generate stress versus swelling strain curves using

$$\sigma_f t_f = \frac{E_s t_s^2 \Delta\kappa}{6(1-\nu_s)} \tag{6.3}$$

where σ_f is the stress, t_f is the film thickness, E_s, t_s, and ν_s are the Young's modulus, thickness and Poisson's ratio of the substrate, respectively. $\Delta\kappa$ is the change in curvature of the substrate. The shear modulus is calculated from the stress-strain curve in the limit of zero swelling strain. Further discussion of the cantilever bending method is contained in Chapter 2.

6.3 Results and Discussion

6.3.1 Crystallinity and Orientation
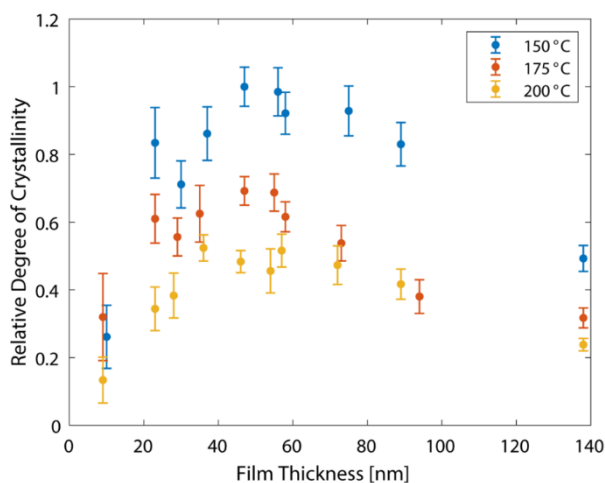
Figure 6.1. Relative degree of crystallinity (rDoC) versus thickness for Nafion thin films annealed at three different temperatures.

Figure 6.1 plots the relative degree of crystallinity (rDoC) versus film thickness for each set of Nafion thin films. The rDoC is suppressed with increasing annealing temperature for all thicknesses. There are conflicting results within the literature on crystallinity, where morphological studies on PFSAs membranes have previously reported both an increase[134] and decrease[135] in crystallinity with annealing temperature. Work by Page et. al demonstrated an endothermic peak in differential scanning calorimetry (DSC) that increases with increasing annealing temperature, which they attributed to the melting of small, imperfect crystallites.[21] This melting behavior is observed in a variety of semi-crystalline polymers, where small or thin lamellae melt below the bulk melting temperature.[136-137] The annealing conditions in this study are below the bulk melting temperature of PTFE crystallites (327°C). Likely, with higher annealing temperatures, a greater fraction of small, imperfect crystallites melt. Once melted, the driving force for ionic-group aggregation and clustering may prevent backbone recrystallization and thickening of larger crystals, suppressing rDoC. Previous studies that used WAXS to qualitatively examine the crystalline peak observed a sharpening of the peak with annealing temperature, and concluded

there was a growth in crystal size and crystallinity.[10] We also observe a sharpening of the crystalline peak in this study despite a decrease in the degree of crystallinity. This can be explained by the fact that when small crystals melt and do not reform, the average crystal size within the film is now larger. This average, or statistical distribution, in crystal is size is precisely what is measured using (GI)WAXS.

Since the matrix knee for bulk PFSA membranes in SAXS has been shown to consistently grow stronger with increased annealing time and temperature, the trend in rDoC with annealing temperature suggests the matrix knee is not directly related to the degree of crystallinity as previously ascribed. Though the matrix knee peak is stronger in more crystalline PFSAs,[123] it may be related more directly to the regularity of inter-crystallite spacing. For temperatures above the α-transition, the larger crystals that do not melt may redistribute with more uniformity. Studying the matrix knee peak and degree of crystallinity within the same sample should be done to determine the exact relationship more conclusively.

Within each annealing temperature, rDoC increases with decreasing film thickness to a maximum between 40 and 60 nm. Reducing the film thickness may align more chains parallel to the interfaces and reduce the entropic barrier to crystallization.[138-139] As the film thickness is reduced further, rDoC drops sharply with decreasing film thickness. Previous studies on PFSA thin films have shown a transition in different properties in the same 40 to 60 nm region,[4-5, 61] which points to a characteristic lengthscale that exists within the material, where backbone crystallization is impeded; reducing film thickness further decreases rDoC.

To compare the relative change in rDoC at each annealing temperature, each set of films is normalized to the highest rDoC within that set. Figure 6.2 shows this normalized rDoC plotted versus thickness. The three sets of films now collapse onto each other, indicating that confinement effect on crystallinity is consistent across annealing temperatures. The effect of annealing temperature is separate and distinct from confinement effects.
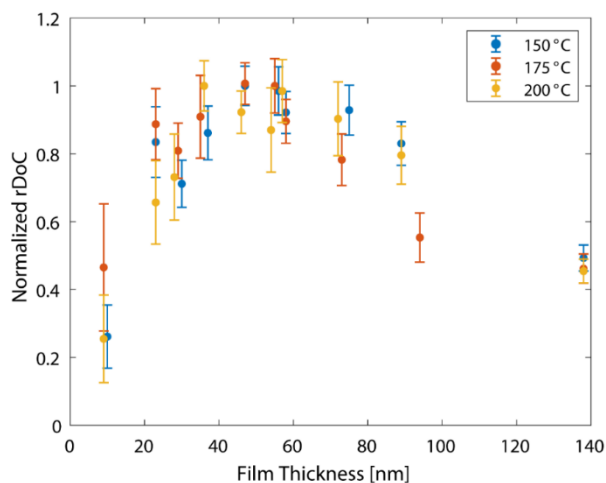
Figure 6.2. Normalized rDoC versus film thickness for Nafion thin films. The set of films for each annealing temperature is normalized by the maximum rDoC at that temperature.
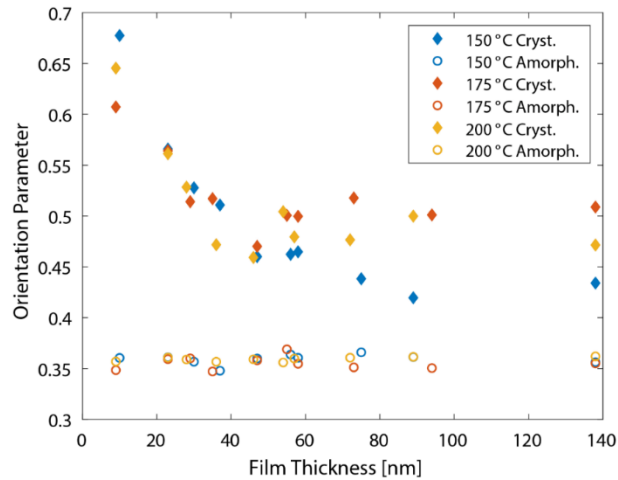
Figure 6.3. Orientation parameter versus film thickness for the crystalline and amorphous peaks of Nafion thin films annealed at three different temperatures.

Figure 6.3 plots the orientation parameter for the crystalline and amorphous peaks versus film thickness for the three sets of Nafion films. In all three sets, for all film thicknesses, the amorphous peak has an isotropic orientation distribution. The crystalline peak does not exhibit a dependence on annealing temperature except for the thickest films, where higher annealing temperature seems to slightly promote more oriented crystallites, increasing the OP from 0.44 to 0.51. As film thickness is reduced, OP is relatively constant until ~50 nm where it begins to increase indicating crystallites are becoming more oriented through-plane. This 40 to 50 nm region is the same point at which rDoC begins to sharply decrease for all three annealing temperatures, which further supports that below this transition point crystallite formation is becoming disrupted and crystallites are forced to orient with the decreasing film thickness. The observed orientation of these crystallites may also affect ionomer domain orientation and has implications for the direction and magnitude of gas and proton transport through PFSA thin films in catalyst layers.

6.3.2 Mechanical and Swelling Properties

To connect the nanomorphology to physical properties, thin-film samples were prepared under the same conditions and their mechanical properties measured with the cantilever bending method. A shear modulus is calculated from stress-strain curves generated by the cantilever bending method and ellipsometry experiments, and the shear modulus is plotted versus film thickness in Figure 6.4a.
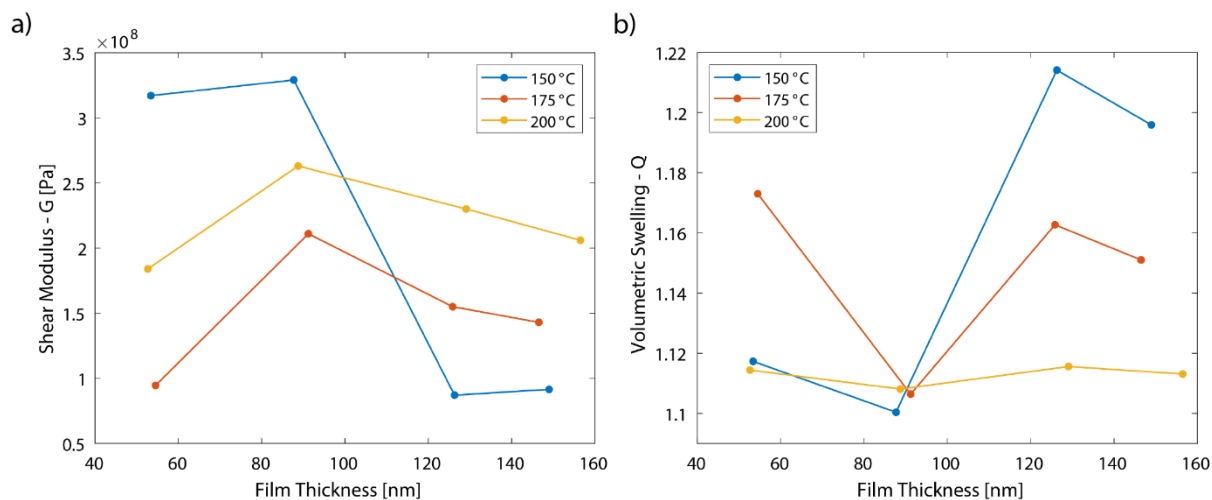
Figure 6.4. a) Shear modulus and b) volumetric swelling at 95% RH plotted versus film thickness for Nafion thin films annealed at three different temperatures.

For the thickest films above 120 nm, the shear modulus increases with increasing annealing temperature, which is consistent with bulk studies.[131] This trend changes as film thickness decreases below 100 nm, where the films annealed at 150°C have the highest measured shear modulus followed by 200°C and then 175°C. All three sets of samples show an increase then decrease in shear modulus, with a maximum value at ~90 nm. This increase then decrease in shear modulus with thickness is similar to what is observed in normalized rDoC, though the maximum for each is offset from one another. The trends in shear modulus are opposite to what is observed for swelling at 95% RH (Figure 6.4b). At the thickest films above 120 nm, the volumetric swelling decreases with increasing annealing temperature. As the film thickness is reduced, the volumetric swelling has a minimum at ~90 nm before increasing again.

At the macroscale, the chemical-mechanical balance between water sorption and modulus is well established in bulk PFSA membranes: for a higher modulus, the film will swell to a lesser degree at the same water activity. To test if this relationship is valid under these annealing conditions, the dry shear modulus is plotted versus the volumetric swelling at 95% relative humidity (Figure 6.5). The shear modulus and volumetric swelling show an inversely linear relationship on a log-log scale, which is consistent across annealing temperature and film thickness. Similar results have been shown in literature with different annealing protocols.[61] This chemical-mechanical balance established in bulk PFSA membranes appears to hold also in PFSA thin films, regardless of film thickness, annealing temperature, and annealing protocol. Using the above relationship, measuring water uptake may be used as a proxy to elucidate the mechanical properties of thin films.
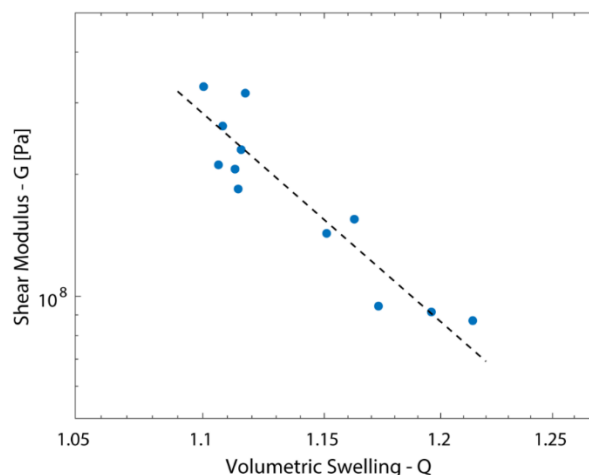
Figure 6.5. Dry shear modulus plotted versus volumetric swelling at 95% RH.
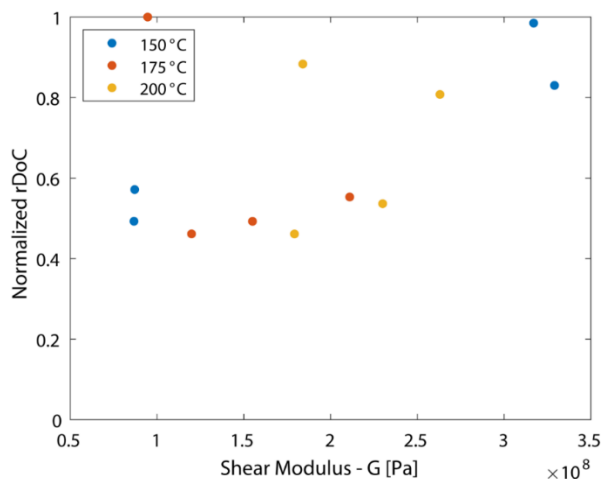
Figure 6.6. Normalized rDoC plotted versus shear modulus for three different annealing temperatures. There is a general positive correlation between normalized rDoC and shear modulus.

To determine if there is a correlation between crystallinity and shear modulus, normalized rDoC is plotted versus shear modulus in Figure 6.6. A general positive correlation exists between normalized rDoC and the shear modulus, but the correlation is not strong. This highlights that crystallinity is not the lone factor in determining the mechanical properties for PFSA thin films. The properties of the amorphous and hydrophilic regions also contribute to the overall mechanical response of these materials. One study looked at the impact of annealing temperature on the α-transition and found it increased from 110 to 120°C when annealing at 70 vs 100°C, respectively.[140] While this effect needs to be studied further, if the α-transition continues to increase with increasing annealing temperature it could change the effective quench depth of the material. In traditional glassy materials, the quench depth at which a material is measured affects the physical properties.[141] Thus, if films annealed at different temperatures have different α-transition temperatures, this would affect the measured mechanical properties.

In addition to contributions from amorphous and hydrophilic regions, mesoscale effects may also be an important factor. While these films are all thicker than the transition point in OP such that the orientation of crystallites within the film are similar, the film may be oriented differently at longer lengthscales, which necessitates further investigation. The connectivity of the crystalline, amorphous, and hydrophilic regions, and the relative orientations of each of these domains are all contributing factors to the observed macroscopic mechanical properties.

6.4   Summary and Conclusions

The relative degree of crystallinity (rDoC) and orientation of crystallites are determined for three sets of PFSA thin films annealed at different temperatures. rDoC decreases with increasing annealing temperature and demonstrates a non-monotonic change with film thickness. Crystallites become more oriented through-plane below 50 nm, with a simultaneous sharp decrease in rDoC. At larger film thicknesses, the shear modulus measured by cantilever bending method increases with increasing annealing temperature, reminiscent of trends observed for bulk ionomers. As the film thickness reduces, the shear modulus increases, with a maximum value around 90 nm for all three annealing temperatures. While a positive correlation between rDoC and shear modulus exists, it is weak probably due to mesoscale-network effects, which need to be considered to make a more rigorous connection between mechanical properties and crystallinity. However, a strong inverse relationship is found between the shear modulus and maximum hydration swelling as measured by ellipsometry. Thus, the chemical-mechanical balance observed in bulk PFSA membranes is demonstrated to be valid for thin films as well, and swelling can potentially be used as a proxy for probing mechanical properties in thin films.

7 PFSA Ionomer Structure and Water Uptake Across the α-Transition Temperature

7.1 Introduction

Since its discovery, Nafion has been the prototypical PFSA ionomer used in electrochemical energy conversion devices. The high proton conduction, low gas-permeability, robust mechanical properties, and good chemical stability make it an excellent material to use as the ion-conducting membrane separating electrodes. Within the catalyst layer, however, the low gas permeability of PFSA thin films is a detriment to device performance. For fuel cells, several studies at low platinum loadings have shown that oxygen transport in the ionomer film of the catalyst layer is the limiting factor for device performance.[7, 142] Because of this, there has been a push for developing new ionomers that have better react transport. Transport properties may be prioritized over mechanical stability, which is somewhat less important for ionomer films confined in the catalyst layer compared to ionomer membranes.

One way to improve water uptake and reactant transport is to increase the density of side-chains terminated in sulfonic-acid groups. The side-chain density is often characterized by equivalent weight (EW), which is the grams of polymer per sulfonic-acid group. Lower EW leads to a higher side-chain density, which increases the driving force for water sorption leading to greater water volume fraction and potentially improved domain connectivity. The 3M Company has developed a library of PFSAs with varying EWs and chemistries, which, in bulk form, exhibit a clear scaling relationship between water uptake and proton conductivity with EW. Additionally, a higher side-chain density leads to a decrease in crystallinity of the hydrophobic backbone in these materials. For Nafion and a subset of these 3M PFSA ionomers, the inverse relationship between EW and water uptake continues to be valid for thin films.[123]

Prior studies in thin films have only looked at structure-property relationships for single annealing temperatures. Within bulk, different annealing temperatures have been shown to affect water uptake and conductivity[143-144] and Chapter 6 demonstrated the effect of annealing temperature on crystallinity in Nafion thin films. In this work, we studied the effect of annealing temperature on the morphology and water uptake for four 3M PFSA ionomer EWs (620, 725, 825, 1000 EW) and Nafion 1100 EW. Grazing incidence small-angle x-ray scattering (GISAXS) was used to probe the morphology at ambient and humidified conditions and ellipsometry was used to measure water uptake. We annealed the samples at varying temperatures from 50 to 175°C; this range of annealing temperatures is across the α-transition as observed in bulk PFSA membranes and is attributed to the breaking of the electrostatic network governed by the sulfonic-acid groups. We hypothesized that above the α-transition, a greater morphological rearrangement would occur and that it would impact the observed water uptake.

7.2 Experimental Methods

7.2.1 Sample Preparation

Ionomer solutions. Nafion®-ionomer dispersion (5-wt% solids of 1100 g polymer (mol SO_3^-)$^{-1}$ in alcohol-water mixture) were obtained from Sigma Aldrich. (St. Louis, MO) and 3M-ionomer dispersions (620, 725, 825, and 1000 g polymer (mol SO_3^-)$^{-1}$) were provided by the 3M Fuel-Cells Component Group (St. Paul, MN). All ionomer solutions were diluted from 20 or 25 wt% to 1.5 wt% with n-propyl alcohol (nPA).

Thin film preparation. Samples were prepared on silicon wafers diced into 1.5x1.5 cm pieces. Films were spun cast using a Laurell Technologies WS-650-23B spin coater. 250 µL of ionomer solution was pipetted onto the silicon wafer piece and spun cast at 3000 rpm for 1 minute. After spin casting, samples were annealed under vacuum for 1 hour at 50, 75, 100, 125, 150, or 175°C, respectively. After 1 hour, samples were removed from the vacuum oven to air cool.

7.2.2   Sample Characterization

GISAXS Data Collection. GISAXS measurements were performed at beamline 7.3.3 of the ALS at LBNL. The X-ray energy was 10 keV (λ=1.24 A^{-1}) with a monochromator energy resolution E/dE of 100, and the patterns were acquired with a Dectris Pilatus 2M CCD area detector (172 µm x 172 µm pixel size). GISAXS images were collected at ambient and humidified conditions at $\alpha_i = 0.2°$ with a 5 second exposure time.

Orientation Parameter (OP). Calculation of the orientation parameter follows Roe et. al[27] and is described in greater detail in Chapter 1. 4° sector cuts were taken from 0-70° after correcting for the geometry. Over this azimuthal range, an OP value of ~0.48 represents an isotropic sample.

Ellipsometry. Sample thickness as a function of relative humidity (RH) was measured with a J.A. Woolam Alpha Spectroscopic Ellipsometer. Humidity was controlled with a lab-built humidity control system. Samples were exposed to a break-in cycle at 0% and 95% RH for 30 minutes each before measuring the swelling isotherm. The isotherm was generated from 0 to 100% RH in 10% increments for 30 minutes at each RH condition. The last 5 minutes of each humidity condition was averaged as the equilibrated thickness.

7.3   Results and Discussion

Figure 7.1 plots horizontal linecuts from GISAXS for each equivalent weight and annealing temperature at the humidified condition. For both chemistries and all EWs, there is a general trend of the ionomer peak moving to higher q-spacing with increasing annealing temperature. Prior studies have shown the q-spacing correlates inversely to water content,[2-3] where increasing annealing temperature decreases the water content at a given water activity, which increases the observed q-spacing. The "matrix knee" also has a temperature dependence. For 3M 620 and 725 EW, the matrix knee is only present at 125°C. The matrix knee for 3M 825, 1000 EW, and Nafion 1100 EW also appears at 125°C but persists at higher annealing temperatures. The α-transition (T_α) in bulk 3M and Nafion ionomers is between 100 and 125°C.[3, 11, 145] When the ionomer film goes through T_α, the ionic network comprised of sulfonic acid-group bridges is broken and the polymer chains become mobile at a longer length scale. This allows the film morphology to rearrange and the matrix knee to form. Figure 7.1 shows that the matrix knee peak is more pronounced at higher EW. Ionomers with higher EW have a higher degree of crystallinity because there are less pendant side-chains to interrupt crystallite formation and these results confirm that the matrix knee does depend on crystallinity. With higher EW and a proportionally higher degree of crystallinity, the matrix knee is more pronounced and moves to higher q-spacing as more crystallites are present and closer together. However, the results in Chapter 6.3.1 show that the matrix knee is not directly proportional to the relative degree of crystallinity and instead has a more complicated relationship that also depends on how crystallites are distributed through the film: for annealing temperatures at 150°C and above, there is a decrease in relative degree of crystallinity (Figure 6.1). Comparing the Nafion 1100 EW and 3M 1000 EW (which has the same side-chain spacing as Nafion) data at 150 and 175°C to the results in Chapter 6.3.1, the matrix knee moves to lower q. As imperfect crystallites are melted, the remaining larger crystallites are spaced further apart, but potentially at a more regular spacing/distribution.
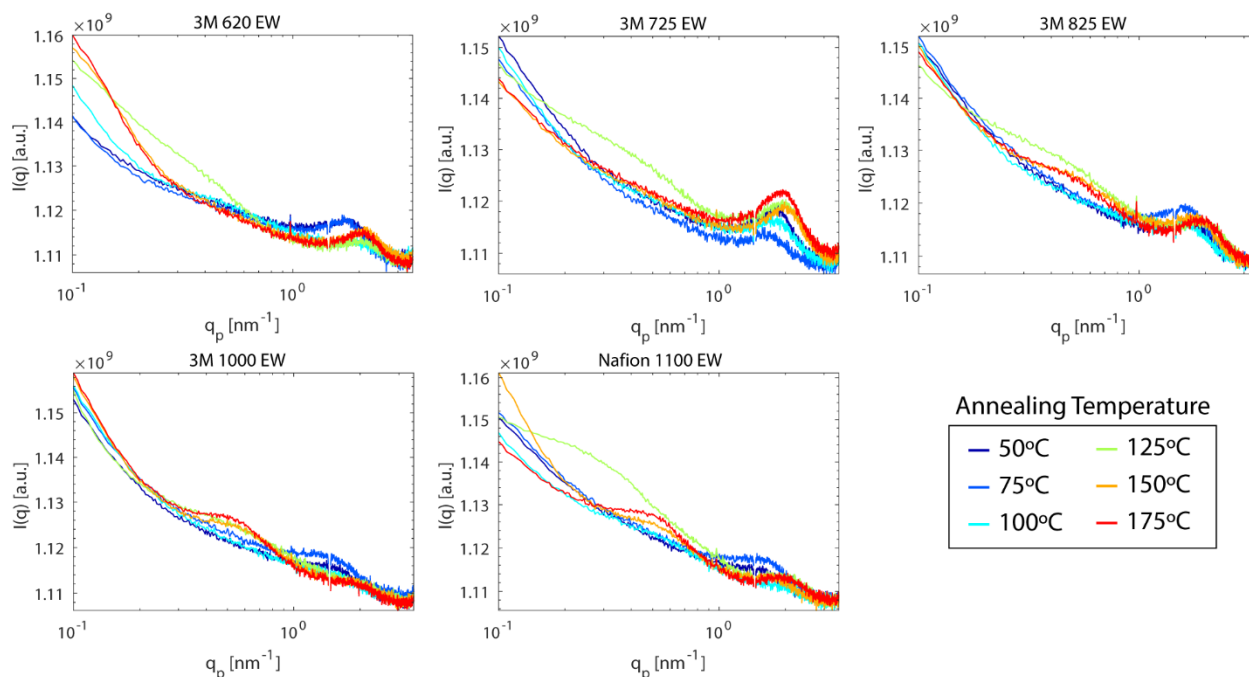
Figure 7.1. GISAXS in-plane linecuts for 3M 620, 725, 825, 1000 EW and Nafion 1100 EW.

The horizontal linecuts show a clear transition in the matrix knee, which is centered in-plane. To understand how the orientation of the ionomer domains changes with annealing temperature, sector cuts were taken as a function of χ, and the ionomer peak was fit with a Gaussian distribution. Figure 7.2 plots the ionomer peak q-spacing for each equivalent weight and annealing temperature at ambient and humidified conditions. The black bar is the mean value for a sample, and each dot is the spacing at a given χ. The dot size is proportional to χ (χ goes from 0° through-plane to 90° in-plane, but sector cuts are taken from 0 to 70° to avoid the Yoneda peak), which helps illustrate the distribution in q-spacing. At ambient conditions (open circles), the ionomer peak is at a higher q-spacing through-plane that decreases as χ increases (for 3M 1000 EW and Nafion 1100 EW, the ionomer peak signal was not present above background for most ambient samples). With increasing annealing temperature, the distribution in q-spacing decreases and the average q-spacing value increases. Once the films are humidified (filled circles), q-spacing not only decreases (due to expansion of nano-domains), but their distribution also becomes narrower indicating a more uniform domain distribution. As water absorbs into the film, the confinement upon the silicon substrate prevents significant swelling in-plane and most swelling takes place

through-plane. The anisotropic swelling collapses the distribution in q-spacing to a smaller average value that reflects the higher water content at high RH.
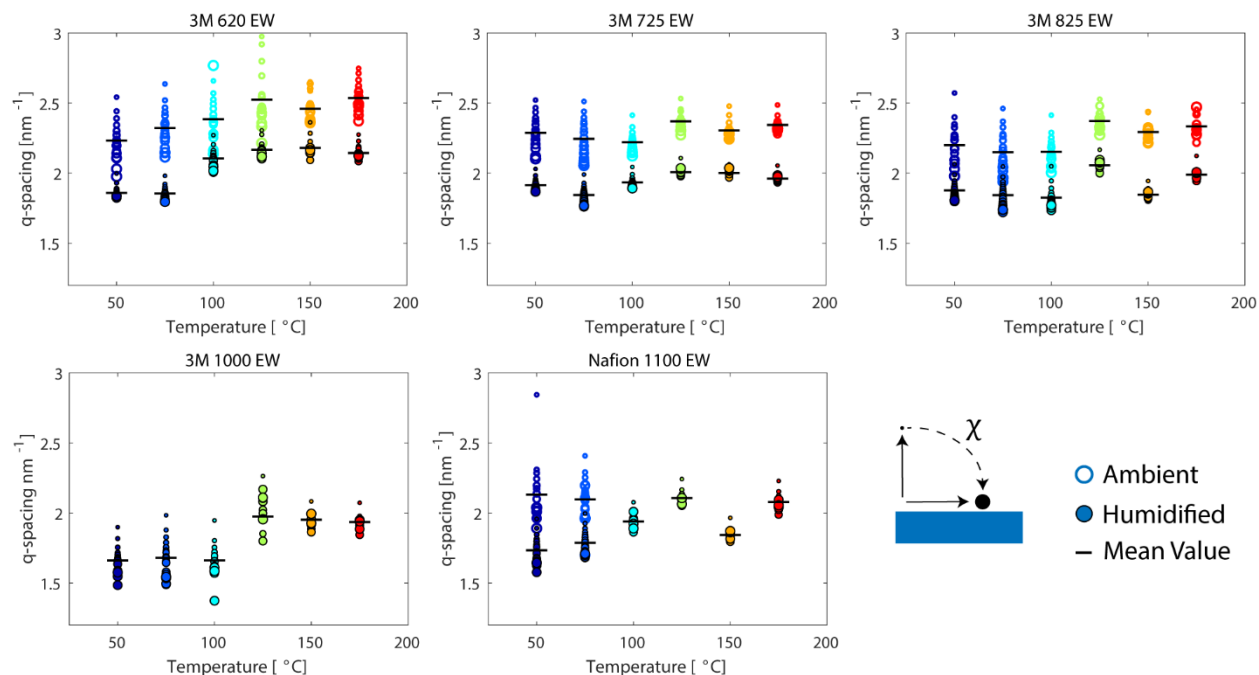
Figure 7.2. Distribution of ionomer peak spacing for ambient and humidified conditions. Circle size represents the azimuthal angle. Open circles are under ambient conditions, filled circles are under humidified (95+% RH) conditions.

In addition to the distribution in ionomer peak q-spacing, there is also a distribution in peak intensity and breadth. Figures S7.1-S7.5 in Supporting Information are the 2D GISAXS images, which show the anisotropy in intensity. Using the intensity and FWHM extracted from fitting, an orientation parameter (OP) can be calculated using Equation 7.1, which provides a numerical value for how oriented the ionomer domains. A value of ~0.48 represents isotropic ordering (represented as a dashed line) and as OP increases towards 1, the ionomer domain correlations become oriented through-plane. Figure 7.3 plots OP for each EW and annealing temperature, at ambient and humidified conditions. Below T_α, the OP values indicate the ionomer peak is more strongly correlated through-plane. The through-plane correlation is strongest (highest OP) in the sample annealed at 100°C for 3M 620 EW, and strongest in the samples annealed at 75°C for the other four ionomers. 3M 725 and 825 EW have a decrease in OP at 100°C, with a marked transition at 125°C when the matrix knee appears. T_α as measured by dynamic mechanical analysis in bulk membranes occurs over a finite width in temperature;[3] the decrease in OP at 100°C suggests a portion of the film has rearranged towards a more isotropic state. The film's rearrangement is more complete at 125°C, where OP has an isotropic value. 3M 1000 EW shows a more gradual transition towards isotropic values with annealing temperature and Nafion 1100 EW's transition occurs at 100°C. The longer side-chain in Nafion may confer greater mobility to the polymer and allow for rearrangement at a slightly lower temperature. These results indicate the maximum in OP precedes the onset of T_α.
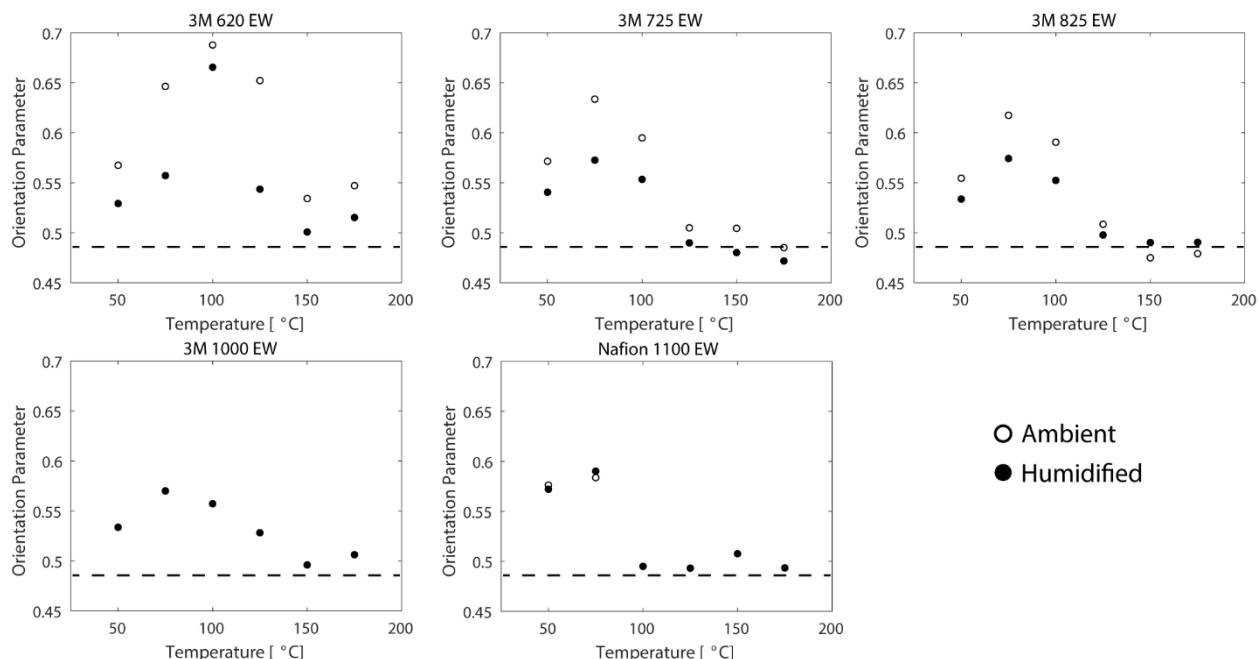
Figure 7.3. Orientation Parameter for ambient and humidified conditions. Dotted line represents an isotropic sample.

Upon swelling, the films' OP values decrease towards a more isotropic value. This decrease in OP with hydration is most pronounced in 3M 620 EW film, which uptakes the most water, and decreases with increasing EW. As the polymer volume fraction decreases, the hydrophilic domains become more interconnected and reduce the dry anisotropy. The interconnectivity of the domains is important for reactant transport (e.g. H^+, O_2, H_2O), and has implications for reducing transport resistances in catalyst layers. To understand how annealing temperature affects the water uptake in these materials, each films' thickness swelling was measured as a function of RH using ellipsometry.
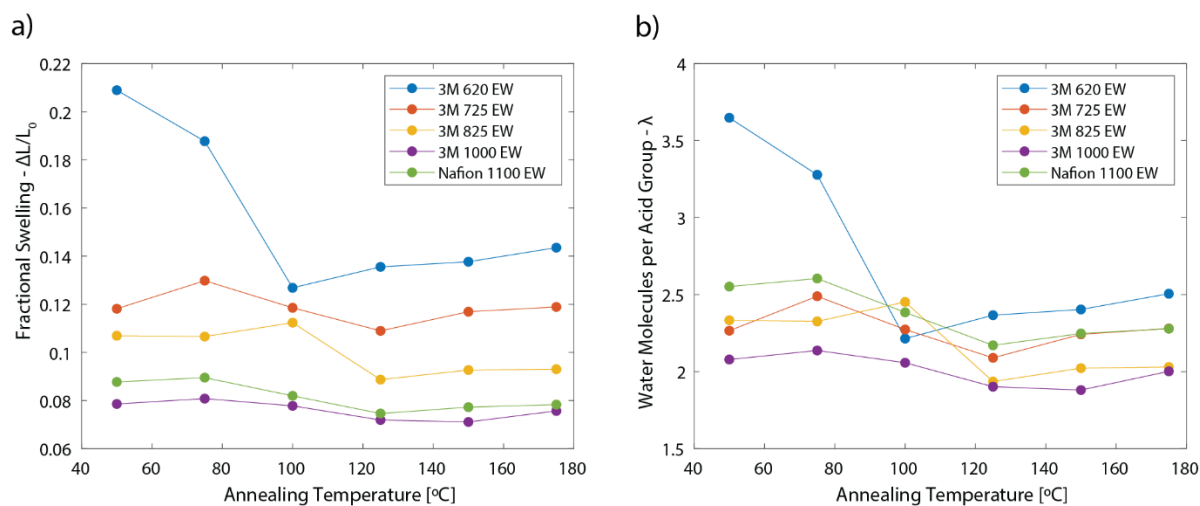
Figure 7.4. a) Fractional swelling plotted versus annealing temperature b) Normalized water content (λ), calculated from fractional swelling and equivalent weight, plotted versus annealing temperature.

81

Figure 7.4a plots the fractional swelling at 95% RH for each EW and annealing temperature. With increasing annealing temperature, the fractional swelling at 95% RH decreases for all EWs. As the EW increases, the side chain density decreases and there is a smaller total driving force for water sorption into the ionomer and the fractional swelling decreases accordingly. The driving force per sulfonic acid group remains the same and the total driving force can be normalized using the EW of each polymer. Plotting the number of water molecules per sulfonic acid group, λ, the curves collapse to follow a universal trend (Figure 7.4b). Calculating λ assumes purely 1-dimensional swelling, the same dry density, and ideal mixing. There are differences in Figure 7.4b that may be due to differences in initial density or non-ideal mixing, but the sorption behavior across these chemistries is more similar on a per acid-group basis. This same universal sorption behavior is observed in bulk membranes,[3] but the water content in these thin films is considerably depressed. Bulk membranes have λ values between 10 and 15 at 95% RH. Confinement affects the nanostructural morphology and prevents significant in-plane swelling.
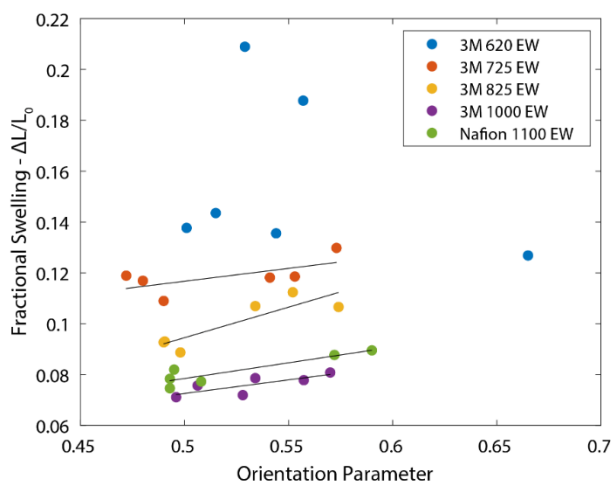
Figure 7.5. Fractional swelling plotted versus orientation parameter for each ionomer chemistry.

Between 75 and 125°C, there is a decrease in swelling, which corresponds to the appearance of the matrix knee and the shift in OP to more isotropic values. To connect the macroscopic swelling to the nanostructure, Figure 7.5 plots the swelling at 95% RH versus the humidified OP for each ionomer, which shows aa positive correlation, with the notable exception of the 3M 620 EW. 3M 620 EW has an additional scattering peak appear above Tα, and the two peaks follow a $\sqrt{3}, \sqrt{4}$ q-spacing. This is a new morphology distinct from the other ionomers and as such, it has a different relationship between orientation and swelling. For the other 3M EWs and Nafion, the greater the orientation through-plane, the higher the observed swelling. This demonstrates a connection between the nanostructural morphology and macroscopic swelling. For alternating layers of hydrophilic and hydrophobic regions through-plane, the hydrophilic regions are mainly prevented from swelling in-plane. As the morphology approaches an isotropic orientation, the film's through-plane swelling is reduced; Figure 7.6 demonstrates this schematically.
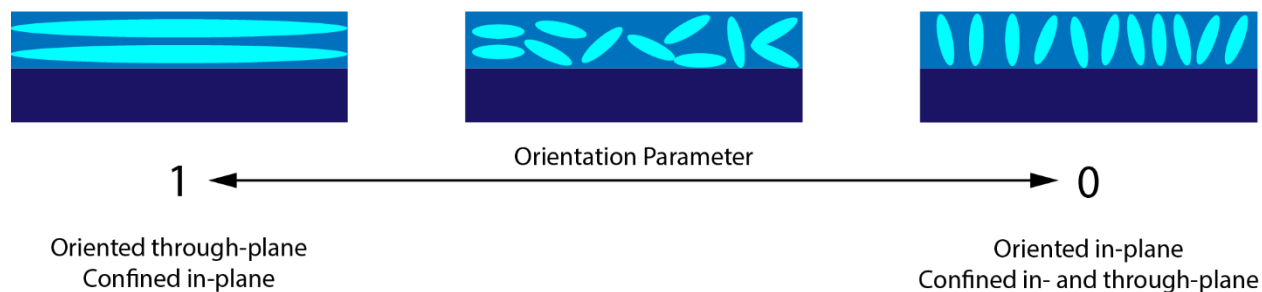
Figure 7.6. Schematic on the effect of domain orientation.

All thin films will be prevented from swelling in-plane due to confinement upon a substrate, while additional swelling restriction may occur due to the orientation of phase-separated domains. At the extreme of complete orientation through-plane (OP = 1), layers of hydrophilic and hydrophobic domains would alternate through-plane. Because of this alternating layout (i.e. lamellae), there would be no percolation of the structural hydrophobic phase through the film, which would allow stress-free swelling through-plane, and a greater water uptake at a given water activity. At the other extreme, the orientation of domain correlation would be completely in-plane (OP = 0) with perfect percolation of both phases from top to bottom of the film. In this scenario, the structural hydrophobic component would prevent the hydrophilic domains from swelling through-plane, in addition to the in-plane mechanical confinement from the substrate. This additional through-plane restriction will increase swelling stress and reduce overall water uptake. For PFSA ionomers studied here, the orientation lies much closer to isotropic and the effect is more subtle. The effect of orientation is not only important for water uptake, but also for reactant transport. The effect of tortuosity on transport has been demonstrated across a wide variety of systems including bulk PFSA membranes,[146-147] block co-polymer electrolytes,[148-149] and porous media.[94]

7.4   Summary and Outlook

The nanostructural morphology of 3M 620, 725, 825, 1000 and Nafion 1100 EW ionomers were probed with GISAXS at 6 different annealing conditions. Films were studied at ambient and humidified conditions to understand the effect of water uptake on morphology. The ionomer peak q-spacing has a large distribution at ambient conditions that collapses to a smaller q-value in the humidified condition and within each EW there is a positive trend in q-spacing with increasing annealing temperature for both environmental conditions. The appearance of the matrix knee, attributed to inter-crystallite spacing, appears above the alpha-transition (T_α) temperature as measured in bulk samples. Concurrent with the appearance of the matrix knee is a shift in the orientation of ionomer domain correlations; below T_α the ionomer domain correlations are stronger through-plane and above T_α the ionomer peak becomes more isotropic. The nanostructure is correlated to macroscopic swelling measurements using ellipsometry. Swelling decreases with increasing EW and increasing annealing temperature. For 3M 725, 825, 1000, and Nafion 1100 EW, there is a positive correlation between OP and swelling, which demonstrates the relationship of domain correlation orientation to observed physical properties. The next step in building these structure-property relationships is to connect the nanostructure to transport properties. Using the interdigitated electrodes described in Chapter 4, proton transport can be measured as a function of water content and connected to domain orientation. The swelling measurements from ellipsometry will normalize the polymer volume fraction to understand how domain orientation and tortuosity

83

are linked in these ionomer thin films. Quantifying this effect for PFSA thin films is crucial for understanding the limiting behavior in the catalyst layers of electrochemical energy conversion devices.

7.5   Supporting Information

Figures S7.1-S7.5 are the full 2D GISAXS images at the 6 annealing conditions for four 3M PFSA ionomer EWs (620, 725, 825, 1000 EW) and Nafion 1100 EW. The 2D GISAXS images visually show the anisotropy in the ionomer peak, which is quantified with OP in Figure 7.3.
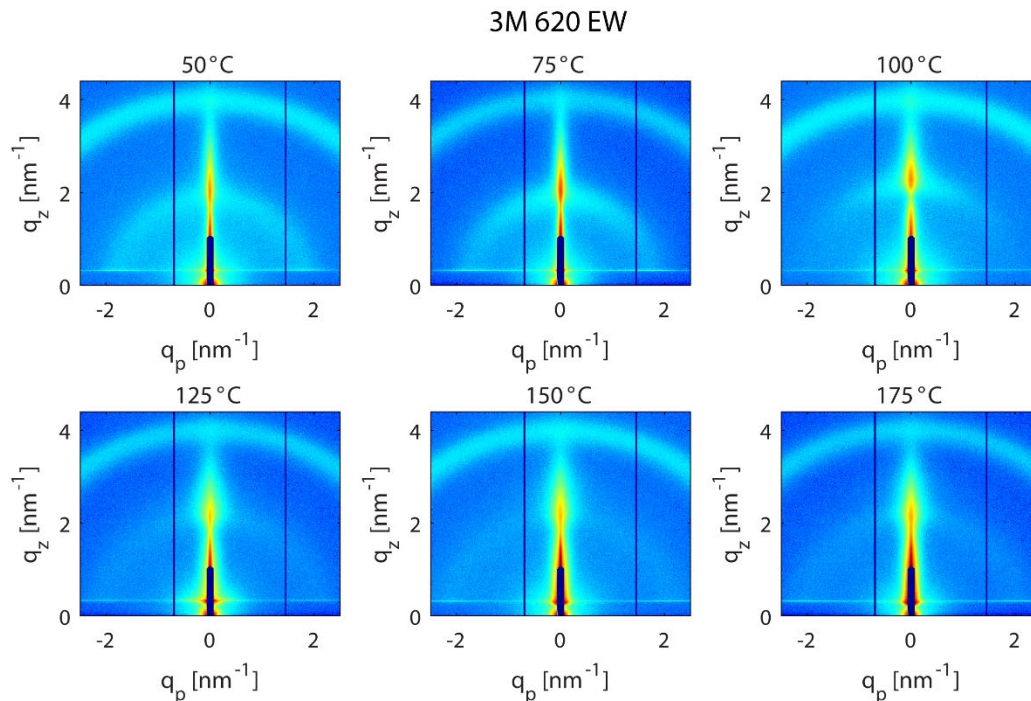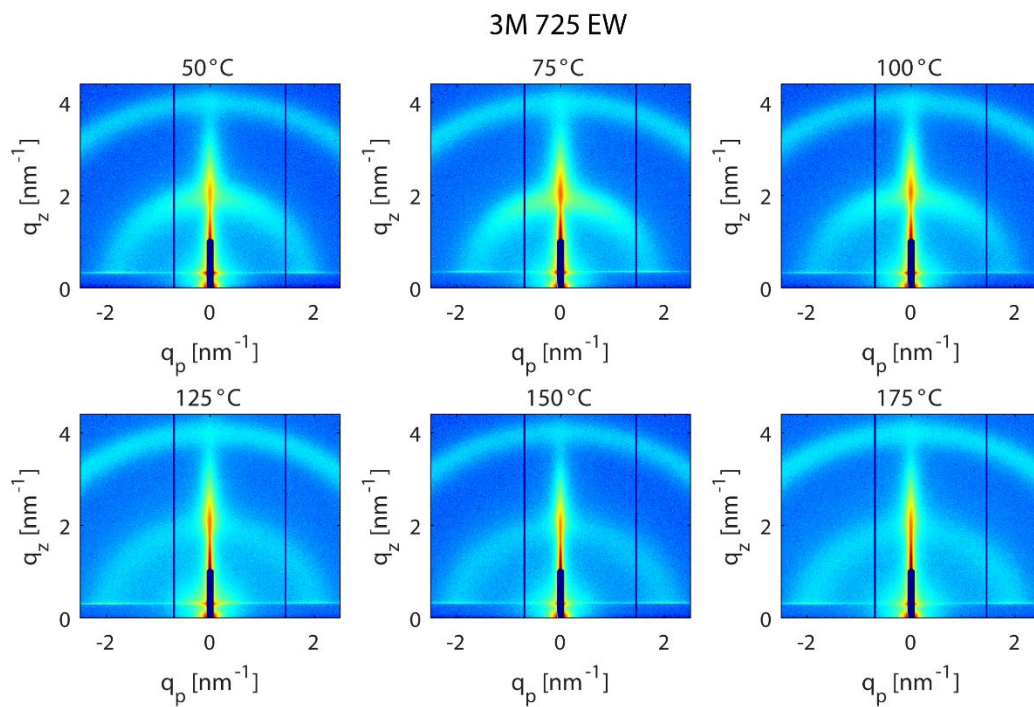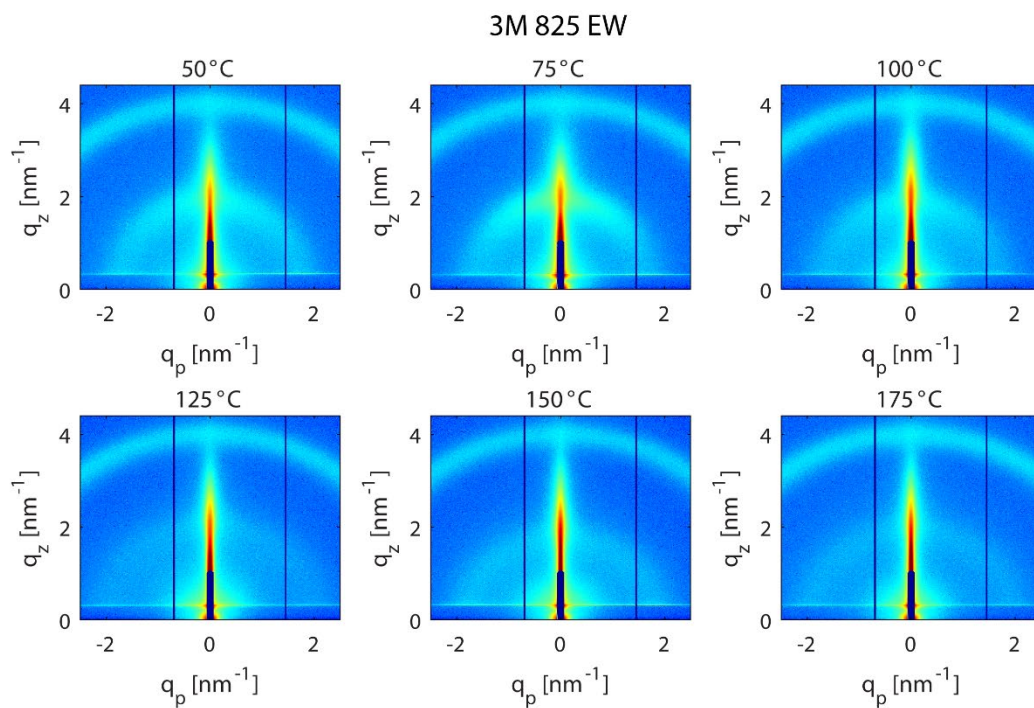

Figure S7.1. 3M 620 EW.

3M 725 EW

Figure S7.2. 3M 725 EW.

3M 825 EW

Figure S7.3. 3M 825 EW.

3M 1000 EW

Figure S7.4. 3M 1000 EW.

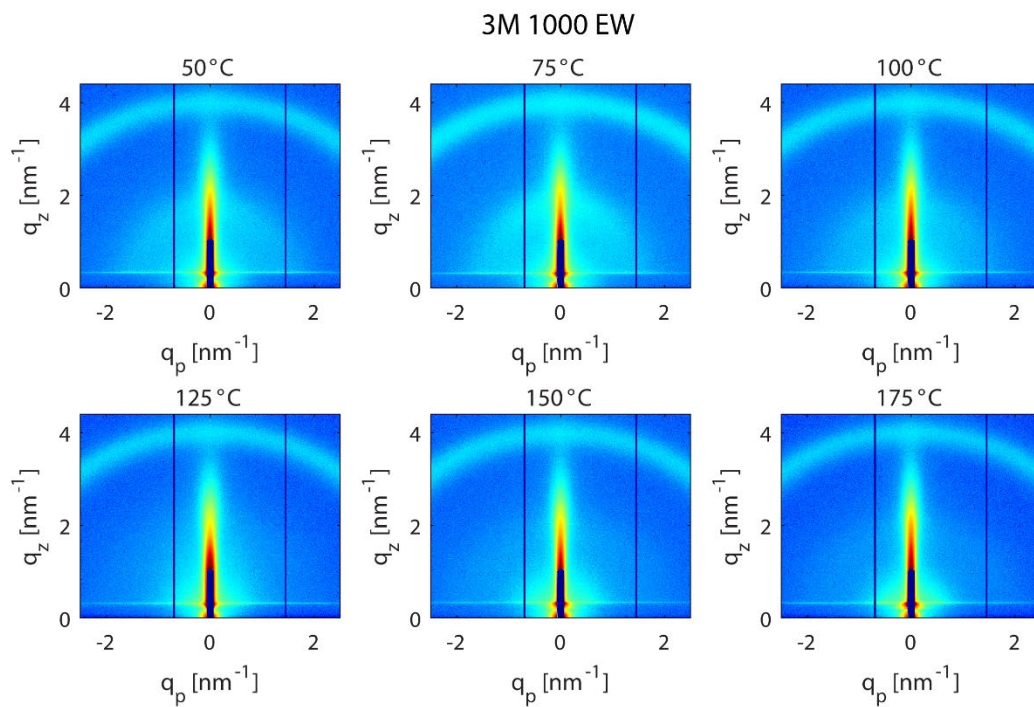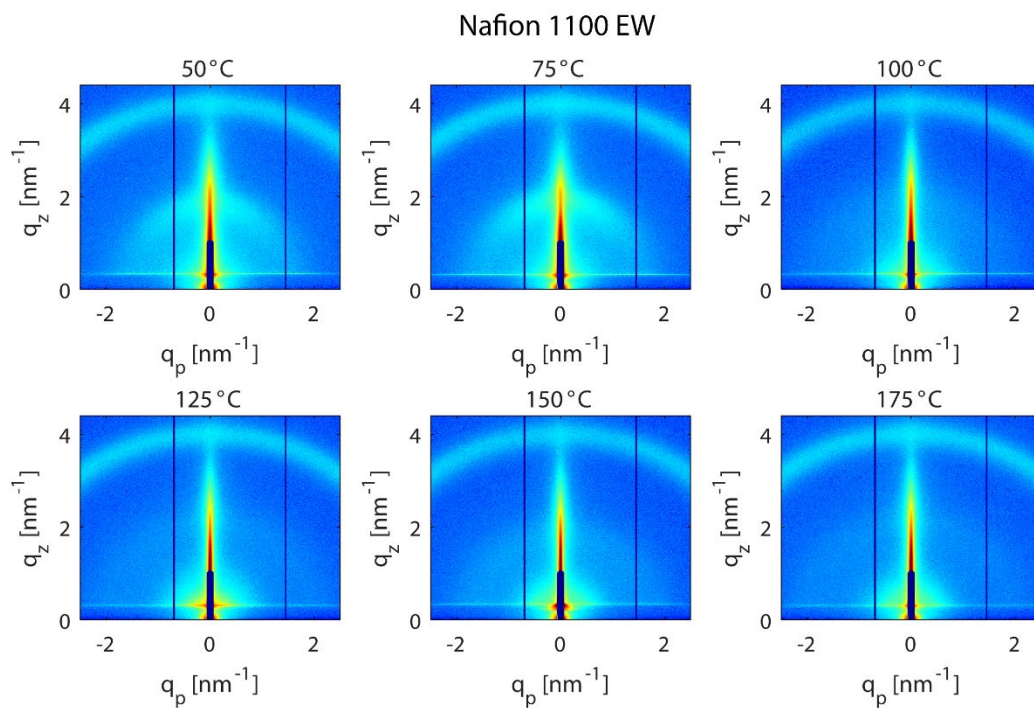Nafion 1100 EW

Figure S7.5. Nafion 1100 EW.

8 Summary

This dissertation develops and explores structure-property relationships in perfluorinated sulfonic-acid (PFSA) ion-conducting (ionomer) polymer thin films. In pursuit of this goal, experimental techniques were developed and applied to ionomer thin films. Chapter 2 gave a general background into transmission and grazing-incidence x-ray scattering (GIXS) before developing a new method of GIXS called electric-field intensity (EFI)-modulated scattering. By taking GIXS images across a range of incidence angles, the intensity modulation of the specular rod can be analyzed using EFI calculations to depth-resolve thin films. The technique is explained within the distorted-wave born approximation and validated with Nafion single layer films and Nafion-SBS bilayer films. The index of refraction, film thickness, and a depth-profile of scatterers can be extracted with this technique, which is typically not attainable in normal GIXS measurements and represents a new paradigm of characterizing condensed-matter thin films.

Chapter 3 focused on mechanical characterization using a cantilever bending method, which measures the stresses in supported thin films via the curvature of the underlying substrate. Polymer network theory is applied to a model hydrogel system to understand stresses away from the limit of zero deformation. The analysis shows that, in rubbery polymers, the cantilever bending method can be used to measure the osmotic pressure and equilibrium shear modulus. The chapter concludes with a discussion on applying the cantilever bending method to measure thermal transitions and mechanical properties as a function of temperature.

Since PFSA thin films exist in catalyst layers that undergo applied electrochemical potentials, it is desired to study these materials *operando*. Chapter 4 discussed standard nanofabrication techniques and applies them to manufacture planar electrode devices for *operando* characterization. These devices have a cell geometry that enables GIXS to be performed while applying working potentials to drive electrochemical reactions. The planar electrode cell was tested with a Nafion PFSA thin film and 3M perfluorinated anion exchange material (PFAEM). The phase-separated structure of the Nafion thin film did not appear to change with applied potentials, but there is preliminary evidence that the thin film's density is changing in a non-uniform way in response to the potential. Further experiments are proposed to elucidate the underlying behavior. The PFAEM thin film exhibited a change in morphology from lamellar to bicontinuous under applied potentials. Likely this change is occurring due to the conversion of the carbonate species to hydroxide during the experiment. Chapter 4 concluded with a discussion on interdigitated electrodes as a platform to interrogate the ion-transport behavior in ionomer thin films.

Chapter 5 looked at the formation of Nafion thin films as they are cast from dispersion. Grazing incidence small- and wide-angle x-ray scattering (GISAXS/GIWAXS) were employed with an *in-situ* slot die coater to investigate this dynamic behavior. Within the dispersion, Nafion aggregates exists as a core-shell rod, where the core is a dense PTFE aggregate and the shell is a mixture of solvated side-chain and solvent. As solvent evaporates, the aggregates arrange at a regular distance that is mediated by side-chain interactions. As the film transitions from a dispersion to gel-like state, crystallization of the backbone occurs rapidly. In the gel state, hydrophilic domains coalesce as solvent continues to evaporate. The entire process from dispersion to film occurs over 10 minutes, at which point normal drying behavior is observed. Casting from different water/n-propanol ratios is shown to affect the dynamic behavior observed during the drying process, which is a potential avenue for controlling the structure and behavior of ionomer thin films and catalyst layers.

Chapter 6 detailed how different annealing temperatures affect the nanostructural morphology and related physical properties. To do this, GIWAXS was used to determine the relative degree of crystallinity for Nafion thin films at three different annealing temperature and across a range of thicknesses. Contrary to conventional thought, the relative degree of crystallinity (rDoC) decreased with increasing annealing temperature. This behavior has been observed in other ion-conducting polymers, and is attributed to the melting of small imperfect crystallites. Crystallinity shows a non-monotonic trend with film thickness, first increasing to a maximum around 50 nm before sharply decreasing. Normalizing the change in rDoC across annealing temperatures, the effect of confinement is shown to be universal. The mechanical properties of Nafion thin films were investigated at the same annealing temperatures to understand the relationship between rDoC and modulus. A weak positive correlation exists, but these results highlight the multiscale ordering of PFSA ionomers. Mesoscale and network effects need to be taken in to account to connect crystallinity to mechanical properties more rigorously.

The final study looked at the structure and swelling behavior of Nafion and 3M PFSA at four different equivalent weights. Each of these chemistries were annealed from 50 to 175°C and their structure characterized using GISAXS. Below their α-transition temperature, the hydrophilic domains were oriented more strongly through-plane. Once the films were annealed above the α-transition temperature, these domains become isotropic through the film. Hydration reduces the anisotropy in orientation relative to the dry state. Water-uptake measurements were performed using spectroscopic ellipsometry and plotting the fractional swelling at 95% RH versus the orientation parameter for the ionomer peak demonstrated a positive correlation: the higher the domain orientation through-plane, the higher the swelling. A simple percolation argument explains this phenomenon.

In total, this work has not only advanced the understanding of PFSA thin films, but has also advanced the techniques and methods with which to investigate these materials. It is my hope that these techniques and methods will aid others in exploring and understanding condensed soft-matter thin film behavior.

References

1. Holdcroft, S., Fuel Cell Catalyst Layers: A Polymer Science Perspective. *Chem Mater* **2014,** *26* (1), 381-393.
2. Mauritz, K. A.; Moore, R. B., State of understanding of Nafion. *Chemical reviews* **2004,** *104* (10), 4535-4586.
3. Kusoglu, A.; Weber, A. Z., New Insights into Perfluorinated Sulfonic-Acid Ionomers. *Chemical Reviews* **2017,** *117* (3), 987-1104.
4. Eastman, S. A.; Kim, S.; Page, K. A.; Rowe, B. W.; Kang, S.; Soles, C. L.; Yager, K. G., Effect of Confinement on Structure, Water Solubility, and Water Transport in Nafion Thin Films. *Macromolecules* **2012,** *45* (19), 7920-7930.
5. Page, K. A.; Kusoglu, A.; Stafford, C. M.; Kim, S.; Kline, R. J.; Weber, A. Z., Confinement-driven increase in ionomer thin-film modulus. *Nano letters* **2014,** *14* (5), 2299-304.
6. Kusoglu, A.; Kushner, D.; Paul, D. K.; Karan, K.; Hickner, M. A.; Weber, A. Z., Impact of Substrate and Processing on Confinement of Nafion Thin Films. *Advanced Functional Materials* **2014,** *24* (30), 4763-4774.
7. Weber, A. Z.; Kusoglu, A., Unexplained transport resistances for low-loaded fuel-cell catalyst layers. *J. Mater. Chem. A* **2014,** *2* (41), 17207-17211.
8. Grot, W., *Fluorinated Ionomers*. William Andrew: 2011.
9. Allen, F. I.; Comolli, L. R.; Kusoglu, A.; Modestino, M. A.; Minor, A. M.; Weber, A. Z., Morphology of Hydrated As-Cast Nafion Revealed through Cryo Electron Tomography. *ACS Macro Letters* **2014,** *4* (1), 1-5.
10. Gebel, G.; Aldebert, P.; Pineri, M., Structure and related properties of solution-cast perfluorosulfonated ionomer films. *Macromolecules* **1987,** *20* (6), 1425-1428.
11. Shi, S.; Weber, A. Z.; Kusoglu, A., STRUCTURE-TRANSPORT RELATIONSHIP OF PERFLUOROSULFONIC-ACID MEMBRANES IN DIFFERENT CATIONIC FORMS. *Electrochimica Acta* **2016,** *220*, 517-528.
12. Modestino, M. A.; Paul, D. K.; Dishari, S.; Petrina, S. A.; Allen, F. I.; Hickner, M. A.; Karan, K.; Segalman, R. A.; Weber, A. Z., Self-Assembly and Transport Limitations in Confined Nafion Films. *Macromolecules* **2013,** *46* (3), 867-873.
13. DeCaluwe, S. C.; Baker, A. M.; Bhargava, P.; Fischer, J. E.; Dura, J. A., Structure-property relationships at Nafion thin-film interfaces: Thickness effects on hydration and anisotropic ion transport. *Nano Energy* **2018,** *46*, 91-100.
14. Dura, J. A.; Murthi, V. S.; Hartman, M.; Satija, S. K.; Majkrzak, C. F., Multilamellar Interface Structures in Nafion. *Macromolecules* **2009,** *42* (13), 4769-4774.
15. Murthi, V. S.; Dura, J.; Satija, S.; Majkrzak, C., Water Uptake and Interfacial Structural Changes of Thin Film Nafion® Membranes Measured by Neutron Reflectivity for PEM Fuel Cells. *ECS Transactions* **2008,** *16* (2), 1471-1485.
16. Forrest, J. A.; Dalnoki-Veress, K., The glass transition in thin polymer films. *Advances in Colloid and Interface Science* **2001,** *94* (1–3), 167-195.
17. Mataz, A.; Gregory, B. M., Effects of confinement on material behaviour at the nanometre size scale. *Journal of Physics: Condensed Matter* **2005,** *17* (15), R461.
18. Liu, Y.-X.; Chen, E.-Q., Polymer crystallization of ultrathin films on solid substrates. *Coordination Chemistry Reviews* **2010,** *254* (9–10), 1011-1037.

19. Wang, Y.; Ge, S.; Rafailovich, M.; Sokolov, J.; Zou, Y.; Ade, H.; Lüning, J.; Lustiger, A.; Maron, G., Crystallization in the Thin and Ultrathin Films of Poly(ethylene−vinyl acetate) and Linear Low-Density Polyethylene. *Macromolecules* **2004,** *37* (9), 3319-3327.

20. Tsui, O. K. C.; Russell, T. P.; Hawker, C. J., Effect of Interfacial Interactions on the Glass Transition of Polymer Thin Films. *Macromolecules* **2001,** *34* (16), 5535-5539.

21. Page, K. A.; Cable, K. M.; Moore, R. B., Molecular Origins of the Thermal Transitions and Dynamic Mechanical Relaxations in Perfluorosulfonate Ionomers. *Macromolecules* **2005,** *38* (15), 6472-6484.

22. Abe, Y.; Mochizuki, A.; Kawashima, T.; Yamashita, S.; Asaka, K.; Oguro, K., Effect on bending behavior of counter cation species in perfluorinated sulfonate membrane–platinum composite. *Polymers for Advanced Technologies* **1998,** *9* (8), 520-526.

23. Shahinpoor, M., Ionic polymer–conductor composites as biomimetic sensors, robotic actuators and artificial muscles—a review. *Electrochimica Acta* **2003,** *48* (14–16), 2343-2353.

24. Kendrick, I.; Kumari, D.; Yakaboski, A.; Dimakis, N.; Smotkin, E. S., Elucidating the Ionomer-Electrified Metal Interface. *Journal of the American Chemical Society* **2010,** *132* (49), 17611-17616.

25. Subbaraman, R.; Strmcnik, D.; Stamenkovic, V.; Markovic, N. M., Three Phase Interfaces at Electrified Metal−Solid Electrolyte Systems 1. Study of the Pt(hkl)−Nafion Interface. *The Journal of Physical Chemistry C* **2010,** *114* (18), 8414-8422.

26. Als-Nielsen, J.; McMorrow, D., *Elements of modern X-ray physics*. John Wiley & Sons: 2011.

27. Roe, R.-J., *Methods of X-ray and Neutron Scattering in Polymer Science*. Oxford University Press: 2000.

28. Baker, J. L.; Jimison, L. H.; Mannsfeld, S.; Volkman, S.; Yin, S.; Subramanian, V.; Salleo, A.; Alivisatos, A. P.; Toney, M. F., Quantification of Thin Film Crystallographic Orientation Using X-ray Diffraction with an Area Detector. *Langmuir* **2010,** *26* (11), 9146-9151.

29. Smilgies, D.-M., Geometry-independent intensity correction factors for grazing-incidence diffraction. *Review of Scientific Instruments* **2002,** *73* (4), 1706-1710.

30. Renaud, G.; Lazzari, R.; Leroy, F., Probing surface and interface morphology with Grazing Incidence Small Angle X-Ray Scattering. *Surface Science Reports* **2009,** *64* (8), 255-380.

31. Vineyard, G. H., Grazing-incidence diffraction and the distorted-wave approximation for the study of surfaces. *Physical Review B* **1982,** *26* (8), 4146-4159.

32. Sinha, S. K.; Sirota, E. B.; Garoff, S.; Stanley, H. B., X-ray and neutron scattering from rough surfaces. *Physical Review B* **1988,** *38* (4), 2297-2311.

33. Rauscher, M.; Salditt, T.; Spohn, H., Small-angle x-ray scattering under grazing incidence: The cross section in the distorted-wave Born approximation. *Physical Review B* **1995,** *52* (23), 16855-16863.

34. Lazzari, R.; Leroy, F.; Renaud, G., Grazing-incidence small-angle x-ray scattering from dense packing of islands on surfaces: Development of distorted wave Born approximation and correlation between particle sizes and spacing. *Physical Review B* **2007,** *76* (12), 125411.

35. Jiang, Z.; Lee, D. R.; Narayanan, S.; Wang, J.; Sinha, S. K., Waveguide-enhanced grazing-incidence small-angle x-ray scattering of buried nanostructures in thin films. *Physical Review B* **2011,** *84* (7), 075440.

36. Holy´, V.; Kuběna, J.; Ohli´dal, I.; Lischka, K.; Plotz, W., X-ray reflection from rough layered systems. *Physical Review B* **1993,** *47* (23), 15896-15903.

37. Holý, V.; Baumbach, T., Nonspecular x-ray reflection from rough multilayers. *Physical Review B* **1994,** *49* (15), 10668-10676.

38. Parratt, L. G., Surface Studies of Solids by Total Reflection of X-Rays. *Physical Review* **1954,** *95* (2), 359-369.

39. Tolan, M., X-ray scattering from soft-matter thin films: materials science and basic research. **1999**.

40. Golovchenko, J. A.; Patel, J. R.; Kaplan, D. R.; Cowan, P. L.; Bedzyk, M. J., Solution to the Surface Registration Problem Using X-Ray Standing Waves. *Physical Review Letters* **1982,** *49* (8), 560-563.

41. Bedzyk, M. J.; Bommarito, G. M.; Schildkraut, J. S., X-ray standing waves at a reflecting mirror surface. *Physical Review Letters* **1989,** *62* (12), 1376-1379.

42. Bedzyk, M. J.; Bommarito, G. M.; Caffrey, M.; Penner, T. L., Diffuse-double layer at a membrane-aqueous interface measured with x-ray standing waves. *Science* **1990,** *248* (4951), 52.

43. Lee, D. R.; Hagman, A.; Li, X.; Narayanan, S.; Wang, J.; Shull, K. R., Perturbation to the resonance modes by gold nanoparticles in a thin-film-based x-ray waveguide. *Applied Physics Letters* **2006,** *88* (15), 153101.

44. Babonneau, D.; Camelio, S.; Lantiat, D.; Simonot, L.; Michel, A., Waveguiding and correlated roughness effects in layered nanocomposite thin films studied by grazing-incidence small-angle x-ray scattering. *Physical Review B* **2009,** *80* (15), 155446.

45. Lee, B.; Lo, C.-T.; Thiyagarajan, P.; Lee, D. R.; Niu, Z.; Wang, Q., Structural characterization using the multiple scattering effects in grazing-incidence small-angle X-ray scattering. *Journal of Applied Crystallography* **2008,** *41* (1), 134-142.

46. Narayanan, S.; Lee, D. R.; Guico, R. S.; Sinha, S. K.; Wang, J., Real-Time Evolution of the Distribution of Nanoparticles in an Ultrathin-Polymer-Film-Based Waveguide. *Physical Review Letters* **2005,** *94* (14), 145504.

47. Gann, E.; Caironi, M.; Noh, Y.-Y.; Kim, Y.-H.; McNeill, C. R., Diffractive X-ray Waveguiding Reveals Orthogonal Crystalline Stratification in Conjugated Polymer Thin Films. *Macromolecules* **2018,** *51* (8), 2979-2987.

48. Alexander, H.; Wim, B.; James, G.; Eric, S.; Eliot, G.; Rick, K.; Alastair, M.; Matthew, C.; Bruce, R.; Howard, P., A SAXS/WAXS/GISAXS Beamline with Multilayer Monochromator. *Journal of Physics: Conference Series* **2010,** *247* (1), 012007.

49. Henke, B. L.; Gullikson, E. M.; Davis, J. C., X-Ray Interactions: Photoabsorption, Scattering, Transmission, and Reflection at E = 50-30,000 eV, Z = 1-92. *Atomic Data and Nuclear Data Tables* **1993,** *54* (2), 181-342.

50. Virtanen, P.; Gommers, R.; Oliphant, T. E.; Haberland, M.; Reddy, T.; Cournapeau, D.; Burovski, E.; Peterson, P.; Weckesser, W.; Bright, J.; van der Walt, S. J.; Brett, M.; Wilson, J.; Millman, K. J.; Mayorov, N.; Nelson, A. R. J.; Jones, E.; Kern, R.; Larson, E.; Carey, C. J.; Polat, İ.; Feng, Y.; Moore, E. W.; VanderPlas, J.; Laxalde, D.; Perktold, J.; Cimrman, R.; Henriksen, I.; Quintero, E. A.; Harris, C. R.; Archibald, A. M.; Ribeiro, A. H.; Pedregosa, F.; van Mulbregt, P.; Vijaykumar, A.; Bardelli, A. P.; Rothberg, A.; Hilboll, A.; Kloeckner, A.; Scopatz, A.; Lee, A.; Rokem, A.; Woods, C. N.; Fulton, C.; Masson, C.; Häggström, C.; Fitzgerald, C.; Nicholson, D. A.; Hagen, D. R.; Pasechnik, D. V.; Olivetti, E.; Martin, E.; Wieser, E.; Silva, F.; Lenders, F.; Wilhelm, F.; Young, G.; Price,

G. A.; Ingold, G.-L.; Allen, G. E.; Lee, G. R.; Audren, H.; Probst, I.; Dietrich, J. P.; Silterra, J.; Webber, J. T.; Slavič, J.; Nothman, J.; Buchner, J.; Kulick, J.; Schönberger, J. L.; de Miranda Cardoso, J. V.; Reimer, J.; Harrington, J.; Rodríguez, J. L. C.; Nunez-Iglesias, J.; Kuczynski, J.; Tritz, K.; Thoma, M.; Newville, M.; Kümmerer, M.; Bolingbroke, M.; Tartre, M.; Pak, M.; Smith, N. J.; Nowaczyk, N.; Shebanov, N.; Pavlyk, O.; Brodtkorb, P. A.; Lee, P.; McGibbon, R. T.; Feldbauer, R.; Lewis, S.; Tygier, S.; Sievert, S.; Vigna, S.; Peterson, S.; More, S.; Pudlik, T.; Oshima, T.; Pingel, T. J.; Robitaille, T. P.; Spura, T.; Jones, T. R.; Cera, T.; Leslie, T.; Zito, T.; Krauss, T.; Upadhyay, U.; Halchenko, Y. O.; Vázquez-Baeza, Y.; SciPy, C., SciPy 1.0: fundamental algorithms for scientific computing in Python. *Nature Methods* **2020**.

51. VanLandingham, M. R.; Villarrubia, J. S.; Guthrie, W. F.; Meyers, G. F. In *Nanoindentation of polymers: an overview*, Macromolecular symposia, Wiley-Blackwell, 111 River Street Hoboken NJ 07030-5774 USA: 2001; pp 15-44.

52. Stafford, C. M.; Harrison, C.; Beers, K. L.; Karim, A.; Amis, E. J.; VanLandingham, M. R.; Kim, H.-C.; Volksen, W.; Miller, R. D.; Simonyi, E. E., A buckling-based metrology for measuring the elastic moduli of polymeric thin films. *Nat Mater* **2004,** *3* (8), 545-550.

53. Stoney, G. G., The Tension of Metallic Films Deposited by Electrolysis. *Proceedings of the Royal Society of London. Series A* **1909,** *82* (553), 172-175.

54. Windischmann, H.; Gray, K. J., Stress measurement of CVD diamond films. *Diamond and Related Materials* **1995,** *4* (5), 837-842.

55. Hodge, T. C.; Bidstrup-Allen, S. A.; Kohl, P. A., Stresses in thin film metallization. *IEEE Transactions on Components, Packaging, and Manufacturing Technology: Part A* **1997,** *20* (2), 241-250.

56. Sethuraman, V. A.; Chon, M. J.; Shimshak, M.; Srinivasan, V.; Guduru, P. R., In situ measurements of stress evolution in silicon thin films during electrochemical lithiation and delithiation. *Journal of Power Sources* **2010,** *195* (15), 5062-5066.

57. Láng, G. G.; Seo, M., On the electrochemical applications of the bending beam method. *Journal of Electroanalytical Chemistry* **2000,** *490* (1–2), 98-101.

58. Chason, E.; Engwall, A.; Pei, F.; Lafouresse, M.; Bertocci, U.; Stafford, G.; Murphy, J. A.; Lenihan, C.; Buckley, D. N., Understanding Residual Stress in Electrodeposited Cu Thin Films. *Journal of The Electrochemical Society* **2013,** *160* (12), D3285-D3289.

59. Ramani, K.; Zhao, W., The evolution of residual stresses in thermoplastic bonding to metals. *International Journal of Adhesion and Adhesives* **1997,** *17* (4), 353-357.

60. Page, K. A.; Shin, J. W.; Eastman, S. A.; Rowe, B. W.; Kim, S.; Kusoglu, A.; Yager, K. G.; Stafford, G. R., In Situ Method for Measuring the Mechanical Properties of Nafion Thin Films during Hydration Cycles. *ACS Applied Materials & Interfaces* **2015,** *7* (32), 17874-17883.

61. Frieberg, B. R.; Page, K. A.; Graybill, J. R.; Walker, M. L.; Stafford, C. M.; Stafford, G. R.; Soles, C. L., Mechanical Response of Thermally Annealed Nafion Thin Films. *ACS Applied Materials & Interfaces* **2016,** *8* (48), 33240-33249.

62. Flory, P. J.; Jr., J. R., Statistical Mechanics of Cross-Linked Polymer Networks II. Swelling. *The Journal of Chemical Physics* **1943,** *11* (11), 521-526.

63. Kusoglu, A.; Karlsson, A. M.; Santare, M. H., Structure-property relationship in ionomer membranes. *Polymer* **2010,** *51* (6), 1457-1464.

64. Kusoglu, A.; Santare, M. H.; Karlsson, A. M., Mechanics-based model for non-affine swelling in perfluorosulfonic acid (PFSA) membranes. *Polymer* **2009,** *50* (11), 2481-2491.

65. Kusoglu, A.; Weber, A. Z., Water Transport and Sorption in Nafion Membrane. **2012,** *1096*, 175-199.

66. Kang, M. K.; Huang, R., A Variational Approach and Finite Element Implementation for Swelling of Polymeric Hydrogels Under Geometric Constraints. *Journal of Applied Mechanics* **2010,** *77* (6), 061004-061004-12.

67. Li, M.; Bresson, B.; Cousin, F.; Fretigny, C.; Tran, Y., Submicrometric Films of Surface-Attached Polymer Network with Temperature-Responsive Properties. *Langmuir* **2015,** *31* (42), 11516-11524.

68. Rubinstein, M.; Colby, R. H.; Dobrynin, A. V.; Joanny, J.-F., Elastic Modulus and Equilibrium Swelling of Polyelectrolyte Gels. *Macromolecules* **1996,** *29* (1), 398-406.

69. Quesada-Pérez, M.; Maroto-Centeno, J. A.; Forcada, J.; Hidalgo-Alvarez, R., Gel swelling theories: the classical formalism and recent approaches. *Soft Matter* **2011,** *7* (22), 10536-10547.

70. Safronov, A. P.; Adamova, L. V.; Blokhina, A. S.; Kamalov, I. A.; Shabadrov, P. A., Flory-Huggins parameters for weakly crosslinked hydrogels of poly(acrylic acid) and poly(methacrylic acid) with various degrees of ionization. *Polymer Science Series A* **2015,** *57* (1), 33-42.

71. Yeo, S. C.; Eisenberg, A., Physical properties and supermolecular structure of perfluorinated ion-containing (nafion) polymers. *Journal of Applied Polymer Science* **1977,** *21* (4), 875-898.

72. Osborn, S. J.; Hassan, M. K.; Divoux, G. M.; Rhoades, D. W.; Mauritz, K. A.; Moore, R. B., Glass Transition Temperature of Perfluorosulfonic Acid Ionomers. *Macromolecules* **2007,** *40* (10), 3886-3890.

73. Tesfaye, M.; Kushner, D. I.; McCloskey, B. D.; Weber, A. Z.; Kusoglu, A., Thermal Transitions in Perfluorosulfonated Ionomer Thin-Films. *ACS Macro Letters* **2018,** *7* (10), 1237-1242.

74. Satterfield, M. B.; Benziger, J. B., Viscoelastic properties of Nafion at elevated temperature and humidity. *Journal of Polymer Science Part B: Polymer Physics* **2009,** *47* (1), 11-24.

75. Hirotsu, S.; Hirokawa, Y.; Tanaka, T., Volume-phase transitions of ionized N-isopropylacrylamide gels. *The Journal of Chemical Physics* **1987,** *87* (2), 1392-1395.

76. Hooper, H. H.; Baker, J. P.; Blanch, H. W.; Prausnitz, J. M., Swelling equilibria for positively ionized polyacrylamide hydrogels. *Macromolecules* **1990,** *23* (4), 1096-1104.

77. Vidyasagar, A.; Majewski, J.; Toomey, R., Temperature Induced Volume-Phase Transitions in Surface-Tethered Poly(N-isopropylacrylamide) Networks. *Macromolecules* **2008,** *41* (3), 919-924.

78. Çaykara, T.; Kiper, S.; Demirel, G., Network parameters and volume phase transition behavior of poly(N-isopropylacrylamide) hydrogels. *Journal of Applied Polymer Science* **2006,** *101* (3), 1756-1762.

79. Contreras-Cáceres, R.; Schellkopf, L.; Fernández-López, C.; Pastoriza-Santos, I.; Pérez-Juste, J.; Stamm, M., Effect of the Cross-Linking Density on the Thermoresponsive Behavior of Hollow PNIPAM Microgels. *Langmuir* **2015,** *31* (3), 1142-1149.

80. Zhu, P. W.; Napper, D. H., Volume phase transitions of poly(N-isopropylacrylamide) latex particles in mixed water-N,N-dimethylformamide solutions. *Chemical Physics Letters* **1996,** *256* (1), 51-56.

81. Deal, B. E.; Grove, A. S., General Relationship for the Thermal Oxidation of Silicon. *Journal of Applied Physics* **1965,** *36* (12), 3770-3778.

82. DeCaluwe, S. C.; Kienzle, P. A.; Bhargava, P.; Baker, A. M.; Dura, J. A., Phase segregation of sulfonate groups in Nafion interface lamellae, quantified via neutron reflectometry fitting techniques for multi-layered structures. *Soft Matter* **2014,** *10* (31), 5763-5776.

83. Divekar, A. G.; Park, A. M.; Owczarczyk, Z. R.; Seifert, S.; Pivovar, B. S.; Herring, A. M., A Study of Carbonate Formation Kinetics and Morphological Effects Observed on OH-Form of Pfaem When Exposed to Air Containing CO2. *ECS Transactions* **2017,** *80* (8), 1005-1011.

84. Siroma, Z.; Watanabe, S.; Yasuda, K.; Fukuta, K.; Yanagi, H., Mathematical Modeling of the Concentration Profile of Carbonate Ions in an Anion Exchange Membrane Fuel Cell. *Journal of The Electrochemical Society* **2011,** *158* (6), B682.

85. Ziv, N.; Mondal, A. N.; Weissbach, T.; Holdcroft, S.; Dekel, D. R., Effect of CO2 on the properties of anion exchange membranes for fuel cell applications. *Journal of Membrane Science* **2019,** *586*, 140-150.

86. Niwa, O.; Morita, M.; Tabei, H., Electrochemical behavior of reversible redox species at interdigitated array electrodes with different geometries: consideration of redox cycling and collection efficiency. *Analytical Chemistry* **1990,** *62* (5), 447-452.

87. Kitsara, M.; Goustouridis, D.; Chatzandroulis, S.; Chatzichristidi, M.; Raptis, I.; Ganetsos, T.; Igreja, R.; Dias, C. J., Single chip interdigitated electrode capacitive chemical sensor arrays. *Sensors and Actuators B: Chemical* **2007,** *127* (1), 186-192.

88. Mazlan, N. S.; Ramli, M. M.; Abdullah, M. M. A. B.; Halin, D. S. C.; Isa, S. S. M.; Talip, L. F. A.; Danial, N. S.; Murad, S. A. Z., Interdigitated electrodes as impedance and capacitance biosensors: A review. *AIP Conference Proceedings* **2017,** *1885* (1), 020276.

89. Ronkainen, N. J.; Halsall, H. B.; Heineman, W. R., Electrochemical biosensors. *Chemical Society Reviews* **2010,** *39* (5), 1747-1763.

90. Mina, S.; Derek, R. O., Fabrication of an interdigitated sample holder for dielectric spectroscopy of thin films. *Journal of Physics: Conference Series* **2015,** *619* (1), 012028.

91. Ono, Y.; Nagao, Y., Interfacial Structure and Proton Conductivity of Nafion at the Pt-Deposited Surface. *Langmuir* **2016,** *32* (1), 352-358.

92. Sharon, D.; Bennington, P.; Liu, C.; Kambe, Y.; Dong, B. X.; Burnett, V. F.; Dolejsi, M.; Grocke, G.; Patel, S. N.; Nealey, P. F., Interrogation of Electrochemical Properties of Polymer Electrolyte Thin Films with Interdigitated Electrodes. *Journal of The Electrochemical Society* **2018,** *165* (16), H1028-H1039.

93. Olthuis, W.; Streekstra, W.; Bergveld, P., Theoretical and experimental determination of cell constants of planar-interdigitated electrolyte conductivity sensors. *Sensors and Actuators B: Chemical* **1995,** *24* (1), 252-256.

94. Dullien, F. A. L., *Porous Media: Fluid Transport and Pore Structure*. 2nd ed.; Academic Press: 1992.

95. Newman, J.; Thomas-Alyea, K. E., *Electrochemical Systems*. 3rd ed.; John Wiley & Sons, Inc.: 2004.

96. Kusoglu, A., Ionomer Thin Films in PEM Fuel Cells. In *Encyclopedia of Sustainability Science and Technology*, Meyers, R. A., Ed. Springer New York: New York, NY, 2018; pp 1-23.

97. Hatzell, K. B.; Dixit, M. B.; Berlinger, S. A.; Weber, A. Z., Understanding inks for porous-electrode formation. *J Mater Chem A* **2017,** *5* (39), 20527-20533.

98. Karan, K., PEFC catalyst layer: Recent advances in materials, microstructural characterization, and modeling. *Current Opinion in Electrochemistry* **2017,** *5* (1), 27-35.

99.   Welch, C.; Labouriau, A.; Hjelm, R.; Orler, B.; Johnston, C.; Kim, Y. S., Nafion in Dilute Solvent Systems: Dispersion or Solution? *ACS Macro Letters* **2012,** *1* (12), 1403-1407.

100.   Shibayama, M.; Matsunaga, T.; Kusano, T.; Amemiya, K.; Kobayashi, N.; Yoshida, T., SANS Studies on Catalyst Ink of Fuel Cell. *J Appl Polym Sci* **2014,** *131* (3), 39842.

101.   Yamaguchi, M.; Matsunaga, T.; Amemiya, K.; Ohira, A.; Hasegawa, N.; Shinohara, K.; Ando, M.; Yoshida, T., Dispersion of Rod-like Particles of Nafion in Salt-Free Water/1-Propanol and Water/Ethanol Solutions. *J Phys Chem B* **2014,** *118* (51), 14922-8.

102.   Kim, Y. S.; Welch, C. F.; Hjelm, R. P.; Mack, N. H.; Labouriau, A.; Orler, E. B., Origin of Toughness in Dispersion-Cast Nafion Membranes. *Macromolecules* **2015,** *48* (7), 2161-2172.

103.   Konosu, Y.; Masunaga, H.; Hikima, T.; Tokita, M.; Matsumoto, H.; Sasabe, T.; Yoshida, T.; Shinohara, K.; Hirai, S., Time-Resolved Nanostructural Analysis of Thin-Film Formation Process from Nafion Solution by Synchrotron X-Ray Scattering. *ECS Transactions* **2016,** *75* (14), 637-642.

104.   Konosu, Y.; Koga, M.; Matsumoto, H.; Tokita, M.; Masunaga, H.; Hikima, T.; Sugimori, H.; Yoshida, T.; Shinohara, K.; Hirai, S., Time-Resolved Nanostructural Analysis of Catalyst Layer Formation Process by Synchrotron X-ray Scattering. *ECS Transactions* **2017,** *80* (8), 269-273.

105.   Liu, F.; Ferdous, S.; Schaible, E.; Hexemer, A.; Church, M.; Ding, X.; Wang, C.; Russell, T. P., Fast Printing and In Situ Morphology Observation of Organic Photovoltaics Using Slot-Die Coating. *Advanced Materials* **2015,** *27* (5), 886-891.

106.   Pröller, S.; Liu, F.; Zhu, C.; Wang, C.; Russell, T. P.; Hexemer, A.; Müller-Buschbaum, P.; Herzig, E. M., Following the Morphology Formation In Situ in Printed Active Layers for Organic Solar Cells. *Advanced Energy Materials* **2016,** *6* (1), 1501580.

107.   M., P. C.; Feng, L.; P., R. T.; Alexander, H.; Cheng, W.; Peter, M. B., The Crystallization of PEDOT:PSS Polymeric Electrodes Probed In Situ during Printing. *Advanced Materials* **2015,** *27* (22), 3391-3397.

108.   Manley, E. F.; Strzalka, J.; Fauvell, T. J.; Jackson, N. E.; Leonardi, M. J.; Eastham, N. D.; Marks, T. J.; Chen, L. X., In Situ GIWAXS Analysis of Solvent and Additive Effects on PTB7 Thin Film Microstructure Evolution during Spin Coating. *Adv Mater* **2017,** *29* (43), 1703933.

109.   Chou, K. W.; Yan, B.; Li, R.; Li, E. Q.; Zhao, K.; Anjum, D. H.; Alvarez, S.; Gassaway, R.; Biocca, A.; Thoroddsen, S. T.; Hexemer, A.; Amassian, A., Spin-Cast Bulk Heterojunction Solar Cells: A Dynamical Investigation. *Advanced Materials* **2013,** *25* (13), 1923-1929.

110.   Al-Hussein, M.; Herzig, E. M.; Schindler, M.; Löhrer, F.; Palumbiny, C. M.; Wang, W.; Roth, S. V.; Müller-Buschbaum, P., Comparative study of the nanomorphology of spray and spin coated PTB7 polymer: Fullerene films. *Polymer Engineering & Science* **2016,** *56* (8), 889-894.

111.   Liu, F.; Gu, Y.; Jung, J. W.; Jo, W. H.; Russell, T. P., On the morphology of polymer-based photovoltaics. *J Polym Sci Pol Phys* **2012,** *50* (15), 1018-1044.

112.   Hexemer, A.; Bras, W.; Glossinger, J.; Schaible, E.; Gann, E.; Kirian, R.; MacDowell, A.; Church, M.; Rude, B.; Padmore, H., A SAXS/WAXS/GISAXS Beamline with Multilayer Monochromator. *Journal of Physics: Conference Series* **2010,** *247*, 012007.

113.   Kline, S., Reduction and analysis of SANS and USANS data using IGOR Pro. *Journal of Applied Crystallography* **2006,** *39* (6), 895-900.

114. Gebel, G.; Loppinet, B., Colloidal structure of ionomer solutions in polar solvents. *J Mol Struct* **1996,** *383* (1-3), 43-49.

115. Rubatat, L.; Gebel, G.; Diat, O., Fibrillar Structure of Nafion: Matching Fourier and Real Space Studies of Corresponding Films and Solutions. *Macromolecules* **2004,** *37* (20), 7772-7783.

116. Gebel, G., Structural evolution of water swollen perfluorosulfonated ionomers from dry membrane to solution. *Polymer* **2000,** *41* (15), 5829-5838.

117. Loppinet, B.; Gebel, G.; Williams, C. E., Small-Angle Scattering Study of Perfluorosulfonated Ionomer Solutions. *The Journal of Physical Chemistry B* **1997,** *101* (10), 1884-1892.

118. Berlinger, S. A.; McCloskey, B. D.; Weber, A. Z., Inherent Acidity of Perfluorosulfonic Acid Ionomer Dispersions and Implications for Ink Aggregation. *The Journal of Physical Chemistry B* **2018,** *122* (31), 7790-7796.

119. Teubner, M.; Strey, R., Origin of the Scattering Peak in Microemulsions. *J Chem Phys* **1987,** *87* (5), 3195-3200.

120. Chen, S. H.; Chang, S. L.; Strey, R. In *On the interpretation of scattering peaks from bicontinuous microemulsions*, Darmstadt, Steinkopff: Darmstadt, 1990; pp 30-35.

121. DeCaluwe, S. C.; Kienzle, P. A.; Bhargava, P.; Baker, A. M.; Dura, J. A., Phase segregation of sulfonate groups in Nafion interface lamellae, quantified via neutron reflectometry fitting techniques for multi-layered structures. *Soft Matter* **2014,** *10* (31), 5763-76.

122. Modestino, M. A.; Kusoglu, A.; Hexemer, A.; Weber, A. Z.; Segalman, R. A., Controlling Nafion Structure and Properties via Wetting Interactions. *Macromolecules* **2012,** *45* (11), 4681-4688.

123. Kusoglu, A.; Dursch, T. J.; Weber, A. Z., Nanostructure/Swelling Relationships of Bulk and Thin-Film PFSA Ionomers. *Adv Funct Mater* **2016,** *26* (27), 4961-4975.

124. Kushner, D. I.; Kusoglu, A.; Podraza, N. J.; Hickner, M. A., Substrate-Dependent Molecular and Nanostructural Orientation of Nafion Thin Films. *Adv Funct Mater* **2019,** *0* (0), 1902699.

125. Nagao, Y., Proton-Conductivity Enhancement in Polymer Thin Films. *Langmuir* **2017,** *33* (44), 12547-12558.

126. Dishari, S. K.; Hickner, M. A., Confinement and Proton Transfer in NAFION Thin Films. *Macromolecules* **2013,** *46* (2), 413-421.

127. Ogata, Y.; Abe, T.; Yonemori, S.; Yamada, N. L.; Kawaguchi, D.; Tanaka, K., Impact of the Solid Interface on Proton Conductivity in Nafion Thin Films. *Langmuir* **2018,** *34* (50), 15483-15489.

128. Tesfaye, M.; Kushner, D. I.; Kusoglu, A., Interplay between Swelling Kinetics and Nanostructure in Perfluorosulfonic Acid Thin-Films: Role of Hygrothermal Aging. *ACS Applied Polymer Materials* **2019,** *1* (4), 631-635.

129. Liu, J.; Yager, K. G., Unwarping GISAXS data. *IUCrJ* **2018,** *5* (6), 737-752.

130. Teubner, M.; Strey, R., Origin of the scattering peak in microemulsions. *The Journal of Chemical Physics* **1987,** *87* (5), 3195-3200.

131. Kusoglu, A.; Savagatrup, S.; Clark, K. T.; Weber, A. Z., Role of Mechanical Factors in Controlling the Structure–Function Relationship of PFSA Ionomers. *Macromolecules* **2012,** *45* (18), 7467-7476.

132. Luan, Y.; Zhang, Y.; Zhang, H.; Li, L.; Li, H.; Liu, Y., Annealing effect of perfluorosulfonated ionomer membranes on proton conductivity and methanol permeability. *Journal of Applied Polymer Science* **2008,** *107* (1), 396-402.

133. Tang, Y.; Karlsson, A. M.; Santare, M. H.; Gilbert, M.; Cleghorn, S.; Johnson, W. B., An experimental investigation of humidity and temperature effects on the mechanical properties of perfluorosulfonic acid membrane. *Materials Science and Engineering: A* **2006,** *425* (1), 297-304.

134. Wang, J.; Yang, M.; Dou, P.; Wang, X.; Zhang, H., Influences of Annealing on the Perfluorosulfonate Ion-Exchanged Membranes Prepared by Melt Extrusion. *Industrial & Engineering Chemistry Research* **2014,** *53* (36), 14175-14182.

135. Hensley, J. E.; Way, J. D.; Dec, S. F.; Abney, K. D., The effects of thermal annealing on commercial Nafion® membranes. *Journal of Membrane Science* **2007,** *298* (1), 190-201.

136. Alizadeh, A.; Richardson, L.; Xu, J.; McCartney, S.; Marand, H.; Cheung, Y. W.; Chum, S., Influence of Structural and Topological Constraints on the Crystallization and Melting Behavior of Polymers. 1. Ethylene/1-Octene Copolymers. *Macromolecules* **1999,** *32* (19), 6221-6235.

137. Loo, Y.-L.; Wakabayashi, K.; Huang, Y. E.; Register, R. A.; Hsiao, B. S., Thin crystal melting produces the low-temperature endotherm in ethylene/methacrylic acid ionomers. *Polymer* **2005,** *46* (14), 5118-5124.

138. Wang, Y.; Rafailovich, M.; Sokolov, J.; Gersappe, D.; Araki, T.; Zou, Y.; Kilcoyne, A. D. L.; Ade, H.; Marom, G.; Lustiger, A., Substrate Effect on the Melting Temperature of Thin Polyethylene Films. *Physical Review Letters* **2006,** *96* (2), 028303.

139. Sadler, D. M.; Gilmer, G. H., Selection of lamellar thickness in polymer crystal growth: A rate-theory model. *Physical Review B* **1988,** *38* (8), 5684-5693.

140. Divoux, G. M.; Finlay, K. A.; Park, J. K.; Song, J.-M.; Yan, B.; Zhang, M.; Dillard, D. A.; Moore, R. B., Morphological Factors Affecting the Behavior of Water in Proton Exchange Membrane Materials. *ECS Transactions* **2011,** *41* (1), 87-100.

141. Rusch, K. C., Time-temperature superposition and relaxational behavior in polymeric glasses. *Journal of Macromolecular Science, Part B* **1968,** *2* (2), 179-204.

142. Nonoyama, N.; Okazaki, S.; Weber, A. Z.; Ikogi, Y.; Yoshida, T., Analysis of Oxygen-Transport Diffusion Resistance in Proton-Exchange-Membrane Fuel Cells. *Journal of The Electrochemical Society* **2011,** *158* (4), B416-B423.

143. Kidena, K.; Ohkubo, T.; Takimoto, N.; Ohira, A., PFG-NMR approach to determining the water transport mechanism in polymer electrolyte membranes conditioned at different temperatures. *European Polymer Journal* **2010,** *46* (3), 450-455.

144. Maldonado, L.; Perrin, J.-C.; Dillet, J.; Lottin, O., Characterization of polymer electrolyte Nafion membranes: Influence of temperature, heat treatment and drying protocol on sorption and transport properties. *Journal of Membrane Science* **2012,** *389*, 43-56.

145. Shi, S.; Weber, A. Z.; Kusoglu, A., Structure/property relationship of Nafion XL composite membranes. *Journal of Membrane Science* **2016,** *516*, 123-134.

146. Li, J.; Park, J. K.; Moore, R. B.; Madsen, L. A., Linear coupling of alignment with transport in a polymer electrolyte membrane. *Nat Mater* **2011,** *10* (7), 507-511.

147. Allahyarov, E.; Taylor, P. L., Simulation Study of the Correlation between Structure and Conductivity in Stretched Nafion. *The Journal of Physical Chemistry B* **2009,** *113* (3), 610-617.

148.   Arges, C. G.; Kambe, Y.; Dolejsi, M.; Wu, G.-P.; Segal-Pertz, T.; Ren, J.; Cao, C.; Craig, G. S. W.; Nealey, P. F., Interconnected ionic domains enhance conductivity in microphase separated block copolymer electrolytes. *Journal of Materials Chemistry A* **2017,** *5* (11), 5619-5629.

149.   Diederichsen, K. M.; Brow, R. R.; Stoykovich, M. P., Percolating Transport and the Conductive Scaling Relationship in Lamellar Block Copolymers under Confinement. *ACS Nano* **2015,** *9* (3), 2465-2476.